

Crystalline Disposal R&D at LBNL: FY18 Progress Report

Spent Fuel and Waste Disposition

*Prepared for
US Department of Energy
Spent Fuel and Waste Science and Technology*
Liang Zheng¹, Hang Deng¹,
Seiji Nakagawa¹, Kunhwi Kim¹,
Timothy Kneafsey¹, Patrick Dobson¹,
Sharon Borglin¹, Chris Doughty¹, Marco Voltolini¹,
Chin-Fu Tsang^{1,2}, Benoît Dessirier²,
Quinn Wenning³, Chris Juhlin²
¹LBNL, ²Uppsala University, ³ETH

August 24, 2018

LBNL-2001177

SFWD Working Document: External Release

DISCLAIMER

This document was prepared as an account of work sponsored by the United States Government. While this document is believed to contain correct information, neither the United States Government nor any agency thereof, nor the Regents of the University of California, nor any of their employees, makes any warranty, express or implied, or assumes any legal responsibility for the accuracy, completeness, or usefulness of any information, apparatus, product, or process disclosed, or represents that its use would not infringe privately owned rights. Reference herein to any specific commercial product, process, or service by its trade name, trademark, manufacturer, or otherwise, does not necessarily constitute or imply its endorsement, recommendation, or favoring by the United States Government or any agency thereof, or the Regents of the University of California. The views and opinions of authors expressed herein do not necessarily state or reflect those of the United States Government or any agency thereof or the Regents of the University of California.

This line intentionally left blank.

Revision 5
01/15/2018**APPENDIX E****NTRD DOCUMENT COVER SHEET ¹**

Name/Title of Deliverable/Milestone/ Revision No. Crystalline Disposal R&D at LBNL / M4SF-18LB010302031

Work Package Title and Number Crystalline Disposal R&D – LBNL SF-18LB01030203

Work Package WBS Number 1.08.01.03.02

Responsible Work Package Manager Liange Zheng (signature on file)

(Name/Signature)

Date Submitted **08/24/2018**

Quality Rigor Level for Deliverable/Milestone ²	<input type="checkbox"/> QRL-1 Nuclear Data	<input type="checkbox"/> QRL-2	<input type="checkbox"/> QRL-3	<input checked="" type="checkbox"/> QRL 4 Lab-specific ₃
--	--	--------------------------------	--------------------------------	--

This deliverable was prepared in accordance with

Lawrence Berkeley National Laboratory (LBNL)*(Participant/National Laboratory Name)*

QA program which meets the requirements of

 DOE Order 414.1 NQA-1 Other**This Deliverable was subjected to:** Technical Review Peer Review**Technical Review (TR)****Peer Review (PR)****Review Documentation Provided****Review Documentation Provided** Signed TR Report or, Signed PR Report or, Signed TR Concurrence Sheet or, Signed PR Concurrence Sheet or, Signature of TR Reviewer(s) below Signature of PR Reviewer(s) below**Name and Signature of Reviewers****Name and Signature of Reviewers**Hao Xu (signature on file)Boris Faybishenko (signature on file)

NOTE 1: Appendix E should be filled out and submitted with each deliverable. Or, if the PICS:NE system permits, completely enter all applicable information in the PICS:NE Deliverable Form. The requirement is to ensure that all applicable information is entered either in the PICS:NE system or by using the FCT Document Cover Sheet.

- In some cases there may be a milestone where an item is being fabricated, maintenance is being performed on a facility, or a document is being issued through a formal document control process where it specifically calls out a formal review of the document. In these cases, documentation (e.g., inspection report, maintenance request, work planning package documentation or the documented review of the issued document through the document control process) of the completion of the activity, along with the Document Cover Sheet, is sufficient to demonstrate achieving the milestone.

NOTE 2: If QRL 1, 2, or 3 is not assigned, then the QRL 4 box must be checked, and the work is understood to be performed using laboratory specific QA requirements. This includes any deliverable developed in conformance with the respective National Laboratory / Participant, DOE or NNSA-approved QA Program.

NOTE 3: If the lab has an NQA-1 program and the work to be conducted requires an NQA-1 program, then the QRL-1 box must be checked in the work Package and on the Appendix E cover sheet and the work must be performed in accordance with the Lab's NQA-1 program. The QRL-4 box should not be checked.

This page intentionally left blank.

CONTENTS

ACRONYMS	xiii
1. INTRODUCTION	1
2. Simulating pore-scale gas bubble migration	3
2.1 Introduction	3
2.2 Modeling Approach	4
2.3 Model Verification	5
2.3.1 Young-Laplacian Equation for a Spherical Bubble	5
2.3.2 Two-Phase Flow in a Rough Channel	6
2.3.3 Discussions	8
2.4 Pore scale characterization for simulations in actual pore structures	8
2.5 Future Work	10
3. LABORATORY AND MODELING STUDY ON EDZ	11
3.1 Introduction	11
3.2 EDZ Experiments Using Shaped Rectangular Sample	12
3.2.1 Experimental Setup	12
3.2.1.1 Test Samples	12
3.2.1.2 Test System	15
3.2.2 Experimental Results	15
3.2.2.1 Loading Test Results	15
3.2.2.2 Geophysical (Seismic) Measurement Results	19
3.2.2.3 Permeability Changes Due To EDZ Development	24
3.3 Rigid Body Spring Network (RBSN) Modeling of EDZ Development	27
3.3.1 Model Setup	27
3.3.2 Implementation of Arbitrary Poisson's Ratio	29
3.3.2.1 RBSN Model Formulation	29
3.3.2.2 Fictitious Stress Approach	31
3.4 Conclusions and Future Plans	32
4. HYDRAULIC PROPERTIES OF FRACTURED CRYSTALLINE ROCK CORES	35
4.1 Introduction	35
4.2 Methodology	35
4.2.1 Description of Fractures	35
4.2.2 Aperture Measurements	37
4.2.3 Experimental Apparatus	38
4.2.4 Experimental Procedure	42
4.2.5 Transmissivity Calculations	42
4.3 Laboratory results	43
4.3.1 Anisotropy Analysis of FY17 Experiments	43
4.3.2 FY18 Experiments	47
4.4 Conclusions	48

4.4.1 Future Work	48
5. FRACTURES AND FLUID FLOW IN CRYSTALLINE ROCKS – EXAMPLE FROM THE COSC-1 BOREHOLE, SWEDEN	51
5.1. Introduction	51
5.2 Fracture Characteristics of the COSC-1 Borehole	53
5.2.1 Introduction to the COSC-1 Project.....	53
5.2.2 Fracture Systematics of the COSC-1 borehole	54
5.2.3 Fractures Associated With Permeable Features Identified from FFEC logging	54
5.2.4 Analysis of Fracture Mineralization of Selected Core Samples Using X-Ray Diffraction (XRD).....	59
5.3 Correlation of FFEC Flow Zones with Fracture Features and Future Work.....	61
6. Summary of FY2018 Progress and Future Work	63
7 ACKNOWLEDGMENTS	65
8 REFERENCES	67

LIST OF FIGURES

Figure 2-1 (a) A cross-section of the computational domain with the gas bubble in the center. (b) Pressure difference between the gas bubble and its surrounding water in relation to the radius of the gas bubble. The dashed line is the results from the Young-Laplace equation, and the blue circles are simulation results from interFoam.	6
Figure 2-2. Schematic of the computational domain, initial volumes of air and water fractions, and boundary conditions.....	6
Figure 2-3. (a) Interfacial velocity from the results of numerical simulations, and (b)-(e) snapshots of the water-air interface predicted by the simulation. The blue band in (a) illustrates the variation of the gas phase volume observed in the experiment.	8
Figure 2-4. (a) 3D volume, (b) connected pore components, and (c) pore throats in the clay volume. (d) Distributions of pore and pore throat size. (e) Ratio a/b and (f) ratio b/c of equivalent ellipsoid. (g) Illustration of the equivalent ellipsoid.	9
Figure 2-5. (a) 3D volume, (b) connected pore components, and (c) pore throats in the carbonate volume. (d) Distributions of pore and pore throat size. (e) Ratio a/b and (f) ratio b/c of the equivalent ellipsoid.	10
Figure 3-1. EDZ at different scales. (a) Large-scale EDZ in a 3.5-m diameter mine tunnel (Martin, 1997); and (b) cm-scale borehole breakout (in Berea sandstone) observed in the laboratory.	11
Figure 3-2. Size effect of breakout observed in the laboratory (Martin, 1997).	11
Figure 3-3. Photograph of shaped Westerly granite slabs used for the experiment.	12
Figure 3-4. 2-D finite element stress analysis using LISA. Only one quarter of the actual sample is modeled due to the symmetry. The top boundary is not constrained, and the uniform axial stress is applied on it.	13
Figure 3-5. 2D finite element stress analysis of the effect of steel footing attached to the end of a shaped slab sample. The stress resulting from unit compressive stress at the top (i.e., the stress concentration) is shown.	14
Figure 3-6. Comparisons between stresses along the minimum horizontal stress line (along the bottom of the model shown in Figure 3-5) of the shaped slab sample and a borehole within an infinite medium with a far-field compressional maximum stresses ratio of ($\sigma_{xx}^{\infty}, \sigma_{zz}^{\infty}$)=(100 MPa, 200 MPa), which is represented by solid lines in plots. Note that, along the center line, $\sigma_{xx} = \sigma_{rr}$ and $\sigma_{zz} = \sigma_{\theta\theta}$. The vertical scale is adjusted for the shaped slab sample. Actual max. stress concentration factor for the slab is ~1.20 times (instead of 2.5 ×) the applied axial stress. The ‘Teflon’ curves represent the case when the sample top has no lateral constraints.	14
Figure 3-7. Bi-axial loading test on a shaped slab of Westerly granite. Acoustic emissions were monitored concurrently with the loading tests. 8 sensors are embedded within grooves in a pair of transparent acrylic loading platens attached to the X surfaces of the slab, mediated by a PTFE (Teflon) film. During the test, large axial (Z) stress was applied while only small confining stress in the X direction was applied and held constant.....	15
Figure 3-8. Loading test on shaped slab Sample Z-1 without steel footings. The failure of the sample was caused by axial splitting, with the ultimate strength of the sample of 161 MPa.....	16

Figure 3-9. Loading test on shaped slab Sample Z-2 with steel footings. The sample was temporarily unloaded from ~170 MPa to ~70 MPa after a large number of acoustic emissions were detected at T~3,000 s. The maximum applied stress was 208 MPa, and the sample was not brought to the ultimate failure. The photograph to the right shows a close-up view of surface spalling (breakout) caused by the axial loading. 17

Figure 3-10. Loading test on shaped slab Sample Z-3 with steel footings: Left—the photograph of the sample before the test; middle—graphs of the stress vs time during the test; and right—the photograph of the sample loaded by steps up to ~208 MPa, when the strong, creep deformation occurred, showing a visible, continuous fracture development on the slab surface. Without further increases in load, the ultimate failure was reached at T~5,000 s. The photographs indicate axial-splitting and buckling failure, typically seen on a tunnel and borehole wall suffering EDZ development, and a diagonal shear band which led to the ultimate loss of the load-bearing capacity of the sample. 17

Figure 3-11. Side view of axial-splitting and buckling failure in Sample Z-3..... 18

Figure 3-12. Snapshots of the EDZ (breakout) development during the slow creep deformation started at T=4,300 s. Note that the time stamps are the elapsed time after the recording was started at T=4,750s. 18

Figure 3-13 Acoustic emission event rate (number of detected events per second) history through the experiment on Sample Z-1. The corresponding axial stresses are also shown. The sudden decrease of the AE counts after reaching 200 counts per second, and the dots in magenta, indicates that the sensors and the measurement system were overwhelmed by an extremely large number of AE events which saturated the measurement capacity. 19

Figure 3-14 Acoustic emission event rate (number of detected events per second) history through the experiment on Sample Z-2. The corresponding axial stresses are also shown. 20

Figure 3-15. Acoustic emission event rate (number of detected events per second) history throughout the experiment on Sample Z-3. The corresponding axial stresses are also shown. Note that, compared to Figure 3-10, the view in these plots are from the back side of the sample shown in the photograph in Figure 3-10. 21

Figure 3-15. (Continued) Acoustic emission event rate (number of detected events per second) history throughout the experiment on Sample Z-3. The corresponding axial stresses are also shown. The data acquisition system saturated after ~4,000 s due to extremely strong AE activity. In the location plot, higher activity did seem to focus near the edges of a diagonal shear zone. 22

Figure 3-16. Seismic-velocity scan lines on Sample Z-2..... 22

Figure 3-17. P and S-wave velocity distributions within an intact (Sample Z-4) and moderately damaged (Sample Z-2) slabs. 23

Figure 3-18. S-wave velocity anisotropy of Sample Z-2. Thomsen’s γ parameter is shown. 24

Figure 3-19. Locations of small subcores and thin section samples in Sample Z-2. 25

Figure 3-20. Mini triaxial test core holder used for permeability tests on the subcores. 25

Figure 3-21. Water-injection flow permeability tests on mini cores. The overall changes in the injection rate correspond well to the expected degree of fracturing of the core samples for their locations in the moderately damaged slab Sample Z-2. Note that Sample R1 has not been tested yet. 25

Figure 3-22. Petrographic thin section samples made for the Sections M1, M2, and M3 shown in Figure 3-19. The width of the samples is 50.8 mm, and the height 25.4 mm. Blue boxes (FOV1 and FOV2) in the figure indicate the field of view of the magnified microscope images shown in Figure 3-23.....	26
Figure 3-23. Thin-section images of FOV1 and FOV2 shown in Figure 3-22. Microcracks in the samples are mostly concentrated near the spalling observed on the surface of the sample, and much less cracks are found inside the slab samples.	27
Figure 3-24. Domain partitioning process: a) nodal points; b) Delaunay, and c) Voronoi cells.	28
Figure 3-25. Preparation of shaped slab samples: a) for laboratory experiments; and b) for the numerical simulations.....	29
Figure 3-26. Typical RBSN lattice element ij: a) neighboring nodes i and j in a Voronoi diagram; b) isolated from the network; and c) a zero-size spring set located at centroid C of Voronoi cell boundary area A_{ij} (rotational springs have been omitted for clarity).....	30
Figure 3-27. Stress tensor at a Voronoi cell node: (a) components of spring force local coordinates; (b) a set of nodal forces satisfying the equilibrium; and (c) complete stress tensor at Voronoi cell node (Adapted from Yip et al., 2005).	30
Figure 4-1. Photographs of natural and artificial cores used in this study.	36
Figure 4-2(a.) Aperture maps from CT measurements for cores 211-2 (left) and 401-1 (right). Calibration scale in μm . Scans were taken on the cores with no confining pressure applied before the transmissivity measurements were made.	37
Figure 4-2(b.) Cross sections of Cores 211-2 (left) and 401-1 (right).	37
Figure 4-3. Sample on CT table ready for scanning.	38
Figure 4-5. System schematic: The lower syringe pump controls confining pressure, and the upper syringe pump flows water through the core. Two 5-way ball valves (one shown) control flow to the inlet tubes (1-4) and outlet tubes (5-8).	40
Figure 4-6. Apparatus assembly: (a) Both pieces of the fractured core are placed in between the water inlets and outlets, (b) feed-through ports on the pressure vessel cap, (c) end of core showing the Silicone rubber sleeve, and (d) view with outer sleeve in place.....	41
Figure 4-7. Schematic diagram of fractured core geometry used for calculations.....	43
Figure 4-8. Transmissivities of various flow paths for Core 211-2 – all experiments conducted in FY17. Transmissivity for each path is shown with a different line thickness, to enable overlapping values to be seen.	44
Figure 4-9. Transmissivities of various flow paths for Core 211-2 – individual cycles of FY17 data.	45
Figure 4-10. Transmissivities of various flow paths for Core 401-1 experiments conducted in FY17, and the transmissivity inferred from FFEC logging in the field. The transmissivity of Path 4 to 8 is zero.	46
Figure 4-11. Schematic of anisotropic flow from analysis of FY17 data.	47
Figure 5-1. Frequency histogram of 'Fracture Zone Index (FZI)' values for 1 m long borehole intervals at Stripa. Intervals with an FZI value greater than 2 were considered part of a fracture zone. FZI was determined through a linear combination of data from borehole measurements of electric resistivity, sonic velocity, hydraulic conductivity, fracture frequency and occurrence of single-hole radar reflectors (Olsson and Gale, 1995).....	51

Figure 5-2. Conceptual geological-hydrogeological models, showing fracture domains, connected open fractures, and fracture end-members at Forsmark (Lundqvist and Hammarström, 2016).....	52
Figure 5-3. Geology and location of the COSC-1 deep borehole (Gee et al., 2013; Lorenz et al., 2015).....	53
Figure 5-4. Left - Lower hemisphere Schmidt equal area projection of the poles to the foliation planes (black circles) depicting the primary shallow (0–500 m) and deep (500–2500 m) foliation trends. Center - Lower hemisphere Schmidt equal area projection of the poles (black circles) to the natural fracture planes. Right - Rose diagram of the orientation of the natural fractures. (Wenning et al., 2017).	54
Figure 5-5. Correlation at 1237-1247 m in COSC-1 borehole between natural gamma and rock density/magnetic susceptibility logs used for depth matching (left two columns), the peaks obtained using the FFEC method identifying approximate location of flowing fractures (central column), and the unrolled core image, the sulfur content (wt. %), and the amplitude of the televiewer image (right two columns). Correlation conducted by B. Dessirier, Uppsala University.	56
Figure 5-6. X-ray powder diffraction profile for fracture mineralization for samples 144-2 (left) and 188-4 (right), where the blue dots are the measured data and the black line is the Rietveld model. The peak positions for each phase are marked at the bottom.	60
Figure 5-7. Piper diagram of borehole waters from COSC-1 well (Dobson et al., 2016).	60

LIST OF TABLES

Table 2-1. Density and kinematic viscosity of water and air, surface tension and contact angle used in the numerical simulations.....	5
Table 2-2. Boundary conditions used for the rough fracture simulations.....	7
Table 2-3. Solver information.....	7
Table 4-1. Transmissivity of Core 211-2. All values in m^2/s	47
Table 4-2. Transmissivity of Core 211-2 altered by applying cementing compound to gaps at core edge near port 8. All values in m^2/s	48
Table 4-3. Transmissivity of Core 401-1. All values in m^2/s	48
Table 5-1. FFEC peak locations, corresponding core samples, and fractures and foliations in the COSC-1 borehole.	55
Table 5-2. Photos of COSC-1 core samples.	57
Table 5-3. Observations of fractures in COSC-1 core samples.	59

This page intentionally left blank.

ACRONYMS

AE	Acoustic Emission
CFD	Computational Fluid Dynamics
COSC	Collisional Orogeny in the Scandinavian Caledonides
DIC	diagonal incomplete-Cholesky, symmetric
EDZ	excavation damage zone
FFEC	flowing fluid electrical conductivity
FIB-SEM	Focus Ion Beam Scanning Electron Microscopy
HMC	hydrological-mechanical-chemical
LBNL	Lawrence Berkeley National Laboratory
NPT	national pipe thread
OpenFOAM	Open Field Operation and Manipulation
PCG	preconditioned conjugate gradient
R&D	Research & Development
RBSM	Rigid-Body-Spring Model
RBSN	The Rigid-Body-Spring Network
URL	Underground Research Laboratory
VOF	volume of fluid
XRD	X-ray diffraction
XRPD	X-ray powder diffraction

1. INTRODUCTION

Lawrence Berkeley National Laboratory's (LBNL) research contributions to the nuclear waste disposal project crystalline rock in FY18 consist of a broad scope of activities, building upon relevant work conducted in previous years relating to deep borehole disposal in crystalline rock. These research activities provide important insights to understanding and predicting flow and transport processes that could occur in low permeability crystalline rocks, where fractures might serve as the main conduits for fluid flow and radionuclide transport.

Section 2 provides an introduction to a new R&D activity aimed at simulation of pore-scale gas bubble migration. Gas production could occur from metal corrosion, radiolysis of trapped water, or from microbial activities. The generation of gas bubbles could impact the migration of radionuclides in the subsurface or cause rock fracturing and the creation of new flow paths. The preliminary modeling work investigates the migration of gas bubbles within different simulated pore structures to evaluate the behavior of bubbles and their potential impact of radionuclide migration.

Section 3 presents the results of laboratory and modeling studies to evaluate the nature of the excavation damage zone (EDZ), which would be an important feature of a mined crystalline repository. One of the challenges of conducting laboratory experiments is to ascertain that the results can be scaled to field scale geometries. A series of laboratory experiments were conducted in FY18 on granite slabs with a special geometry to replicate the stresses and rock deformation responses that would be present in larger circular excavations – the formation of microcracks was monitored using seismic techniques. Permeability measurements were conducted on the damaged samples to evaluate the impact that the damage zone had on fluid flow properties. Preliminary work was also conducted using rigid body spring network modeling to begin to numerically simulate these experiments.

Sections 4 and 5 of the report describe our work with members of the science team of the "Collisional Orogeny in the Scandinavian Caledonides" (COSC) project, which drilled and characterized a 2.5 km borehole COSC-1 in central Sweden, to obtain key scientific insights on the flow characteristics of crystalline basement rocks. In particular, **Section 4** examined the hydraulic properties of crystalline rock cores from the COSC-1 well determined using a unique laboratory-scale apparatus, developed at LBNL. This apparatus was used to measure multi-directional transmissivity to assess fracture anisotropy under confining stress conditions. These fractured core samples were spatially correlated with fluid flow zones in the COSC-1 well, which were identified by flowing fluid electrical conductivity (FFEC) logs. **Section 5** examines the relation between conductive zones in the COSC-1 borehole determined using flowing fluid electrical conductivity logging with fractures that were mapped from acoustic borehole image logs and core sample descriptions. Two main types of fractures have been observed: a steeply dipping fracture set that is associated with the current stress regime, and more shallowly dipping fractures that parallel the rock foliation. It appears that most of the flow zones are associated with foliation-parallel fractures.

This page intentionally left blank.

2. SIMULATING PORE-SCALE GAS BUBBLE MIGRATION

2.1 Introduction

Gas production in geologic nuclear waste disposal systems has been identified as one of the processes that can affect the long-term performance and safety of these systems (Birkholzer et al., 2012; Claret et al., 2018; Tsang et al., 2015). Three main mechanisms are responsible for gas production in nuclear waste disposal systems. Corrosion of metals in canisters, which is considered as the primary gas source, typically involves iron oxidation and hydrogen gas (H₂) production (Xu et al., 2008). Radiolysis of trapped water due to radiation emitted by the spent fuel can also produce hydrogen gas and oxygen gas (O₂) (Christensen and Sunder, 2000). In addition, activities of subsurface microorganisms, which have been reported for crystalline rock at depth (Pedersen, 1999), can lead to the production of an ensemble of gases including carbon dioxide, hydrogen, methane, and hydrogen sulfide (Pedersen, 1996; 1999). Gas bubbles may form and sometimes continuous gas flow may be created as a result of local accumulation of the produced gases.

Understanding the migration of gas bubbles, and the gas-liquid interface, is generally important for the evaluation and assessment of waste disposal sites. First, radionuclides and microorganisms may be preferentially sorbed on the gas-water interface, and the gas velocity is expected to control the migration of these radionuclides (Wan and Wilson, 1994). While continuous flow of gas may enhance transport of radionuclides, gas bubbles trapped in the rock formation can lead to the immobilization of radionuclides. Second, gas migration into regions where there is substantial pressure build-up can induce damage or cause fracturing, and thus create new flow paths (Kim et al., 2011).

The migration of gas bubbles in porous media is controlled by the interplay between the surface tension, inertial, viscous and buoyancy forces (Cihan and Corapcioglu, 2008). Gas bubble migration is affected by not only the liquid and gas properties (e.g., density and viscosity), but also by the pore structure, which control the curvature of the gas-liquid interface, and thus the surface tension force. For example, as gas bubbles enter or exit a pore-throat, the deformation of the bubbles can cause large changes in the surface tension force. The well-known Haines jump is one example that highlights the impact of the pore-structure on two-phase flow (Berg et al., 2013; Armstrong et al., 2015). When the interface exits the pore-throat, capillary pressure drops and the interfacial velocity increases as a result of elastic energy being converted to kinetic energy. The interfacial velocity then decreases as the kinetic energy dissipates. Bubble breakups or snap-offs in pore throats and coalescence have also been observed (Berg et al., 2013, Roman et al., 2017).

Enhancing our understanding of the gas bubble migration at a pore scale is important because we need to study the effects of chemical reactions of radionuclides or microbial activities and fracturing events that occur at a micro-scale. It is also important because these pore-scale processes can propagate through larger scales and affect macroscopic flow and pressure behaviors (Berg et al., 2013; Armstrong et al., 2015). For example, in the experiment by Berg et al. (2013), the pressure drop measured across a 10 mm core showed variations on the temporal scale of dozens of seconds. The pressure variations were attributed to pore-scale Haines jump that was confirmed by real-time 3D imaging (Berg et al., 2013).

The overall objectives of this study are (a) to investigate the impact of pore structures and macroscopic pressure gradient on gas bubble and interfacial migration velocity and local transient pressure variations, and (b) to evaluate the dynamics of gas bubble formation and consumption coupled with reactions, and (c) to evaluate possible mechanical responses, and radionuclides migration at a larger field scale. This chapter reports the results of preliminary investigations, and focuses on the morphological analysis and model verification, which are followed by an outline of future research.

2.2 Modeling Approach

To investigate the impact of pore structures on gas bubble migration, we selected the traditional mesh-based Computational Fluid Dynamics (CFD) approach, which numerically solves the Navier-Stokes equation. Compared to the Lattice Boltzmann method, CFD has the advantages of being computationally efficient and able to handle systems with large density and viscosity contrasts (e.g. water-gas systems). It also avoids the use of idealized geometries and effective properties in pores and throats as in pore network modeling (Meakin and Tartakovsky, 2009; Blunt et al., 2013; Bultreys et al., 2016).

An open source software package, OpenFOAM (Open Field Operation and Manipulation) (Jasak, 2009), was used for the simulations. It is a C++ toolbox that includes a collection of numerical solvers and pre/post-processing utilities, which can be used to solve of a multitude of physical problems in areas including fluid dynamics and continuum mechanics.

InterFoam, a transient solver for two incompressible isothermal immiscible fluids, was selected for the simulations. It is widely used for two-phase flow simulations and has been reported to be applicable for a wide range of conditions (Deshpande et al., 2012; Adrian et al., 2016). InterFoam implements a modified version of the volume of fluid (VOF) method, inheriting features such as mass conservation from the VOF method and reducing numerical smearing of the interface.

In general, the VOF approach treats the two phases as an effective single phase by solving the continuity and momentum equations given by

$$\nabla \cdot \mathbf{U} = 0 \quad (2.1)$$

$$\frac{\partial(\rho\mathbf{U})}{\partial t} + \nabla \cdot (\rho\mathbf{U}\mathbf{U}) = -\nabla p + \mu[\nabla\mathbf{U} + (\nabla\mathbf{U})^T] + \mathbf{F} \quad (2.2)$$

where \mathbf{F} is the body force, e.g., surface tension force, and \mathbf{U} , ρ and μ are weighted averages between the two phases, determined based on the volume fraction of the two phases:

$$\mathbf{U} = \alpha\mathbf{U}_w + (1 - \alpha)\mathbf{U}_{nw} \quad (2.3a)$$

$$\rho = \alpha\rho_w + (1 - \alpha)\rho_{nw} \quad (2.3b)$$

$$\mu = \alpha\mu_w + (1 - \alpha)\mu_{nw} \quad (2.3c)$$

where α is the volume fraction of the wetting phase, and the subscripts w and nw denote the wetting and non-wetting phases, respectively.

An additional equation is introduced for the transport of α

$$\frac{\partial\alpha}{\partial t} + \nabla \cdot (\alpha\mathbf{U}) = 0 \quad (2.4)$$

The modified VOF method requires first writing the transport equations for both phases separately, as it would be the case for the Euler-Euler approach, and combines them into the following equation given by

$$\frac{\partial\alpha}{\partial t} + \nabla \cdot (\alpha\mathbf{U}) + \nabla \cdot (\alpha(1 - \alpha)\mathbf{U}_r) = 0 \quad (2.5)$$

where \mathbf{U}_r is the compression velocity defined as the velocity difference between the wetting and non-wetting phases, and the additional term in Equation (2.5) ensures a sharp interface.

2.3 Model Verification

Two test cases were simulated to validate the modeling approach under conditions that are most relevant to nuclear waste disposal systems, which are described below.

2.3.1 Young-Laplacian Equation for a Spherical Bubble

In this case, a single static spherical gas bubble was placed in a cube of water as illustrated in Figure 2-1(a). 3D simulations were performed for a range of gas bubble radii (R) between 5 and 500 μm . The dimension of the cube is ten times of the radius of gas bubble, i.e. 50 to 5,000 μm , which is assumed to minimize the wall effect. The mesh for each simulation was generated such that the bubble diameter was represented by 20 grid cells. The simulations were performed to evaluate the pressure field for the gas bubble and the surrounding water with no flow boundary conditions. The simulated pressure difference (dP) between the interior of the gas bubble and the surrounding water was compared with the theoretical prediction using the Young-Laplace law (Equation (2.6))

$$dP = 2\sigma/R \quad (2.6)$$

where R is the bubble radius, and σ is the surface tension.

Properties of the water and air phases and the surface tension used in the simulations are summarized in Table 2-1.

Table 2-1. Density and kinematic viscosity of water and air, surface tension and contact angle used in the numerical simulations.

Property	Value
Water density	1000 kg/m ³
Water kinematic viscosity	1.0e-6 m/s ²
Air density	1.2 kg/m ³
Air kinematic viscosity	1.5e-5 m/s ²
Surface tension	0.072 N/m
Contact angle (for water and gas on PDMS)	45°

Figure 2-1(b) plots the pressure difference against the radius of the gas bubble. The simulation results are in good agreement with the analytical solution of the Young-Laplace equation. However, over time, the bubble center deviates from the center of the computational domain. This unexpected bubble motion is more evident for bubbles with small radii.

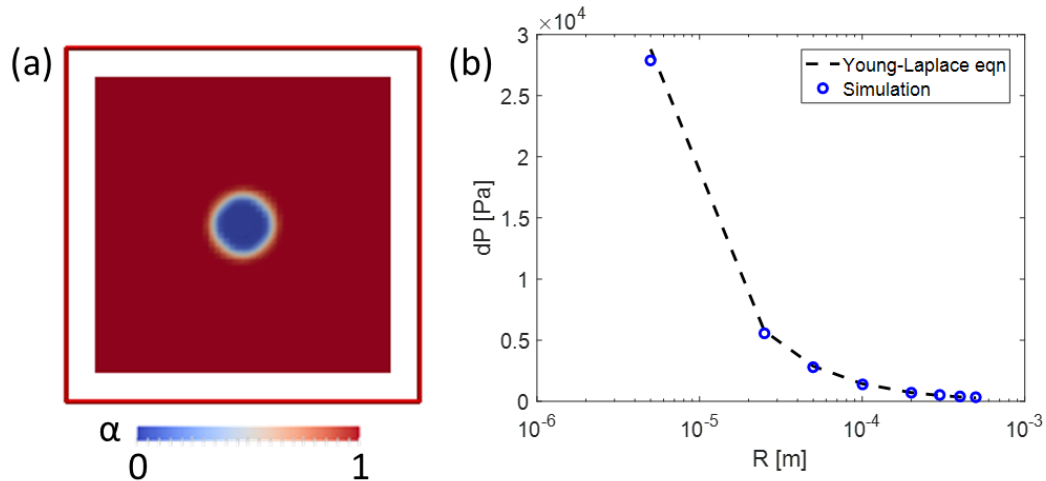


Figure 2-1 (a) A cross-section of the computational domain with the gas bubble in the center. (b) Pressure difference between the gas bubble and its surrounding water in relation to the radius of the gas bubble. The dashed line is the results from the Young-Laplace equation, and the blue circles are simulation results from interFoam.

2.3.2 Two-Phase Flow in a Rough Channel

In the second test case, the migration of a water-air interface in a rough channel was simulated and compared with previous experimental observations (Chang et al., 2017). Chang et al. (2017) described the results of microfluidic experiments performed using rough fracture sections, where water was displaced by air at a flow rate of 0.1 ml/hr, which divided by the average aperture and depth of the fracture gives an average velocity $v=208 \mu\text{m/s}$. The capillary number ($Ca = \mu_w v / \sigma$) of the experiments was on the order of $1e-7$, which is representative of the low capillary number conditions typically encountered in the subsurface. *In situ* images were taken to track the water-air interface and to quantify the migration velocity of the interface. A subsection of the rough-fracture reported in the paper was used to reconstruct the geometry (Figure 2-2). The average width of the channel is 2.2 mm and the length of the subsection is 6 mm. The 2D mesh used for the numerical simulations was generated using the OpenFOAM utility *snappyHexMesh*, with an average grid cell size of $24 \mu\text{m}$.

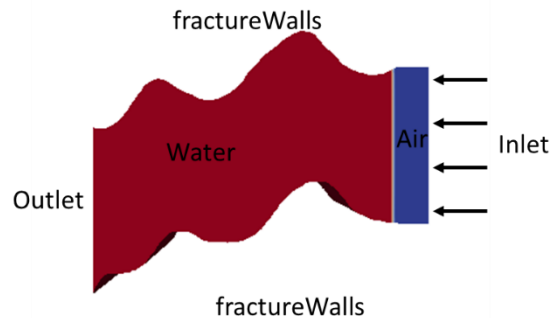


Figure 2-2. Schematic of the computational domain, initial volumes of air and water fractions, and boundary conditions.

Properties of the water and air phases and the surface tension used in the simulations were the same as in the first test (see Table 2-1). The contact angle was 45° as reported in the experimental study. Boundary

conditions of the rough fracture simulations and the information of the solvers used in all simulations are summarized in Tables 2 and 3, respectively. The time step was constrained by the Courant number of the average flow and the Courant number of the interface. The values of the two Courant numbers were set to 0.1. Default numerical schemes were used, except for the divergence term of velocity. It was set to *Gauss linearUpwindV cellLimited Gauss linear 1*, i.e., a linear upwind scheme was used to interpolate the face values using a cell limiter in the direction of greatest changes, to increase stability of the solution.

Table 2-2. Boundary conditions used for the rough fracture simulations

Boundary Condition	Velocity [m/s]	Pressure [Pa]	Volume fraction of water
Inlet	Uniform fixed value	Zero Gradient	Zero
Outlet	Zero Gradient	Uniform fixed value	Zero Gradient
Fracture Walls	No Slip	Fixed Flux Pressure	Constant contact angle

Table 2-3. Solver information

Boundary Condition	p_corr (pressure correction)	p_rgh (dynamic pressure)	U (laminar velocity)
Solver	PCG (preconditioned conjugate gradient)	PCG (preconditioned conjugate gradient)	PBiCG (preconditioned bi-conjugate gradient,)
Preconditioner	DIC (diagonal incomplete-Cholesky, symmetric)	DIC (diagonal incomplete-Cholesky, symmetric)	DILU (diagonal incomplete-LU, asymmetric)
Tolerance	1e-10	1e-7	1e-6
Relative tolerance	0	0.05	0

The snapshots of water volume fraction in the rough channel shown in Figure 2-3 illustrate the results of simulations of the dynamic water displacement by air. Using the modified VOF method, the water-air interface is only slightly smeared. The interfacial velocity shows a positive correlation with the local aperture—the velocity is higher when the air-water interface is at places where apertures are larger (e.g., at times 3 s and 4 s), which is consistent with the experimental observations.

However, the predicted interfacial velocity is substantially (up to five times) larger than the experimental observations. Although the inlet boundary condition used in the simulation is different from the actual flow conditions at that location during the experiment, because the inflow is expected to be affected by upstream channel geometry and flow processes in the experiments, and it is unlikely that the changes in boundary conditions and refining the mesh size would explain such a large discrepancy.

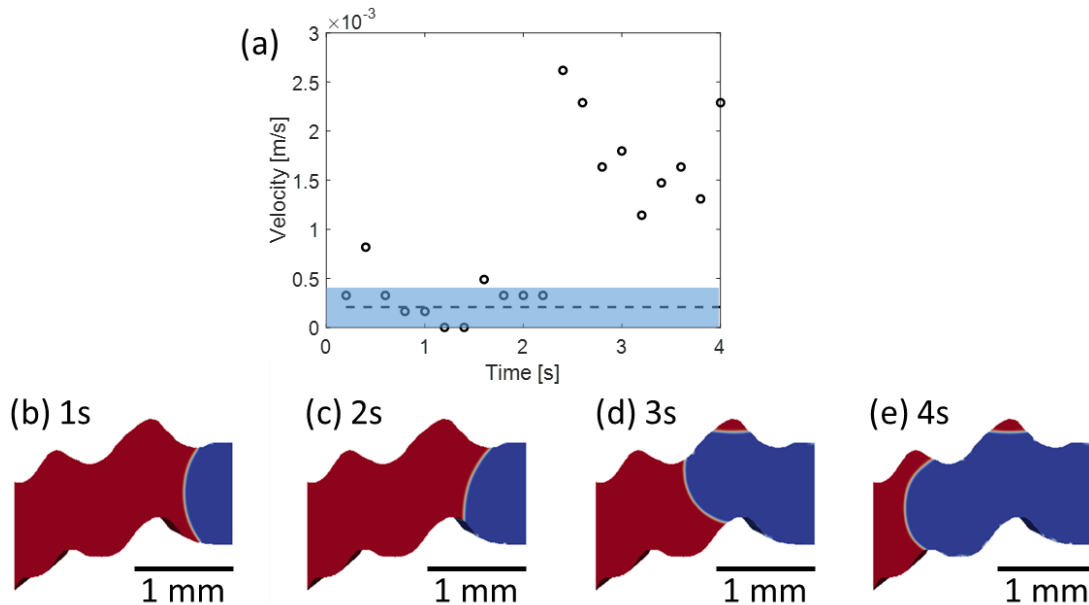


Figure 2-3. (a) Interfacial velocity from the results of numerical simulations, and (b)-(e) snapshots of the water-air interface predicted by the simulation. The blue band in (a) illustrates the variation of the gas phase volume observed in the experiment.

2.3.3 DISCUSSIONS

Both test cases highlighted the challenges of simulating two-phase flow systems dominated by capillary forces by means of the code *interFoam*. This can be explained by the presence of spurious currents at the air-water interface, which may be attributed to the imbalance of local forces, as the surface tension body force is represented using the continuous surface force method, and the inaccuracy of the local curvature estimated from the reconstructed interface (Deshpande et al., 2012; Hoang et al., 2012; Raeini et al., 2012; Nieves-Remacha et al., 2015). Several methods have been proposed to reduce the spurious currents, including (1) smoothing or filtering (Hoang et al., 2012; Raeini et al., 2012), (2) sharpening the interface by modifying the interfacial tension force model (Raeini et al., 2012), and (3) combining VOF with or using interface tracking method such as the level set method (Abu-Al-Saud et al., 2017). However, balancing the need of accurate interface representation, mass conservation, minimizing spurious currents and handling large density ratios are still challenging (Deshpande et al., 2012).

2.4 Pore scale characterization for simulations in actual pore structures

In order to examine the impact of pore structures on gas bubble migration, high-resolution characterization and quantification of pore structures are required. In this subsection, two types of rocks representing two drastically different types of pore geometries were analyzed: (a) a compacted clay material (Illite du Puy from Gaboreau et al., 2016), which has generally smaller pores and flatter pore geometry, and (b) a carbonate rock that has larger pores and a more granular structure.

The pore structures are to be used to generate computational meshes for direct numerical simulations in actual pore structures. The analyses also provide morphological information (e.g. pore/pore throat ratio, pore and pore throat shape factor) to constrain the generation of idealized pore and pore-throat geometry for numerical experiments of gas bubble migration, which can provide valuable information for upscaling.

The 3D data set of the clay material was collected using FIB-SEM (Focus Ion Beam Scanning Electron Microscopy) and has a voxel size of $5 \times 5 \times 5$ nm (Gaboreau et al., 2016). A subsection of the 3D data set ($150 \times 150 \times 180$) was analyzed using iMorph (<http://www.imorph.fr/>). The size of pore and pore throats were calculated from local aperture diameter, which was determined by the maximal ball diameter accommodated by the void space. The ratios between the half axis length of the equivalent ellipsoid provided measures of the aspect ratio of the pores and pore throats. The 3D volume of the carbonate rock was reconstructed from computed tomography images with a resolution of $16 \mu\text{m}$. A sub-volume of $350 \times 350 \times 150$ voxels was analyzed using the same approach.

Figure 2-4(a) shows the 3D rendering of the clay volume with a porosity of $\sim 30\%$. The pore bodies are well connected (Figure 2-4(b)), with an average diameter of 81 nm and a standard deviation of 21 nm. The pore throats show obvious flattened geometry (Figure 2-4(c)), with the size of 19 ± 8 nm. The pore size and pore throat size distributions are also shown in Figure 2-4(d). Figures 2-4(e,f) depict the aspect ratios of the pores based on the conceptual model of the equivalent ellipsoid, shown in Figure 2-4(g). The ratio between the lengths of different axes (a/b and b/c) varies mostly between 1 and 2. Approximately 3% and 9% of the pores have the a/b and b/c ratios larger than two, respectively. More than 40% of pores have the b/c ratio larger than 1.5.

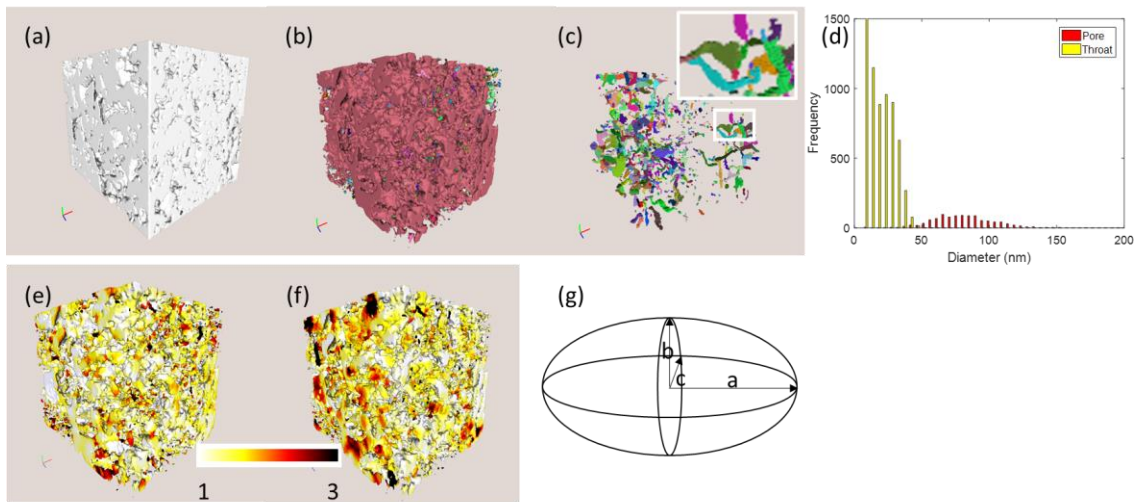


Figure 2-4. (a) 3D volume, (b) connected pore components, and (c) pore throats in the clay volume. (d) Distributions of pore and pore throat size. (e) Ratio a/b and (f) ratio b/c of equivalent ellipsoid. (g) Illustration of the equivalent ellipsoid.

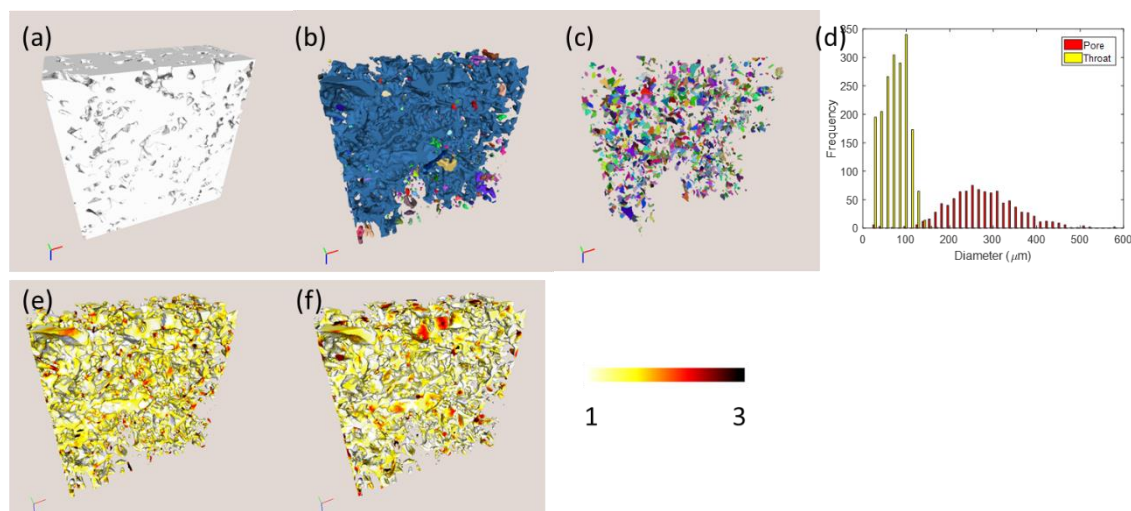


Figure 2-5. (a) 3D volume, (b) connected pore components, and (c) pore throats in the carbonate volume. (d) Distributions of pore and pore throat size. (e) Ratio a/b and (f) ratio b/c of the equivalent ellipsoid.

The carbonate (with porosity of 18%) has larger pores and pore-throats (Figures 2-5(b,c,d)). The pore sizes and pore throats are $281 \pm 78 \mu\text{m}$ and $74 \pm 29 \mu\text{m}$, respectively. However, the ratio between pore and pore throat (3.6) is comparable to that of the clay sample (3.9). The pore geometry is also more rounded as indicated by the lighter color on Figures 2-5(e,f). Less than 2% and 3% of the void space has a/b and b/c ratio larger than two.

2.5 Future Work

In the upcoming fiscal year, three tasks will be performed. First, the modeling approach will be modified to ensure accurate simulation of low capillary number conditions typical for the nuclear waste disposal systems. In particular, two methods will be evaluated – the semi-sharp surface model (Raeini et al., 2012) and the coupling with level-set method (Abu-Al-Saud et al., 2017). Second, pore and pore throat geometries extracted from real rock images presented here will be compared with characteristics of the pore structures of crystalline rocks, to ensure the relevance of the numerical simulations to nuclear waste disposal in crystalline rocks. Third, simulations will be performed to investigate gas bubble migration using representative pore and pore throat geometries with an emphasis on investigating the extent of interface velocity and transient pressure variations. Simulations based on idealized geometries based on morphological statistics will provide insights regarding the controls of pore morphology on gas migration. In the long run, this study will provide necessary expertise and tools for investigations that are also highly relevant to at least two other tasks within the project: (1) dynamic evolution and migration of gas bubbles in the presence of abiotic reactions and microbial activities, and (2) local pressure perturbation (dissipation and buildup) and the geomechanical responses.

3. LABORATORY AND MODELING STUDY ON EDZ

3.1 Introduction

The primary objectives of the laboratory EDZ experiments are to investigate (1) the geometry of the damage around a circular excavation (tunnel/borehole breakout, tensile fracturing) within crystalline rock under high stress, (2) hydrological properties of the damage zone, and (3) the hydrological-mechanical-chemical (HMC) changes of the damage zone and the seal materials (e.g., bentonite, cement), which are expected to be caused due to diffusion and transport of pore fluid once the seal is placed within the excavation.

One major challenge of conducting laboratory study of EDZ development is the large scale differences between laboratory samples and tunnels and boreholes produced in the field. Fracturing and breakout of rock can be strongly dependent upon the mineral grain size (e.g., Duan and Kwok, 2015) and initial flaw size distribution (e.g., Martin et al., 1994). Typical laboratory experiments using a small hole (a model of a borehole or a tunnel) with a diameter up to a few centimeters could result in underestimation of the rock strength and in possibly a wrong design of EDZ properties.

In crystalline rock, it has been found that the stress along the rock surface (tangential, or hoop stress) for initiating breakout of a circular excavation strongly depends upon the diameter. From experiments using Lac du Bonnet granite, it was found that for small, laboratory-scale boreholes, the breakout stress can be 2.5 to 3 times larger than the stress predicted by the uniaxial compression strength of the rock, and this ratio gradually reduce to 1 with increasing diameter (Figure 3-2). Comparison to the breakout of a much larger, field-scale tunnel observed at the URL (Atomic Energy of Canada Limited Underground Research Laboratory mine-by experiment at 420 level) showed the scale effect levels off for hole diameters larger than 50 to 100 mm for this granite (Martin, 1997).

In FY2018, we conducted a series of laboratory EDZ formation experiments (borehole breakout study) on granite slabs with a specially designed geometry (e.g., Nakagawa and Ewy, 2008). The surface of these samples was curved, which induced stress concentration similar to a circular excavation with a diameter of ~0.5 m. Additionally, because only uniaxial loading is required to conduct these tests, very large stress (a few hundreds of MPa) was applied to the sample easily. During these experiments, acoustic emissions and seismic velocity changes caused by microcrack formation were monitored. Because the sides of these samples were either exposed or under only small confining stress, the development of the EDZ was also

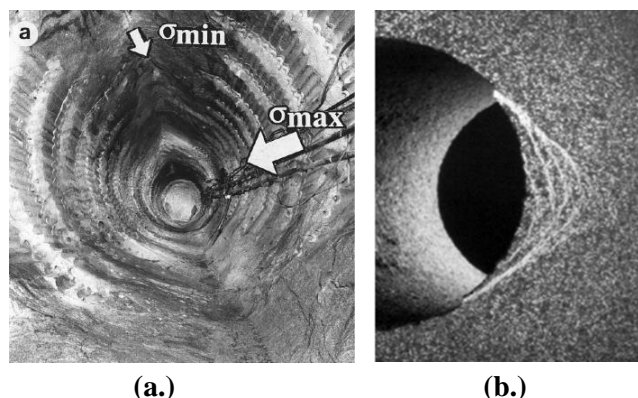


Figure 3-1. EDZ at different scales. (a) Large-scale EDZ in a 3.5-m diameter mine tunnel (Martin, 1997); and (b) cm-scale borehole breakout (in Berea sandstone) observed in the laboratory.

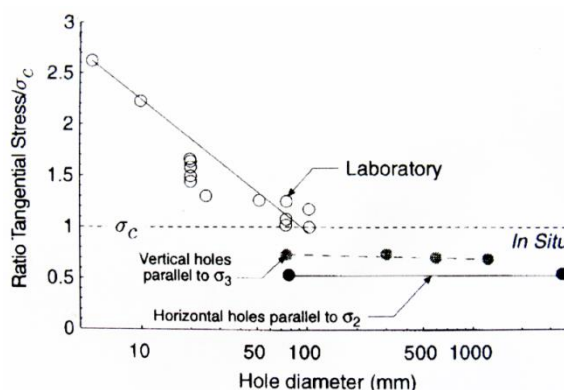


Figure 3-2. Size effect of breakout observed in the laboratory (Martin, 1997).

visualized in real time. In the post mortem examination, more detailed seismic velocity measurements in the sample including characterization of crack-induced shear wave anisotropy, microscope observation of thin sections, and permeability measurements of subcored samples were conducted.

In the following, we will first describe the samples used in the experiments, followed by a description of the experimental procedures. Next, the results of the laboratory experiments are presented, including the visual images of EDZ development, acoustic emission history and located events, seismic velocity changes, post-mortem thin section images, and permeability measurements. Newly started effort for numerical modeling of EDZ development using TOUGH-RBSN (Rigid-Body-Spring-Network) model is also described, which will be used to interpret the laboratory experiments in the future. Lastly, the lessons learned from this study and the next research step will be provided.

3.2 EDZ Experiments Using Shaped Rectangular Sample

3.2.1 Experimental Setup

3.2.1.1 Test Samples

The rock samples used in the experiments are four shaped, fine-grained Westerly granite slabs (Figure 3-3). Only three of the four are shown in Figure 3-3. The original rectangular slabs used for the experiments were 10.24-cm tall (H), 5.08-cm wide (W), and 2.54-cm thick (T). On the sides of the slabs, concave cuts of a radius 25.4 cm were made using a diamond grinding wheel. Two-dimensional stress analysis of axial loading for samples with this geometry was performed using a 2D linear-elastic, plain-strain finite-element model (LISA ver.8.0.0. <http://www.lisa-fet.com/>). In the model, the rock's Young's modulus and the Poisson's ratio were assumed to be 72 GPa and 0.25, respectively. 200 MPa of axial compression was applied at the top, resulting in the distributions of vertical stress σ_{zz} and horizontal stress σ_{xx} shown in Figure 3-4. Note that the model is for one-quarter of the actual sample because of the symmetry, with zero vertical displacement at the bottom and zero horizontal displacement at the right edges of the model. Also the compression has negative values, and tension has positive values in these plots. Note that the color scales are relative and stretched over the stress range of interest.



Figure 3-3. Photograph of shaped Westerly granite slabs used for the experiment.

Axial loading on a horizontally unconstrained sample produces large stress concentration near the curved surface, but also induces horizontal tensile stress at the top end. As will be shown in Section 3.2.2.1, this causes undesirable, premature tensile fracturing of the sample. To mitigate such failure, in the experiment, the lateral deformation was constrained by attaching (gluing for a lab sample) a hard, metal footing to the ends. In the numerical model, a steel section was added to the rock model with a welded interface. Comparison of the stress distributions before and after a 2.54-cm thick alloy steel bar was attached to the sample is shown in Figure 3-5. Although this slightly reduces the stress concentration in the sample, the tensile stress in the sample (positive stress concentration in the plots) is eliminated. Comparisons between stresses along the minimum horizontal stress line (along the bottom of the model shown in Figure 3-5) of the shaped slab sample and a tunnel/borehole (theoretical Kirsch solution [Kirsch, 1898]) within an infinite medium with a far-field compressional maximum stresses ratio of $(\sigma_{xx}^{\infty}, \sigma_{zz}^{\infty}) = (100 \text{ MPa}, 200 \text{ MPa})$ are shown in Figure 3-6. Note that, along the center line, $\sigma_{xx} = \sigma_{rr}$ (tunnel/borehole radial stress) and $\sigma_{zz} = \sigma_{\theta\theta}$ (hoop stress). What we wanted to examine here was how close the relative stress distribution in a shaped slab would correspond to conditions at a field excavation with a circular cross section. The stress

concentration factor here is defined as the stress normalized by the far-field vertical stress σ_{zz}^{∞} , which is ~ 2.5 for the tunnel/borehole. In order to compare the distributions of the stress concentration between the shaped sample and the tunnel/borehole, for the shaped slab, the curves' vertical scales are adjusted by the same factor for both vertical and radial stresses to match the maximum stress concentration factors on the wall (at a radial distance 25.4 cm from the tunnel/borehole center). The actual maximum stress concentration factor was ~ 1.20 times the applied axial stress, which implies that in the laboratory $2.5/1.20 \sim 2.1$ times the far-field vertical stress is required to introduce near-wall stress state similar to a field borehole/tunnel. Based on these results it is anticipated that the stress state near the expected breakout location of the shaped slab sample can be similar to a large-diameter excavation with the same surface curvature, and that constraining the lateral deformation using a steel block on a shaped sample of granite-like rock would mitigate tensile fracturing while having only small impact on the stress concentration.

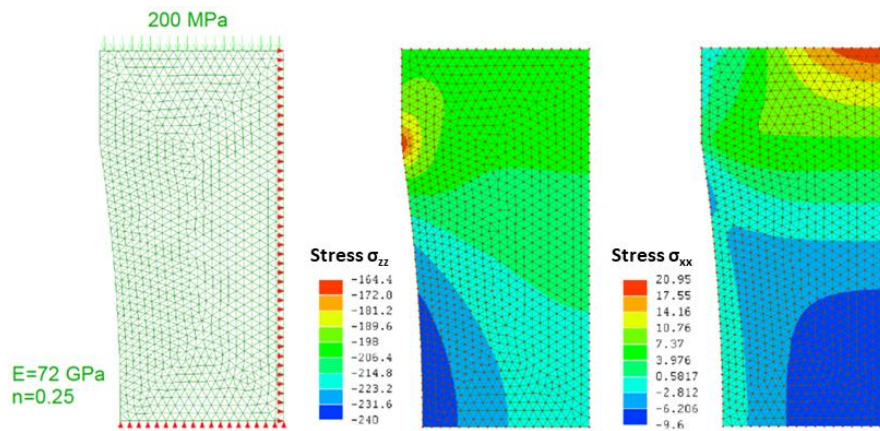


Figure 3-4. 2-D finite element stress analysis using LISA. Only one quarter of the actual sample is modeled due to the symmetry. The top boundary is not constrained, and the uniform axial stress is applied on it.

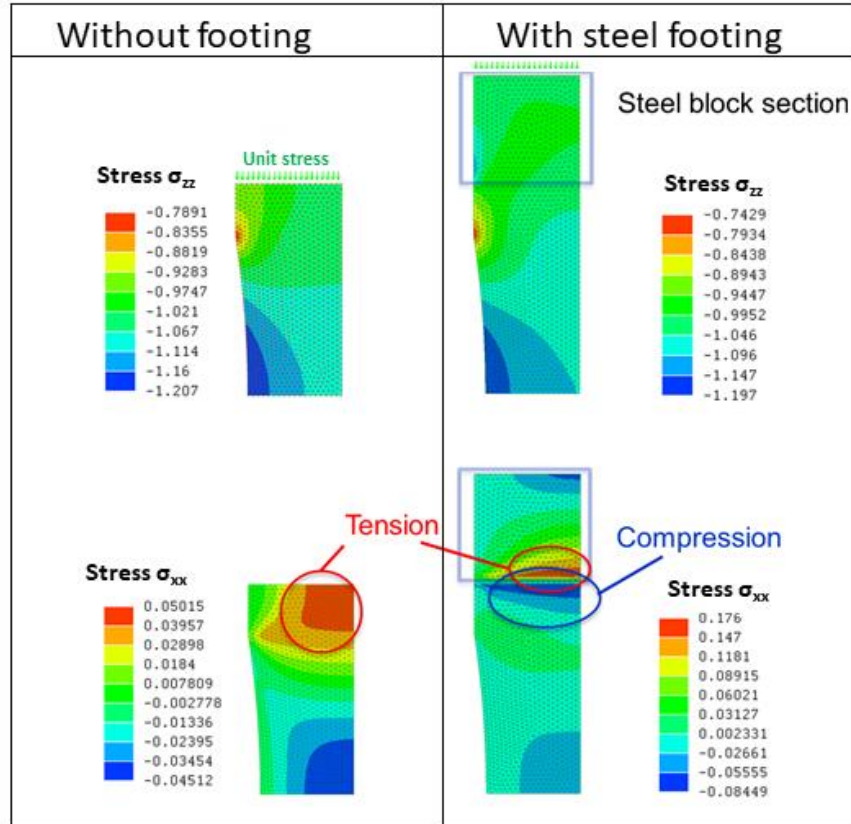


Figure 3-5. 2D finite element stress analysis of the effect of steel footing attached to the end of a shaped slab sample. The stress resulting from unit compressive stress at the top (i.e., the stress concentration) is shown.

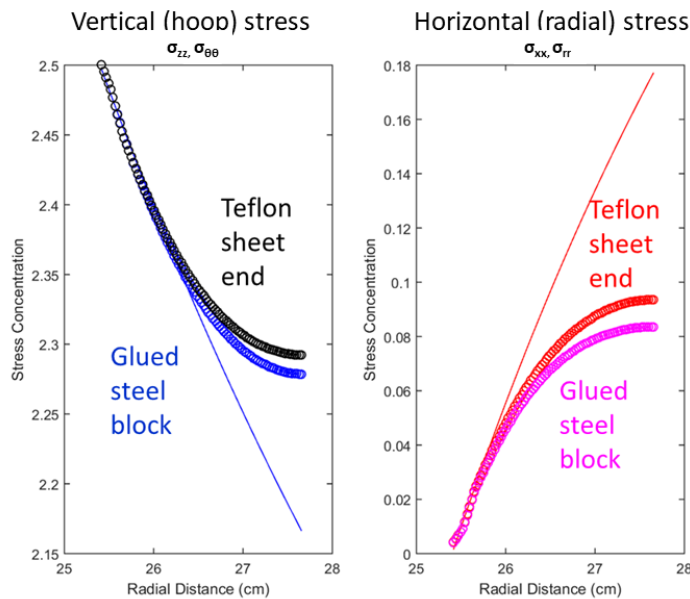


Figure 3-6. Comparisons between stresses along the minimum horizontal stress line (along the bottom of the model shown in Figure 3-5) of the shaped slab sample and a borehole within an infinite medium with a far-field compressional maximum stresses ratio of $(\sigma_{xx}^{\infty}, \sigma_{zz}^{\infty}) = (100 \text{ MPa}, 200 \text{ MPa})$, which is represented by solid lines in plots. Note that, along the center line, $\sigma_{xx} = \sigma_{rr}$ and $\sigma_{zz} = \sigma_{\theta\theta}$. The vertical scale is adjusted for the shaped slab sample. Actual max. stress concentration factor for the slab is ~ 1.20 times (instead of $2.5 \times$) the applied axial stress. The ‘Teflon’ curves represent the case when the sample top has no lateral constraints.

3.2.1.2 Test System

The experiments were conducted using a polyaxial loading system consisting of a high-loading-capacity Z frame and a small-capacity, lateral X - Y frame. Both of them are equipped with hydraulic cylinders to control the principal stress along each loading axis (Enerpac RSM1500 [Z] and Symplex R101 [X and Y], respectively) (Figure 3-7). The hydraulic fluid pressure and flow were controlled by two ISCO syringe pumps. The shaped slab samples were loaded in the Z direction to induce damage in the rock, while much smaller stress was applied in the X direction. During the tests, transparent acrylic blocks were attached to the X surfaces of the sample. There was no stress applied in the Y direction. The acrylic blocks were used to (1) transmit X -direction stress to the slab to provide small confining stress and to support the sides of the sample, (2) serve as an optical window for real-time imaging of the EDZ development, through a 37-mm diameter porthole in the X - Y frame, and to (3) house small acoustic emission sensors (Score Atlanta Inc, PICO Z sensors, frequency band 200 kHz-800 kHz) for acoustic emission monitoring and event location. The acrylic blocks and the sample surfaces were mediated by a thin PTFE film to minimize the friction. The Acoustic Emission (AE) transducers were placed in direct contact with the rock sample through 5mm-diameter holes in the film, with petroleum wax used to establish good acoustic coupling. The AE data collection and processing was performed in real time using an AMSY-6 acoustic emission measurement system (Vallen Systeme). The AE waveform data, when collected and stored, were later used for more careful arrival time analysis and event location.

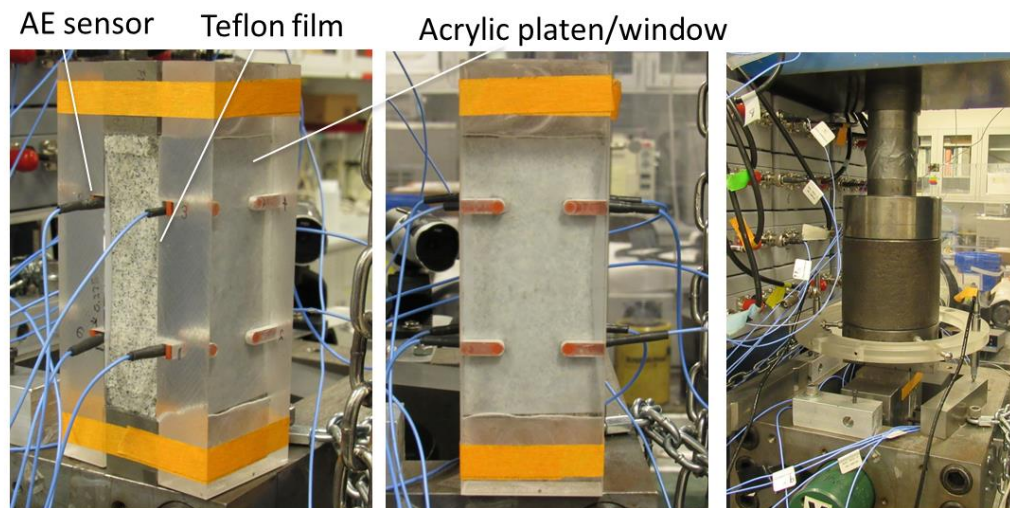


Figure 3-7. Bi-axial loading test on a shaped slab of Westerly granite. Acoustic emissions were monitored concurrently with the loading tests. 8 sensors are embedded within grooves in a pair of transparent acrylic loading platens attached to the X surfaces of the slab, mediated by a PTFE (Teflon) film. During the test, large axial (Z) stress was applied while only small confining stress in the X direction was applied and held constant.

3.2.2 Experimental Results

3.2.2.1 Loading Test Results

The three slab samples (Figure 3-3) were loaded under room temperature and room-dry conditions. The first Sample Z-1 was loaded with a slightly higher X -direction stress ($\sigma_x=9.5$ MPa) than the other two samples, and no steel footing was used (the boundary between the rock sample and Z -direction steel loading platens was mediated by a PTFE film). Preliminary FEM modeling indicated that this resulted in primarily axial splitting of the sample, which originated at the sample-platen boundaries. Also, the resulting ultimate strength of the sample was ~ 160 MPa, smaller than the other samples (Figure 3-8).

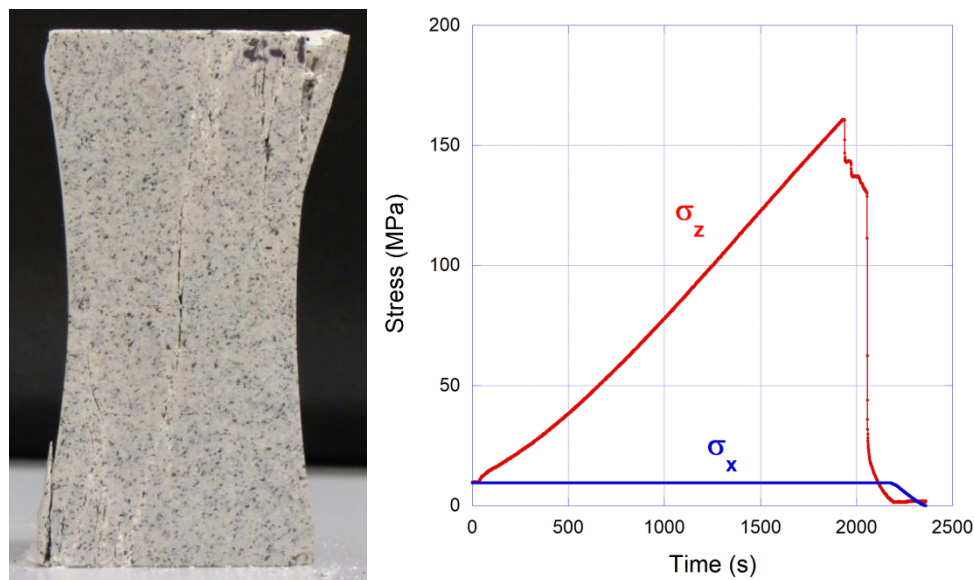


Figure 3-8. Loading test on shaped slab Sample Z-1 without steel footings. The failure of the sample was caused by axial splitting, with the ultimate strength of the sample of 161 MPa.

Next, to avoid the axial splitting, a pair of steel footings (2.54 cm × 2.54 cm × 5.08 cm) were glued to the top and the bottom ends of the remaining samples with epoxy resin. Also, the X-direction confining stress was reduced to 2 MPa. After a large number of acoustic emissions were detected, Sample Z-2 was temporarily unloaded from ~170 MPa to ~70 MPa (Figure 3-9). The maximum applied stress was 208 MPa, and the sample was not brought to the ultimate failure. The photograph to the right shows a close-up view of an observed surface spalling (breakout) on one side (left edge of the sample shown in Figure 3-9 left).

The last Sample Z-3 was loaded under the same conditions as Z-2, but additional measurements were conducted, and the sample was brought to ultimate failure. During these tests, step-by-step loading was applied (Figure 3-10) to conduct active seismic velocity measurements between the sensors (note that the results are not shown in this report). The AE waveforms developed during this test were collected for conducting careful travel time determination and location analysis. Additionally, Z-direction deformations of the sample were measured using a pair of vertical LVDT sensors. In this experiment, after reaching the maximum axial stress of 208 MPa at the sample top, the sample started to exhibit slow plastic deformation, while the axial loading pump was stopped. Due to the compliance in the system, both the reduction in the axial stress and the increase in the compaction are seen in Figure 3-10 (between ~4,300 s and ~5,000 s). At ~5,000 s, the sample failed catastrophically. The mode of the resulting damage induced in the sample was splitting and buckling failure (Figures 3-10 and 3-11), which is typical for compression-induced tunnel/borehole wall breakout. Still images (snapshots) extracted from a video recorded during the creep stage of the loading test are shown in Figure 3-12.

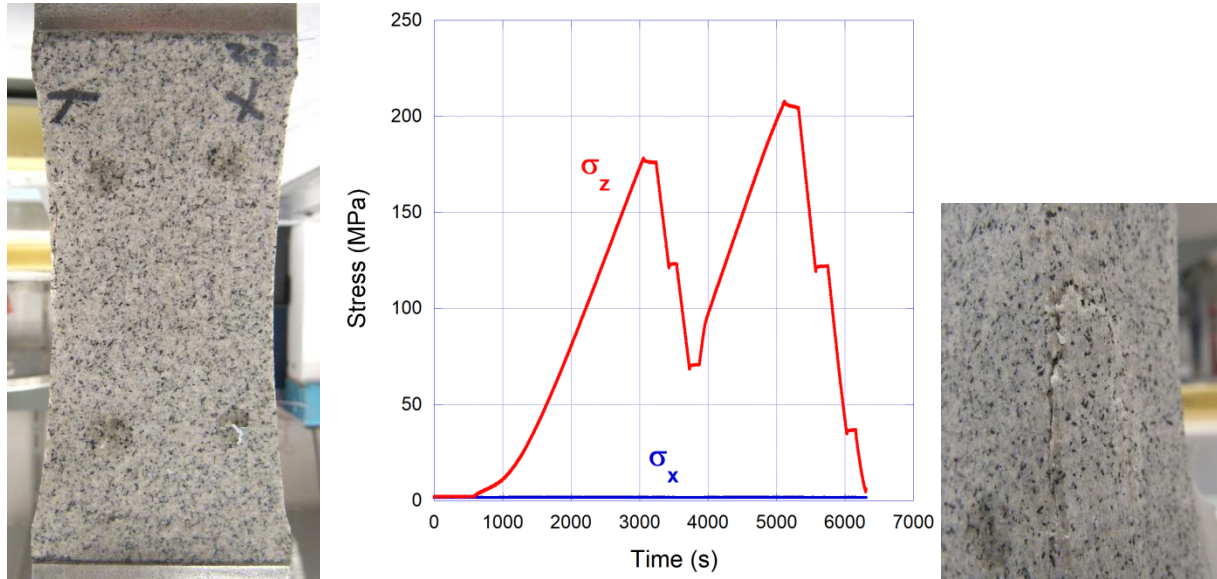


Figure 3-9. Loading test on shaped slab Sample Z-2 with steel footings. The sample was temporarily unloaded from ~170 MPa to ~70 MPa after a large number of acoustic emissions were detected at T~3,000 s. The maximum applied stress was 208 MPa, and the sample was not brought to the ultimate failure. The photograph to the right shows a close-up view of surface spalling (breakout) caused by the axial loading.

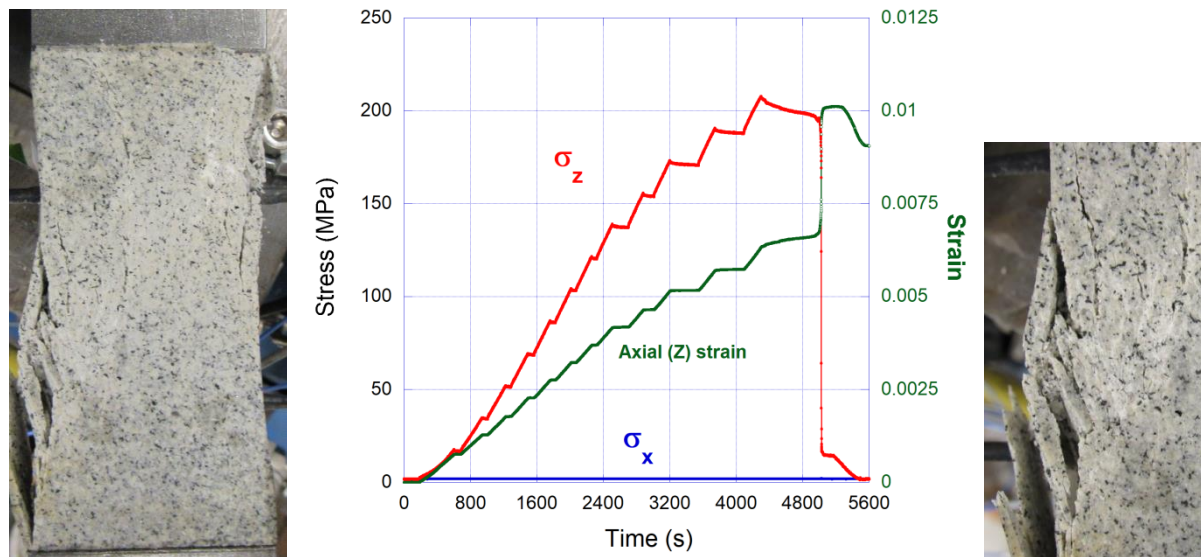


Figure 3-10. Loading test on shaped slab Sample Z-3 with steel footings: Left—the photograph of the sample before the test; middle—graphs of the stress vs time during the test; and right—the photograph of the sample loaded by steps up to ~208 MPa, when the strong, creep deformation occurred, showing a visible, continuous fracture development on the slab surface. Without further increases in load, the ultimate failure was reached at T~5,000 s. The photographs indicate axial-splitting and buckling failure, typically seen on a tunnel and borehole wall suffering EDZ development, and a diagonal shear band which led to the ultimate loss of the load-bearing capacity of the sample.



Figure 3-11. Side view of axial-splitting and buckling failure in Sample Z-3.

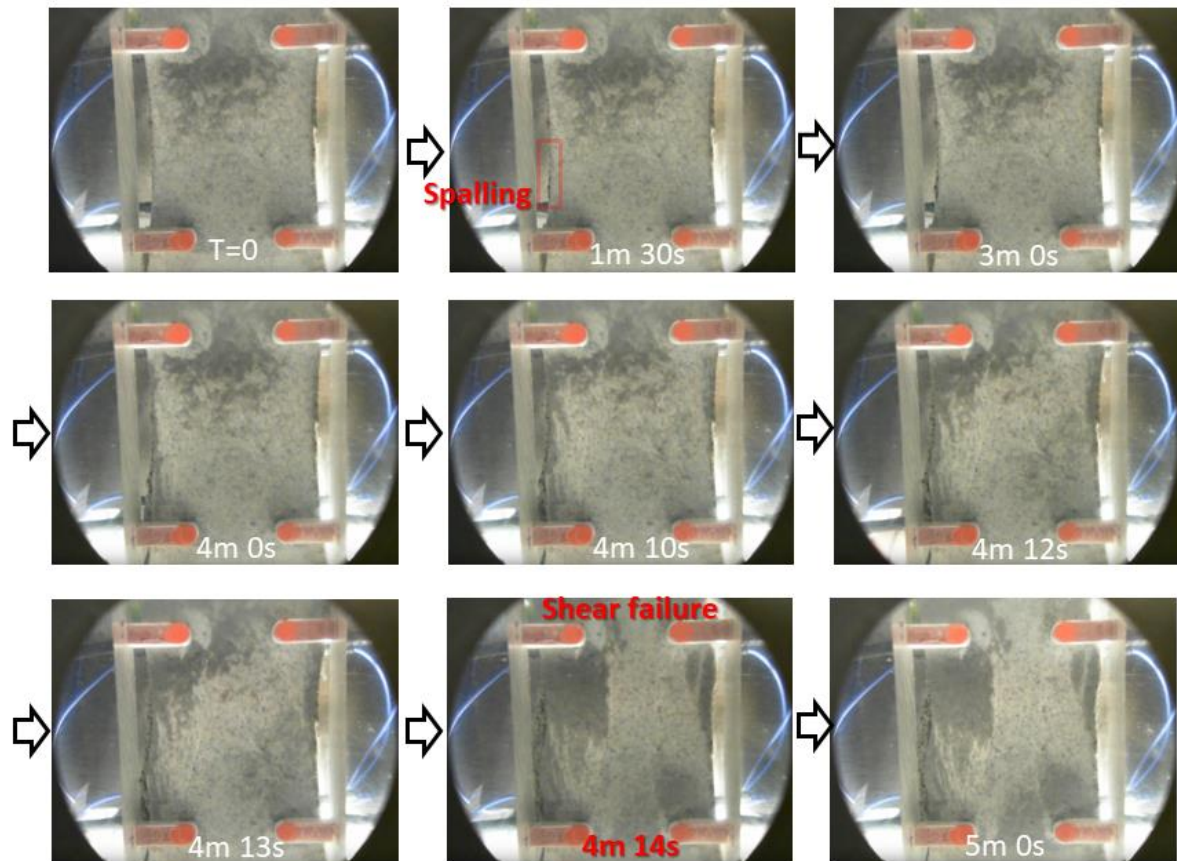


Figure 3-12. Snapshots of the EDZ (breakout) development during the slow creep deformation started at $T=4,300$ s. Note that the time stamps are the elapsed time after the recording was started at $T=4,750$ s.

3.2.2.2 Geophysical (Seismic) Measurement Results

Acoustic emission measurements

Acoustic emissions, which are primarily caused by creation and extension of microcracks due to damage in the samples, were monitored during the loading tests.

For Sample Z-1 (Figure 3-13), initially, the rate of AE activity increased monotonically as the axial load was increased. The AE rate apparently reduced once the rate reached ~ 200 counts per second (note that for this sample only two AE sensors were used). This is because the AE data acquisition system became saturated after the per-sensor count reached ~ 100 . It typically takes a few minutes before this system recovers after the saturation, so that the following AE rate measurements become unreliable. Also the dots shown in magenta indicate high background noise during measurements, which typically happens when the individual events cannot be distinguished from each other, because too many events are occurring close to each other. Although quantitative information cannot be obtained from such data, qualitatively, this high background noise indicates extremely strong AE activity.

The experiment on Sample Z-2 was conducted using 8 sensors. During the initial loading, the AE activity increased rapidly at $\sim 3,000$ s. At that time $\sigma_z \sim 175$ MPa, the loading was stopped, which resulted in immediate reductions in the AE activity. Once the sample was unloaded down to ~ 125 MPa, and then to ~ 70 MPa, the AE activity became very quiet. Upon second loading, strong AE activity did not resume until the load reached the previous level of ~ 170 MPa. This behavior is well known as the Kaiser effect (e.g., Lavrov, 2003). After this, the AE rate reached near or above the maximum system capacity at $\sigma_z \sim 208$ MPa, and the activity did not decrease until the load was reduced to 125 MPa. Although the ultimate failure was not observed in this experiment, the AE activity indicated that a significant level of damage was introduced in the sample.

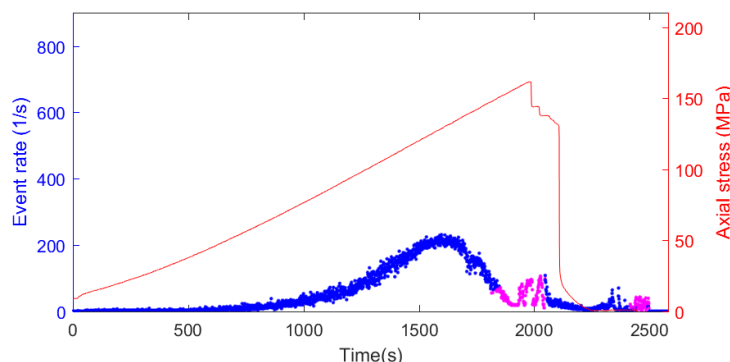


Figure 3-13 Acoustic emission event rate (number of detected events per second) history through the experiment on Sample Z-1. The corresponding axial stresses are also shown. The sudden decrease of the AE counts after reaching 200 counts per second, and the dots in magenta, indicates that the sensors and the measurement system were overwhelmed by an extremely large number of AE events which saturated the measurement capacity.

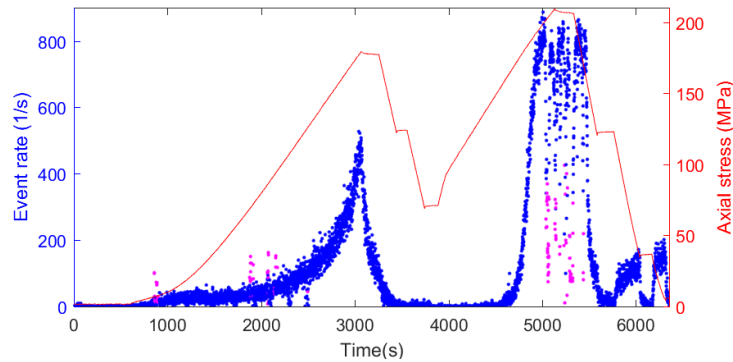


Figure 3-14 Acoustic emission event rate (number of detected events per second) history through the experiment on Sample Z-2. The corresponding axial stresses are also shown.

In the third experiment (Sample Z-3), a very large number of AE waveforms were collected at multiple time intervals for later AE wave arrival time analysis and event location (Figure 3-15). Up to the point where the system was saturated with 800 counts per second (or 100 counts per second for each sensor channel), the step loading resulted in triangle-shaped event history curves, in which the cusps corresponded to the time when the load increase was stopped. In this experiment, again, the loading was stopped at 208 MPa. At this point, extremely strong AE activity was already in progress, saturating the system (the system did not fully recover until $T \sim 4,830$ s, when the ultimate failure was reached). The spatial locations of the events computed from the collected AE waveforms for each time interval are also shown in each panel in Figure 3-15. Note that the view angle is from the back side of the sample shown in Figure 3-10. The red dots indicate shear-dominant events, blue opening-closing events, and black unclassified events due to the lack of sufficient data to compute a moment tensor (which is used to classify the event type). Note that there is only a small number of the blue events occurred in this experiment compared to the others, but they are difficult to see in these figures. Surprisingly, the overall event location distribution in the sample did not change at different stages of the loading, exhibiting a diagonal band corresponding to the shear failure band seen in Figure 3-10. More events did seem to occur at and near the location of the breakout however, as indicated in Figures 3-15 (d,e).

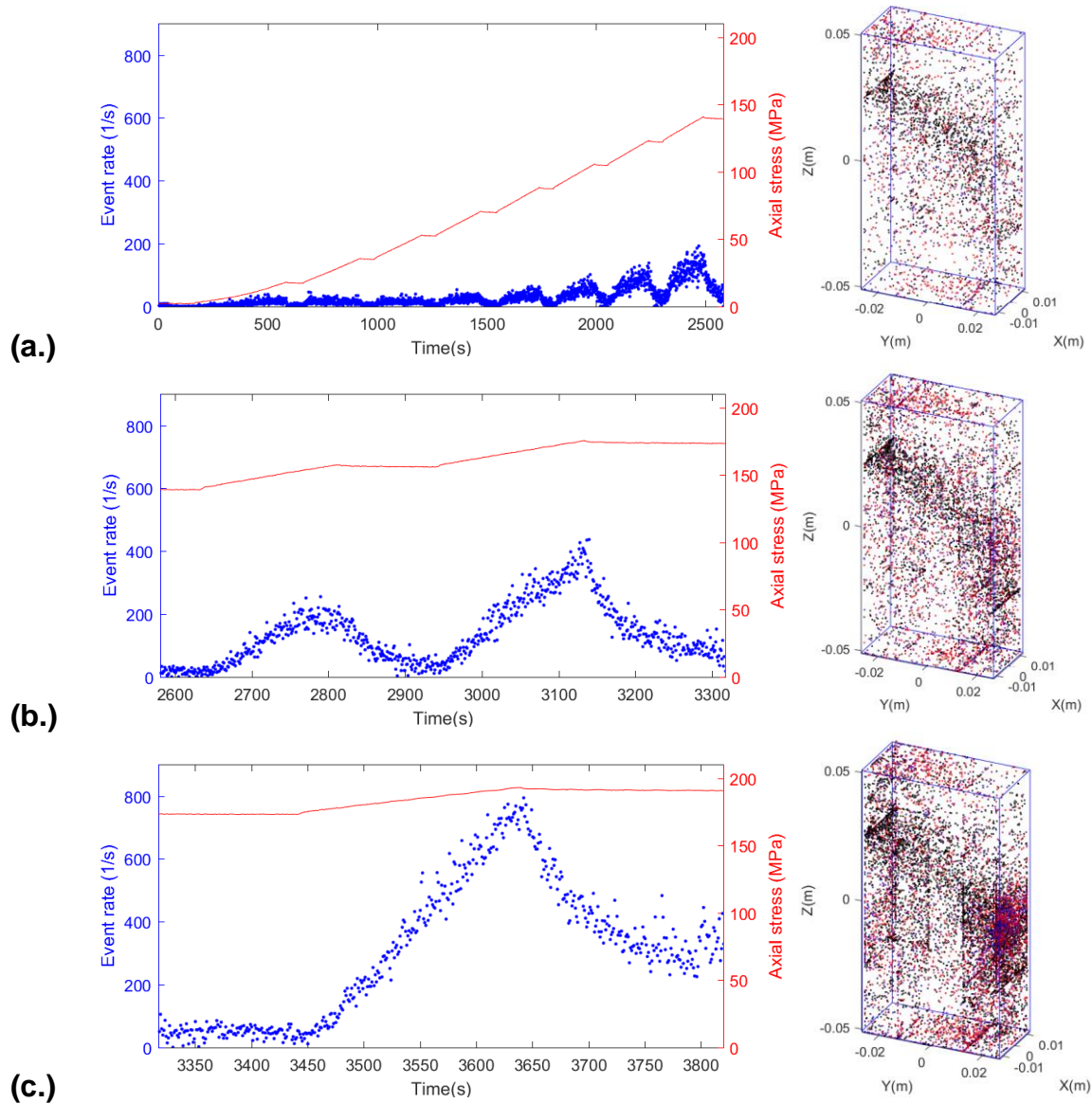


Figure 3-15. Acoustic emission event rate (number of detected events per second) history throughout the experiment on Sample Z-3. The corresponding axial stresses are also shown. Note that, compared to Figure 3-10, the view in these plots are from the back side of the sample shown in the photograph in Figure 3-10.

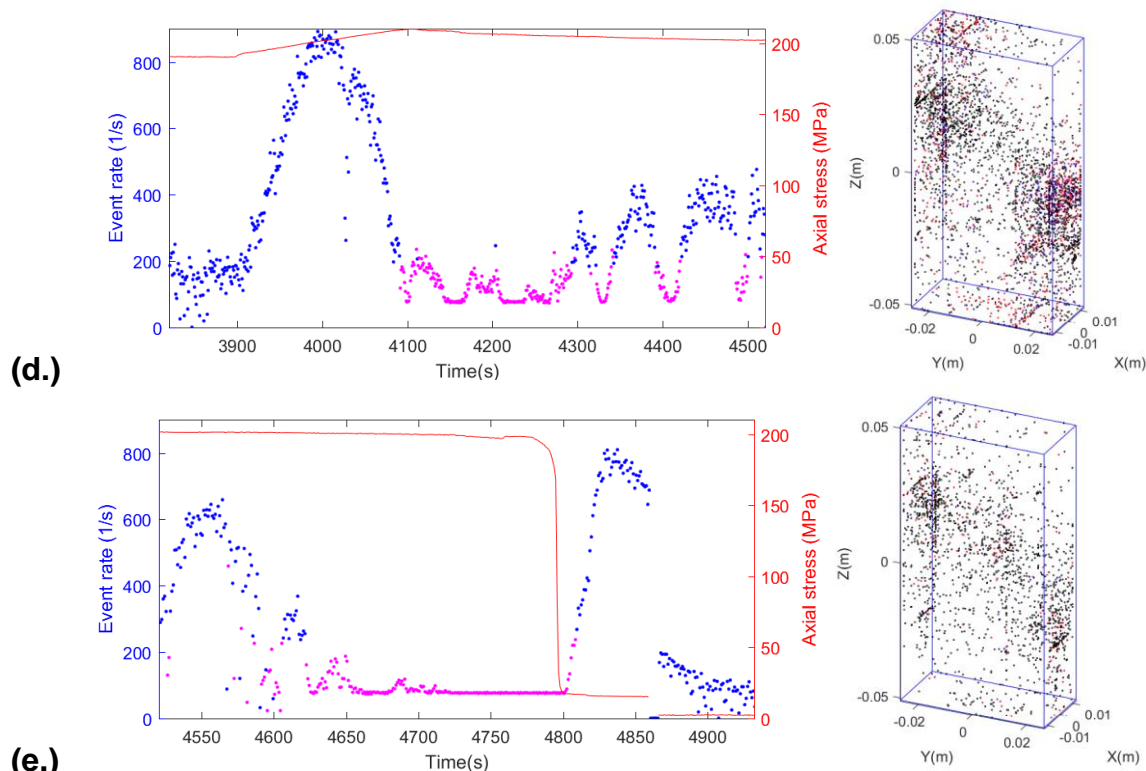


Figure 3-15. (Continued) Acoustic emission event rate (number of detected events per second) history throughout the experiment on Sample Z-3. The corresponding axial stresses are also shown. The data acquisition system saturated after ~4,000 s due to extremely strong AE activity. In the location plot, higher activity did seem to focus near the edges of a diagonal shear zone.

Post-mortem seismic velocity measurements

For Sample Z-2, seismic velocity measurements were conducted across the thickness of the slab sample using pairs of ultrasonic transducers with a central frequency of 1 MHz — Panametrics Accuscan (to measure the P-wave) and Vibroscan (to measure the S-wave). For the S-wave measurements, the direction of the wave polarization was aligned with either Z direction (vertical axis of the slab) or Y direction (horizontal axis of the slab), shown in Figure 3-16. The measurements were conducted at 1-cm intervals along three parallel lines along the Z axis, separated from each other by 1 cm. The determined velocities were compared to the same measurements for an intact, sister sample (Sample Z-4), which were cut from the same host block of Westerly granite, from which the other slab samples were produced.

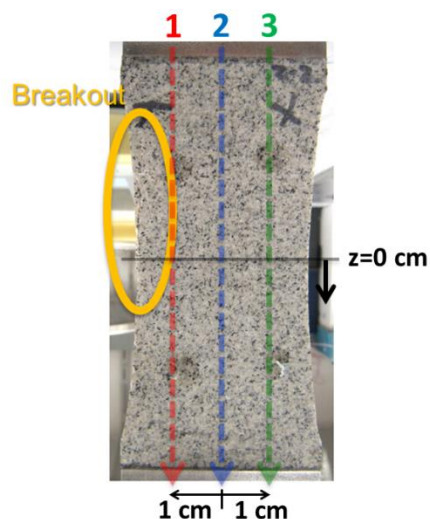


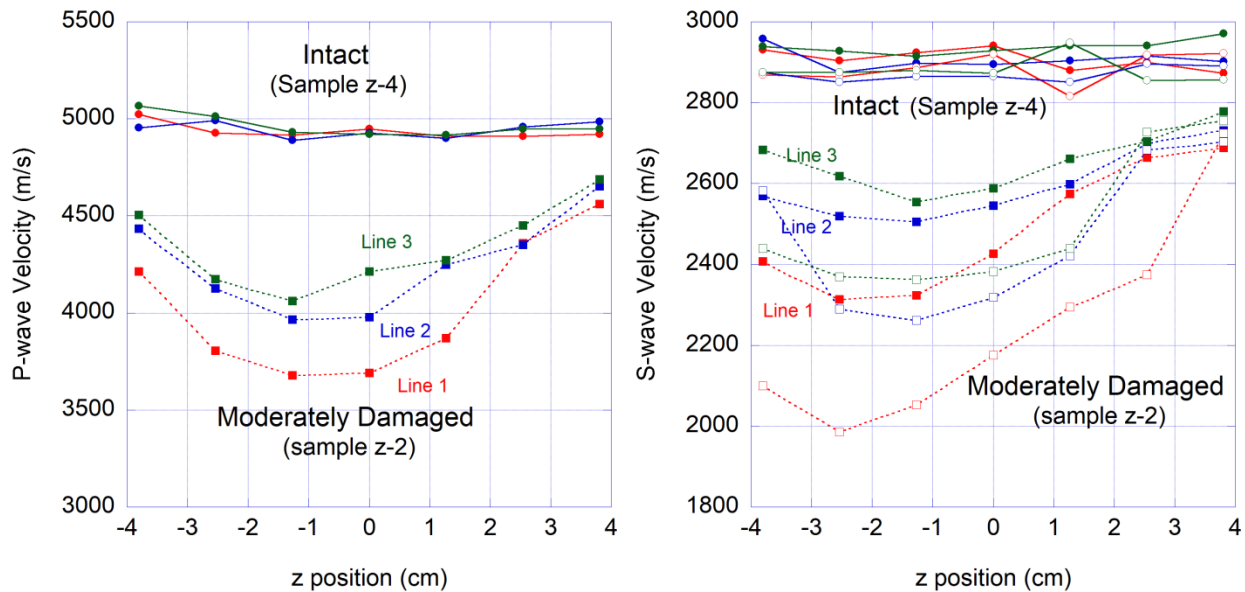
Figure 3-16. Seismic-velocity scan lines on Sample Z-2.

Seismic velocities determined for Samples Z-2 (moderately damaged) and Z-4 (intact) are shown in Figure 3-17. In Figure 3-17(a), compared to the intact sample, damaged sample exhibited very large decrease in both P and S wave velocities, particularly for Line 1 and near the location of the observed surface spalling (at from Z=-2 to -1 cm). It is interesting to see, however, that the seismically detected damage zone far extends into the interior of the rock, in spite of the intact exterior appearance of the sample. This result is consistent with the observation of the widely distributed acoustic emission locations in the severely damaged Sample Z-3, discussed in the previous section, even at stress levels much less than the failure strength of the sample.

The large differences in the velocities of two polarized S waves indicate the presence of cracks oriented along the Z axis (near parallel to the X-Z plane). In Figure 3-18, Thomsen’s γ parameters (S-wave anisotropy parameter) are shown, defined by

$$\gamma = \frac{V_{S,fast}^2 - V_{S,slow}^2}{2V_{S,slow}^2} \tag{3.1}$$

Note that the fast S wave here is defined as the Z-polarized S wave, and the slow S wave is defined as the Y-polarized S wave (so γ can take a negative value). Consistently with Figures 3-17(a) and (b), the damaged sample exhibited strong S-wave birefringence, with the Line 1 and the locations near the spalling, indicating larger anisotropy.



(a.) P-wave velocities

(b.) S-wave velocities (open symbols=Y polarized, closed symbols=Z polarized)

Figure 3-17. P and S-wave velocity distributions within an intact (Sample Z-4) and moderately damaged (Sample Z-2) slabs.

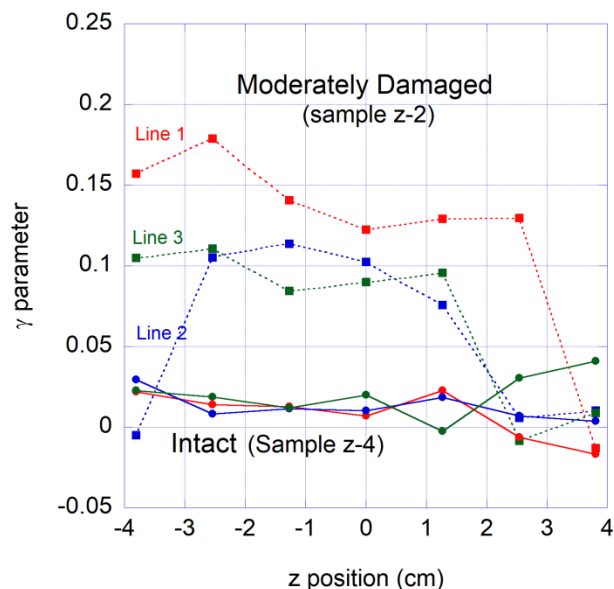


Figure 3-18. S-wave velocity anisotropy of Sample Z-2. Thomsen's γ parameter is shown.

3.2.2.3 Permeability Changes Due To EDZ Development

The acoustic measurements on Sample Z-2 indicate development of microcracks indicating an extensive damage of the rock far away from the surface, even though visually no damage was induced in the rock. To examine the actual impact of the damage on permeability of the rock, direct permeability measurements were conducted on small core samples (diameter 13.9 mm, length 25.4 mm) taken from different locations of the slab sample (Figure 3-19). Additionally, thin section samples (sections M1, M2, and M3) were made from the remaining parts of the slab, to examine the geometry and location of the microcracks via optical microscopy.

The permeability measurements were conducted via a flow-through test using a small triaxial test cell (Figure 3-20). In this test, a small, dry cylindrical core, with stainless steel mesh placed at both ends of the sample, was jacketed and placed within a confining vessel. The cavity and the fluid line at the bottom side of the sample were saturated by water prior to the experiment. Subsequently, an axial stress of 6 MPa (884 psi) and a confining stress of 0.17 MPa (25 psi) were applied to the sample, and an upstream pressure of 0.1 MPa (15 psi) was applied to flow the water through the core. The resulting changes in the volume of the injected water were monitored over 20 to 24 hours (Figure 3-21(a)). Although we tried to maintain the pump pressure at 0.17 MPa (25 psi), imperfect servo control and possible temperature fluctuations of the system resulted in occasional temporal overpressurization (Figure 3-21(b)) due to the increased fluid volume in the system. This seems to correlate with the observed irregular changes in the injected fluid volume, which did not allow for reliable permeability estimation. Nonetheless, the high flow volumes did correlate well with the expected degree of damage of the core, with the left side of the sample (L1–L4) and the locations near the surface damage (L1–L3) exhibiting higher permeability. High accuracy estimation of permeability is not reliable because complete saturation of the cores was not assured, which can be made possible by applying higher pore pressure and via longer-term monitoring of the flow rate changes. However, if the cores are assumed to be saturated by the injected water, the values obtained from the slopes of the flow volume history range from 5.7 μD to 14.2 μD , under a pressure gradient of 6.7 MPa/m (or 25 psi/inch). The reductions in the flow volume after 20 hours for Samples R2, R3, and R4 are possibly due to thermal expansion of the fluid in the system.

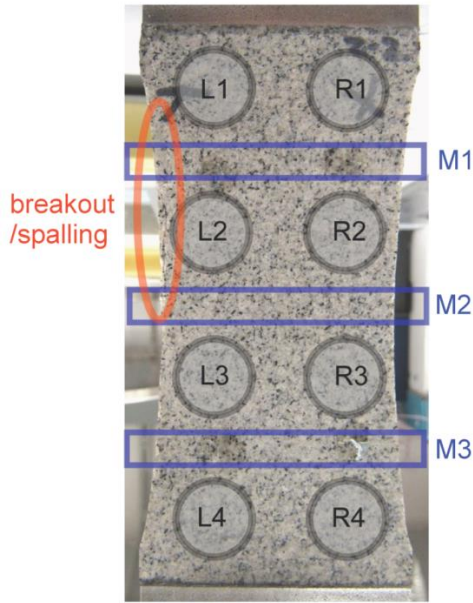


Figure 3-19. Locations of small subcores and thin section samples in Sample Z-2.

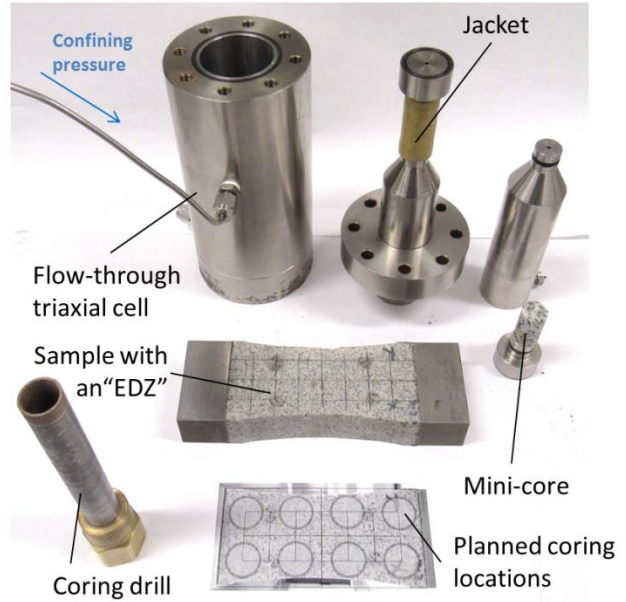
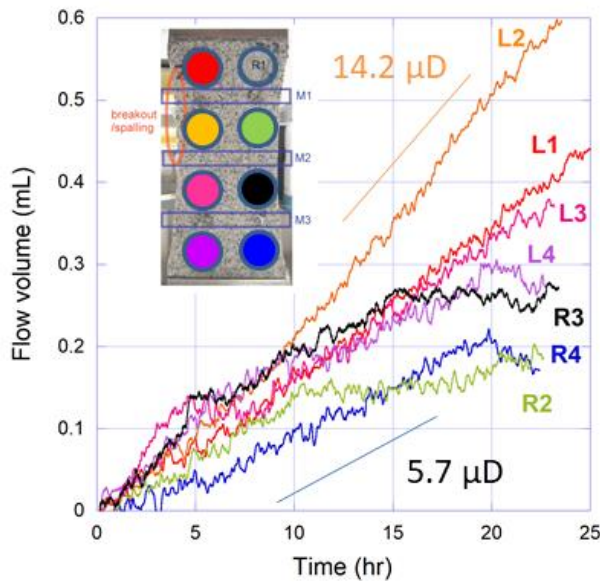
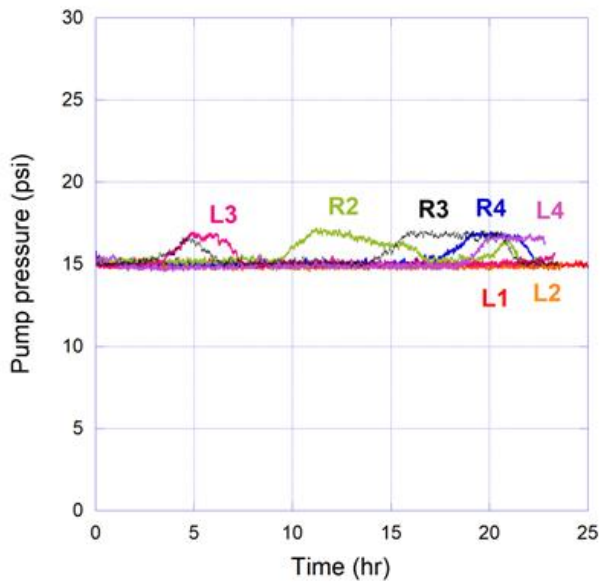


Figure 3-20. Mini triaxial test core holder used for permeability tests on the subcores.



(a.) Injected fluid volume histories



(b.) Pump pressure history

Figure 3-21. Water-injection flow permeability tests on mini cores. The overall changes in the injection rate correspond well to the expected degree of fracturing of the core samples for their locations in the moderately damaged slab Sample Z-2. Note that Sample R1 has not been tested yet.

For the locations M1, M2, and M3, indicated in Figure 3-19, thin section samples were also prepared for conducting the optical microscope study of the induced microcracks. These samples were prepared by

Burnham Petrographics LLC, ID, and the samples were impregnated with blue epoxy to mark open pores and cracks in the samples (Figure 3-22). In the photograph, approximate locations of the observed area FOV1 and FOV2 are indicated.

From the image of FOV1 in Figure 3-23, intense microfractures roughly parallel to the spalled rock surface can be seen as a network of blue, epoxy filled cracks. However, once away from the surface, no clear presence of the cracks can be seen, except for a few, sparsely distributed, randomly oriented cracks (Figure 3-23). Because the seismic velocity changes—and the flow permeability measurements—indicated strong evidence of damage induced in the interior of the sample, the scarcity of the microcracks may indicate that very small aperture of the induced microcracks prevented the intrusion of the dyed epoxy.

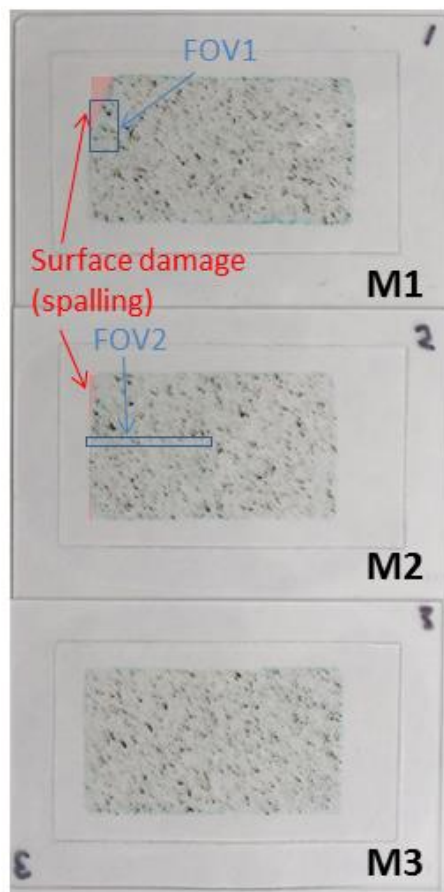


Figure 3-22. Petrographic thin section samples made for the Sections M1, M2, and M3 shown in Figure 3-19. The width of the samples is 50.8 mm, and the height 25.4 mm. Blue boxes (FOV1 and FOV2) in the figure indicate the field of view of the magnified microscope images shown in Figure 3-23.

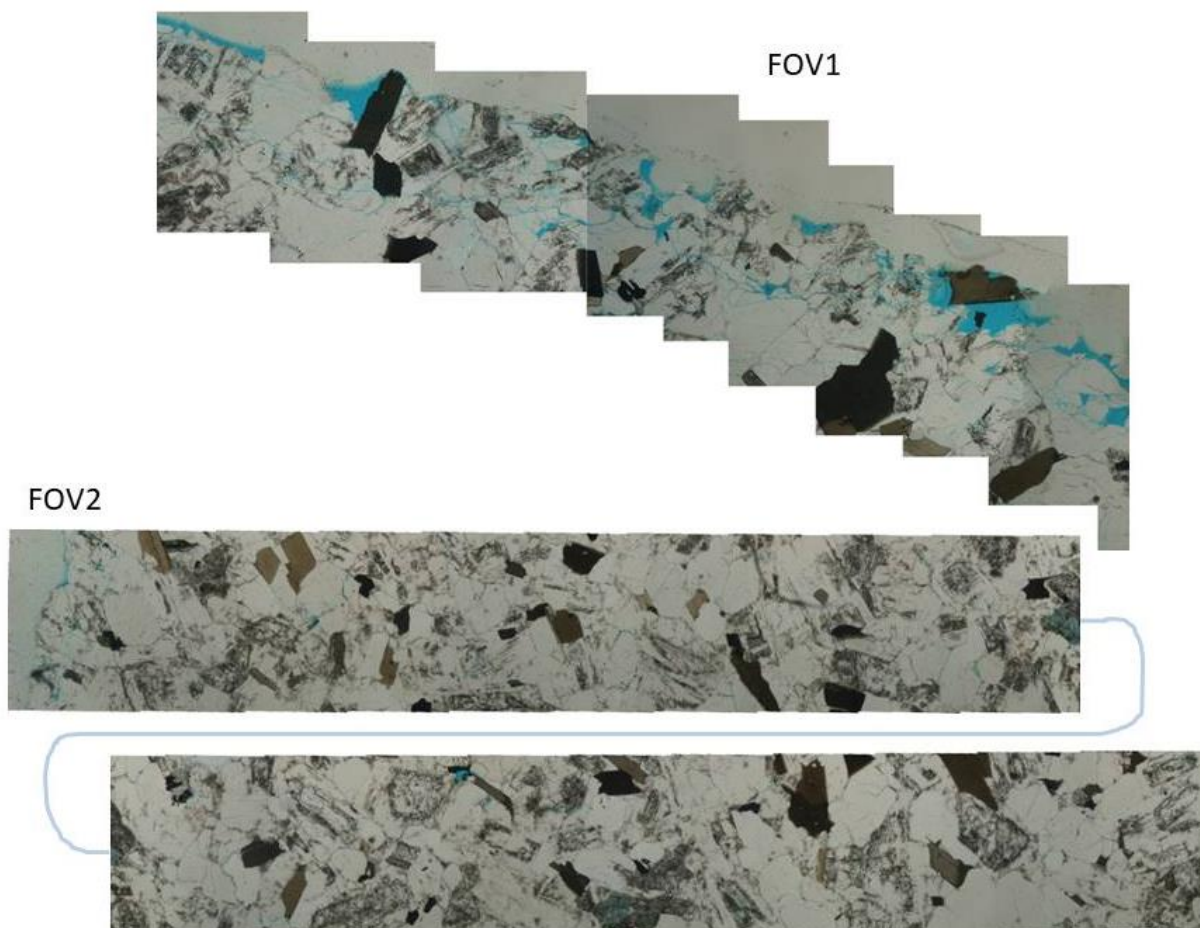


Figure 3-23. Thin-section images of FOV1 and FOV2 shown in Figure 3-22. Microcracks in the samples are mostly concentrated near the spalling observed on the surface of the sample, and much less cracks are found inside the slab samples.

3.3 Rigid Body Spring Network (RBSN) Modeling of EDZ Development

In order to help understand the development of microcracks due to the rock damage observed in the laboratory, we use a discrete, lattice-based approach for modeling the mechanical behavior of low-porosity crystalline rock mass with discontinuous features such as cracks and fractures. The Rigid-Body-Spring Network (RBSN), a kind of discrete modeling approach, represents the system behavior by simple two-node elements interconnected on a set of nodal points. The RBSN formulation is based on the concept of the Rigid-Body-Spring Model (RBSM), first introduced by Kawai (1978), in which the material constitution is represented as a collection of rigid bodies connected by spring sets. This section of the report presents a model setup for the compression test of shaped slab sample, the representation of Poisson effect in the RBSN formulation, followed by conclusions.

3.3.1 Model Setup

The RBSN model adopts the Voronoi diagram for partitioning the domain and the dual Delaunay tessellation for constructing the assembly of lattice elements. Each Voronoi cell is associated with an individual nodal point, where the kinematics of the cell is defined. The Voronoi discretization is basically carried out in three steps: nodal point generation, Delaunay tessellation, and Voronoi tessellation (Figure 3-24).

First, a set of nodal points are positioned regularly or irregularly inside the domain (Figure 3-24(a)). For random point generation, the points are sequentially generated with a minimum allowable distance l_{min} between neighboring points, which define the desired nodal density and thus controls the mesh size. Furthermore, various mesh fineness is attainable using a user-specified spatial correlation function for l_{min} . Nodal points also can be predefined at a specific position from input if necessary for the assignment of boundary geometry and other conditions.

The second step provides the Delaunay tessellation, for which a collection of tetrahedra connect the nodal points (Figure 3-24(b)). The Delaunay tessellation is constructed using the concept of a super-tetrahedron (Sloan, 1987; Taniguchi et al., 2002). The circumsphere of each tetrahedron is the smallest sphere that circumscribes the corresponding four nodal points. In general, a randomly distributed point set corresponds to a unique Delaunay tessellation, in which no two coincidental circumspheres exist. The resulting Delaunay tessellation represents the unstructured mesh of lattice elements. Each tetrahedral edge connects two adjacent nodes, by which the nodal connectivity of the lattice element is defined.

Following the Delaunay tessellation, the Voronoi tessellation is constructed with convex polyhedrons called Voronoi cells (Figure 3-24(c)). The Voronoi cell for a nodal point is a territory in which the locations are closer to the corresponding point than any other points. Locations on a cell boundary are equally close to the neighboring nodal points for which the Voronoi cells share that boundary (i.e., common cell boundary). In consequence, the domain is collectively filled with the disjoint Voronoi cells for all the nodal points. Also, the Voronoi diagram has a unique geometric correspondence with the Delaunay tessellation for a set of nodal points (Okabe et al. 2000). The geometries of the dual Delaunay-Voronoi tessellations are used for the RBSN element formulation, which will be discussed in the next subsection.

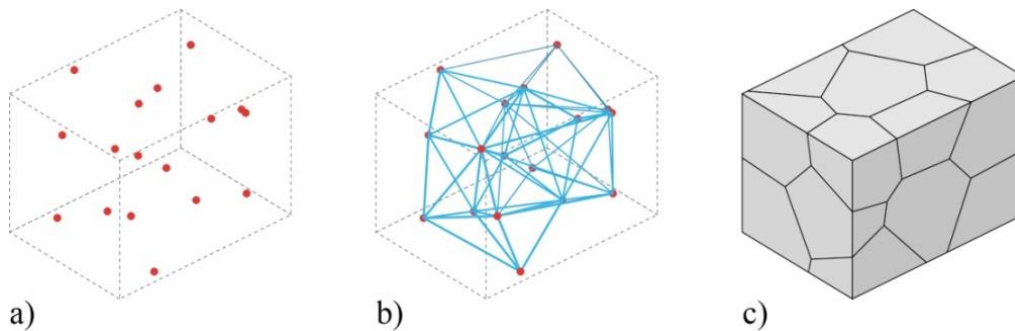


Figure 3-24. Domain partitioning process: a) nodal points; b) Delaunay, and c) Voronoi cells.

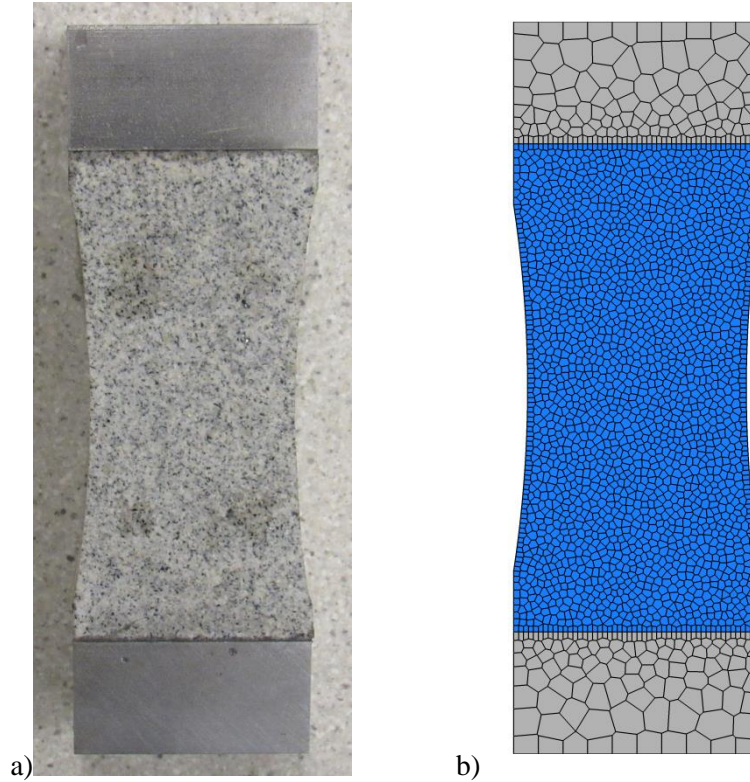


Figure 3-25. Preparation of shaped slab samples: a) for laboratory experiments; and b) for the numerical simulations.

For simulations of the shaped slab compression test, we generated a Voronoi mesh based on laboratory experiment samples. The particular geometry of the sample involved curved surfaces on the sides of a rectangular slab, with a length of 10.2 cm, a width of 5.08 cm, and a thickness of 2.54 cm (Figure 3-25(a)). The curvature on the sides has a radius of 25 cm. Also, $2.54 \times 2.54 \times 5.08$ cm steel blocks are attached at the top and bottom ends in order to prevent tensile fracturing of the sample. The resulting mesh, shown in Figure 3-25(b), replicates all the geometric features of the laboratory sample.

3.3.2 Implementation of Arbitrary Poisson's Ratio

3.3.2.1 RBSN MODEL FORMULATION

A lattice element consists of a spring set and rigid-body constraints connecting neighboring nodes. Figure 3-26 presents the formation of a lattice element for arbitrary neighboring nodes i and j . A zero-size spring set is located at position C (the centroid of the common Voronoi cell boundary), and rigid arms from the spring set link the neighboring nodes (Figure 3-26(b)). Each node has six degrees of freedom (three translations and three rotations) for the case of 3D modeling, and the spring set is also formed from three axial springs and three rotational springs as shown in Figure 3-26(c).

The Voronoi cell is basically considered to be rigid in the sense that it maintains its original shape during the process of loading and material deformation (assumption of small strain). The flexibility of the motion is lumped into the spring sets; therefore, the separation and interpenetration of the cells are permitted. The rigid-body constraints link the nodal degrees of freedom to the generalized relative displacements of the spring set. The spring set consists of three axial springs and three rotational springs acting independently, with stiffnesses $\mathbf{D} = \text{diag}[k_n, k_s, k_t, k_{\phi n}, k_{\phi s}, k_{\phi t}]$ in local n - s - t coordinates. The spring coefficients are scaled in proportion to the distance between the element length h_{ij} , and the area of the Voronoi cell boundary A_{ij} :

$$k_s = k_t = \alpha_1 k_n = \alpha_1 \alpha_2 E \frac{A_{ij}}{h_{ij}}, \quad k_{\phi n} = E \frac{J_p}{h_{ij}}, \quad k_{\phi s} = E \frac{I_{ss}}{h_{ij}}, \quad k_{\phi t} = E \frac{I_{tt}}{h_{ij}} \quad (3.2)$$

in which E is the elastic modulus, J_p , I_{ss} , and I_{tt} are the polar and two principal moments of inertia of the Voronoi cell boundary with respect to the centroid, respectively. By adjusting α_1 and α_2 , according to experimental results, macroscopic modeling of both elastic constants (E and Poisson's ratio, ν) is possible. However, a local description of Poisson effect is not realized with $\alpha_1 \neq 1$. For the special case of $\alpha_1 = \alpha_2 = 1$, the Voronoi scaling of the spring coefficients enables the model to be elastically homogeneous under uniform modes of straining, albeit with zero effective Poisson's ratio (Bolander and Saito, 1998).

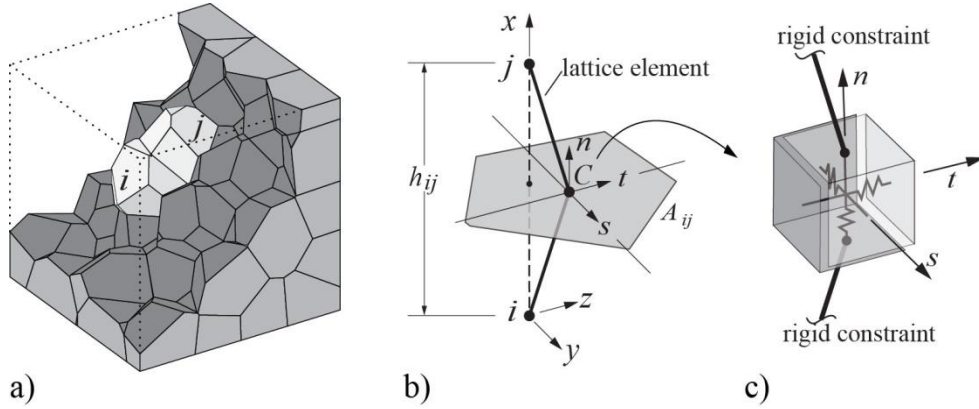


Figure 3-26. Typical RBSN lattice element ij : a) neighboring nodes i and j in a Voronoi diagram; b) isolated from the network; and c) a zero-size spring set located at centroid C of Voronoi cell boundary area A_{ij} (rotational springs have been omitted for clarity).

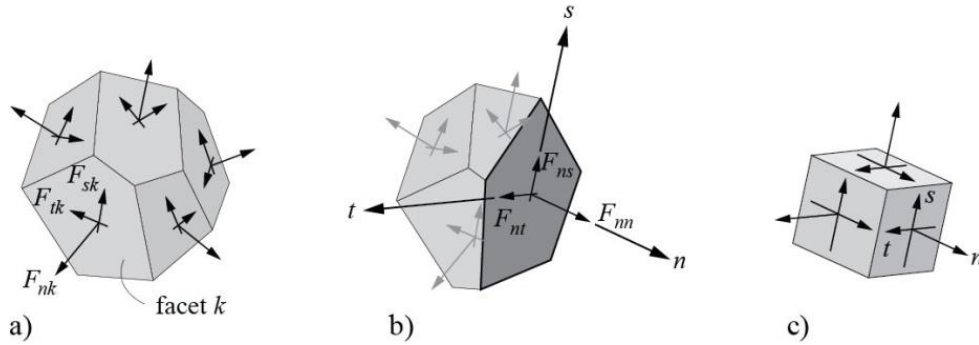


Figure 3-27. Stress tensor at a Voronoi cell node: (a) components of spring force local coordinates; (b) a set of nodal forces satisfying the equilibrium; and (c) complete stress tensor at Voronoi cell node (Adapted from Yip et al., 2005).

At each loading step, stress values are derived from the calculated spring forces. Since a lattice element is structured as a lineal connection with a determined local coordinates, the stress state is available only in the form of a vector by averaging the axial spring forces F_n , F_s , and F_t over the cell boundary area A_{ij} (see Figures 3-26(b,c)). In order to expand the stress state to a tensor form, equilibrium conditions are considered at each Voronoi cell node. Sets of the spring forces are applied at the boundaries surrounding a Voronoi cell (Figure 3-27(a)), and nodal force components F_{nn} , F_{ns} , and F_{nt} can be calculated for an arbitrary section passing through the Voronoi cell node with its corresponding local n - s - t coordinates, which satisfy the equilibrium condition with all the forces acting on the remained cell boundaries (Figure 3-27(b)). Moment contributions to equilibrium are not considered here. By dividing these force components by the cut-face area, the corresponding stress components σ_{nn} , σ_{ns} , and σ_{nt} can be obtained.

By repeating this process for three mutually perpendicular sections, the full stress tensor is obtained (Figure 3-27(c)). Details are given elsewhere (Yip et al., 2005).

3.3.2.2 Fictitious Stress Approach

As described in the previous subsection, macroscopic modeling of Poisson's ratio by adjusting α_1 and α_2 in Equation (3.2) leads an irrational stress production at the local level of stress representation of lattice elements, so called the artificial heterogeneity (Bolander and Saito, 1998). To avoid that unrealistic modeling results, the fictitious (or auxiliary) stress approach has been implemented for representation of the Poisson effect. The formulation is presented as a series of steps.

Step 1: Nodal displacements are determined for the prescribed boundary conditions by solving the system equations for the case of $\alpha_1 = \alpha_2 = 1$ in Equation (3.2), which corresponds to $\nu = 0$. This condition provides an elastically homogeneous basis for introducing the Poisson effect. Principal stresses, σ_1 , σ_2 , and σ_3 , and principal strains, ε_1 , ε_2 , and ε_3 , are calculated at each node using the method for nodal stress calculation given in Section 3.3.2.1. The indices 1, 2, and 3 denote the maximum, intermediate, and minimum principal values, respectively.

Step 2: At each node, an auxiliary measure of orthogonal strain is determined using the vector form of the principal strains, $\boldsymbol{\varepsilon}_p = [\varepsilon_1 \ \varepsilon_2 \ \varepsilon_3]^T$, and actual non-zero value of ν

$$\boldsymbol{\varepsilon}' = \nu \hat{\mathbf{I}} \boldsymbol{\varepsilon}_p \quad (3.3)$$

in which

$$\hat{\mathbf{I}} = \begin{bmatrix} 0 & 1 & 1 \\ 1 & 0 & 1 \\ 1 & 1 & 0 \end{bmatrix}. \quad (3.4)$$

The fictitious stress is obtained by multiplying both sides of Equation (3.3) by E

$$\boldsymbol{\sigma}' = E \nu \hat{\mathbf{I}} \boldsymbol{\varepsilon}_p = \nu \hat{\mathbf{I}} \boldsymbol{\sigma}_p \quad (3.5)$$

where $\boldsymbol{\sigma}_p = [\sigma_1 \ \sigma_2 \ \sigma_3]^T$.

Step 3: Fictitious stress is introduced into the lattice elements framing into each node i via a set of tractions, which are applied to the facets of the associated Voronoi polyhedral cell (Figure 3-28). For facet m , the traction vector is expressed by

$$\mathbf{t}_m^i = \mathbf{S}^i \mathbf{n}_m^i \quad (3.6)$$

where $\mathbf{S}^i = \text{diag}(\sigma_1', \sigma_2', \sigma_3')$ for node i , and \mathbf{n}_m^i is the outward unit normal vector of facet m from node i . To facilitate explanation, but without loss of generality, the coordinate and principal directions in Figure 3-28 are assumed to be aligned. The auxiliary force acting on facet m is then

$$\mathbf{f}_m^i = \mathbf{t}_m^i A_m \quad (3.7)$$

where A_m is the area of facet m . This auxiliary force, resolved into normal and tangential components, is introduced into the spring set of the rigid-body-spring element associated with the facet. The set of auxiliary forces acting on the cell facets is in equilibrium.

Step 4: The introduction of auxiliary spring forces produces nodal displacements, in accordance with the prescribed boundary conditions of Step 1. The new principal stresses, $\hat{\boldsymbol{\sigma}}_p = [\hat{\sigma}_1 \ \hat{\sigma}_2 \ \hat{\sigma}_3]^T$, are calculated at each nodal site.

Step 5: Convergence of the algorithm is achieved when $\|\hat{\sigma}_p - \sigma_p\| < e$, where $\|\cdot\|$ is the Euclidean norm with respect to all nodal values and e is a predefined tolerance. Otherwise, the procedure returns to Step 2 with updated $\sigma_p = \hat{\sigma}_p$. Convergence is ensured since the fictitious stresses of Equation (3.5) become progressively smaller for the normal range of ν .

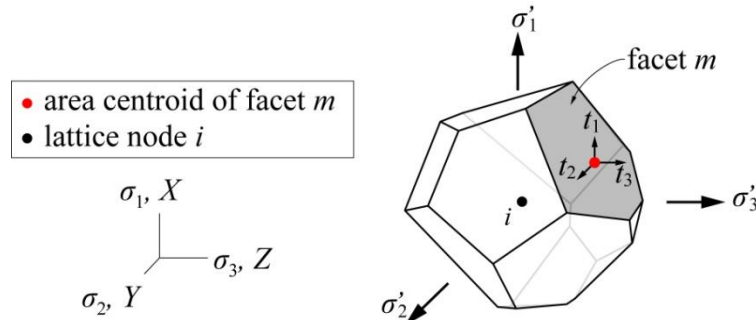


Figure 3-28. Fictitious stresses and associated traction vectors for facet m of Voronoi cell i (adopted from Asahina et al., 2017).

3.4 Conclusions and Future Plans

This objective of this task is to investigate a possibility of the development of excavation-induced damage zone around circular openings (i.e., boreholes and tunnels) in crystalline rock and their impact on rock's mechanical and hydrological properties. To address the issue of scale effects imposed by laboratory testing of small analogue boreholes and tunnels, rock samples with a special geometry (i.e., shaped samples with curved surfaces) have been used to induce realistic breakout on the sample surface and to evaluate a possibility of damage away from the sample surface. The use of such samples allowed us to (1) induce surface breakout, which is expected to occur in the EDZ in strong granite, (2) conduct real-time optical visualization of the EDZ development, and (3) perform acoustic visualization of microcracking in the samples via AE event location.

The acoustic measurements, both AE location and post-mortem seismic velocity measurements, indicated the development of microcracks away from the rock surface, where surface damage was observed. These observations are consistent with the results of measurements of permeability of the cores collected from the tested rock sample. However, visual inspection of the sample or examination of thin sections under a microscope did not indicate the presence of the microcracks clearly. Also, as a surface breakout grows and the failure occurs away from the curved surface, the difference between the laboratory sample and a field tunnel or a borehole grows. However, this test method can be improved to provide a tool for investigating the impact of relatively shallow breakouts on the mechanical and hydrological behavior of excavation-induced damage. Additionally, the laboratory tests can be designed to provide useful calibration data for numerical models for further upscaling.

In the newly started numerical modeling effort, we have implemented the fictitious stress approach to represent the Poisson effect without any spurious stress calculation in the lattice elements. Due to the two-node element representation of the displacement field, ordinary lattice models do not properly simulate local stress conditions for general elastic media (i.e., for arbitrary choices of E and ν). The approach described herein remedies the inabilities of regular lattice models to calculate local measures of stress. Based on tensorial representations of stress at each node, a set of fictitious forces are calculated and introduced into the lattice in a manner that correctly produces the Poisson effect. In consequence, the stiffnesses of the lattice elements are defined by the elastic constants (E and ν) without any calibration against laboratory test results. Also, we have conducted a model preparation for simulations of the shaped slab compression test. A Voronoi mesh is generated based on the geometry of laboratory test samples,

which fully renders the geometric features, such as curved side cuts and steel loading blocks, in the real specimen.

For future work, we plan to test different types of rocks—including noncrystalline rocks, such as shales and carbonates—to understand the impact of rock texture and grain size on the hydrological and mechanical processes expected to occur in the EDZ. Also, we plan to test rock samples from field laboratories, including granite samples from the Grimsel and Stripa mines. Further, the hydro-mechanical-chemical interaction between the filling materials within the excavation and the EDZ is to be investigated. Concurrently, we plan to simulate the laboratory-observed EDZ development using the RBSN model, and predict the development of an EDZ in the field and its hydro-mechanical properties. A series of new modeling simulations is necessary because of nonlinear changes in the stiffness and permeability of the system resulting from progressive development of microcracks and fractures in crystalline rock.

This page intentionally left blank.

4. HYDRAULIC PROPERTIES OF FRACTURED CRYSTALLINE ROCK CORES

4.1 Introduction

This section summarizes the main activities on the hydraulic characterization of fractured core samples, which were conducted at LBNL during FY18. Transmissivity of core samples were measured under laboratory conditions of controlled stress typical for field conditions. Previous reports focused on measurement technique and comparison to field results. We also analyzed the results of the evaluation of core sample transmissivity determined in FY17. Preliminary analysis of anisotropy using data collected in FY17 provided a suggestion of anisotropy, but indicated that further laboratory experiments were necessary, motivating the FY18 work. For FY18 the effort was spent on understanding anisotropy of the fractures, because flow in fractured crystalline rock in the deep subsurface takes place through a fracture network, and is dependent on fracture aperture distribution and the hydraulic head field. The main thrust of the core measurements at LBNL is to determine fracture transmissivity as a function of controlled stress under laboratory conditions. Cores were taken from the borehole COSC-1 (Collisional Orogeny in the Scandinavian Caledonides – COSC – See Chapter 5). The measurements were conducted under controlled stress conditions with fluid delivery and collection customized to directly investigate the effect of stress on fracture hydrologic behavior. A unique apparatus, described in Section 4.2.3, was constructed to enable flow through four flow channels on the fracture face, to measure multi-directional transmissivity, to assess fracture anisotropy.

4.2 Methodology

4.2.1 Description of Fractures

Four fractured core samples were chosen for the anisotropy and transmissivity measurements, and can be seen in the top four frames of Figure 4-1. Criteria for fracture selection were (1) having the correct diameter for the experimental apparatus (60 mm diameter), and (2) having a clean fracture that could be sealed on the core sides. All the cores were inspected, photographed, measured, and evaluated for usability in the experiment. All cores appear to be very tight crystalline rock, containing at least one cross-cutting fracture, and some with secondary mineralization near the fractures. Two fractured cores were selected for more detailed measurements, 211-2 and 401-1, for having the best fit to the system and the least amount of damage.

In addition to the naturally fractured cores, two artificial fractured cores were constructed and used to check the system. Several methods of artificial fracture construction were evaluated, including the use of epoxy, epoxy and sand mixtures, and other moldable compounds. It was determined that Delrin cores were the most reliable, and they were used for the experiments. One artificial core was a 60 mm diameter x 85 mm length cylinder with a horizontal hole drilled through the center. This design effectively blocks three of the flow channels and allows flow through the fourth, mainly to evaluate whether the sleeve surrounding the core properly blocks circumferential flow paths. The other artificial core had the same dimensions but was sliced in half, and an aperture distribution was created by creating a roughness on one half, as shown in the lower two frames of Figure 4-1.

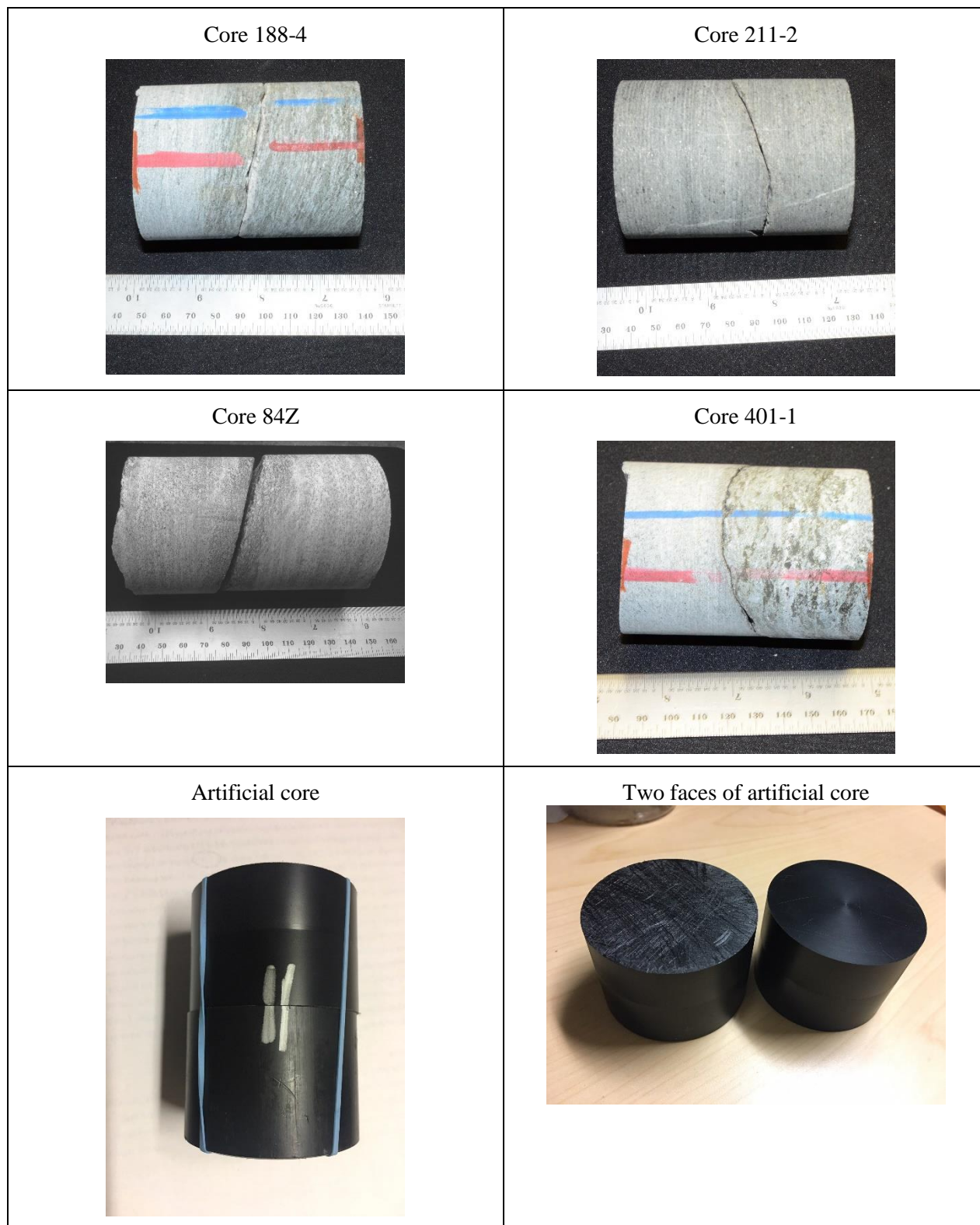


Figure 4-1. Photographs of natural and artificial cores used in this study.

4.2.2 Aperture Measurements

The fractured cores were CT scanned using a modified GE Lightspeed medical X-ray CT scanner before and after transmissivity measurements were made, to get a better understanding of fracture geometry and to estimate the aperture distribution. Because the cores had to be removed from the pressure vessel for scanning, scans were performed without applying the confining pressure. Figures 4-2(a) and (b) show the apertures and CT cross sections of cores 211-2 and 401-1. Figure 4-3 is an image of the sample on the table ready for CT scanning.

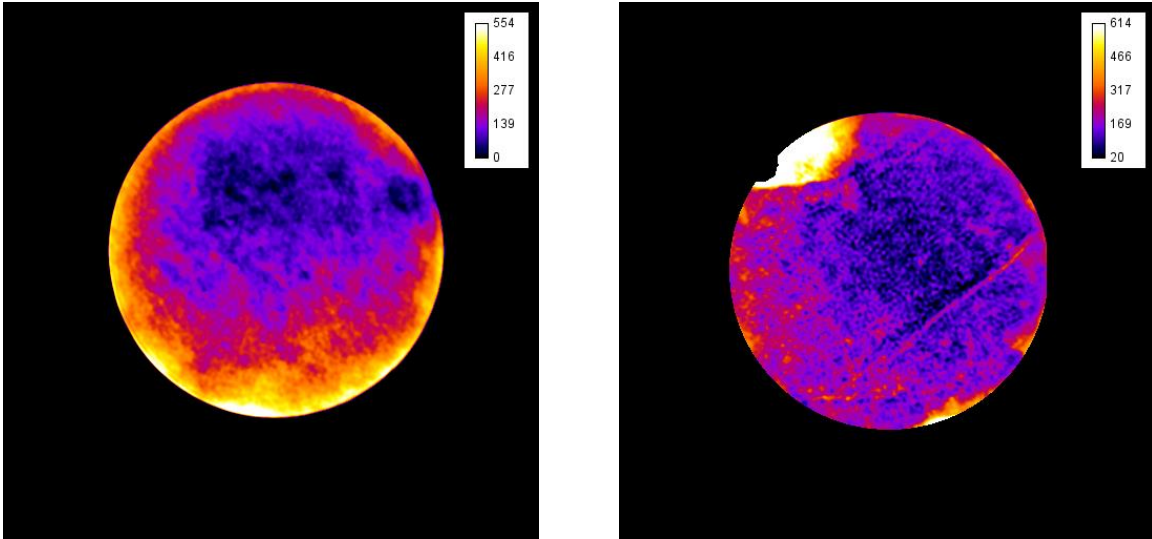


Figure 4-2(a.) Aperture maps from CT measurements for cores 211-2 (left) and 401-1 (right). Calibration scale in μm . Scans were taken on the cores with no confining pressure applied before the transmissivity measurements were made.

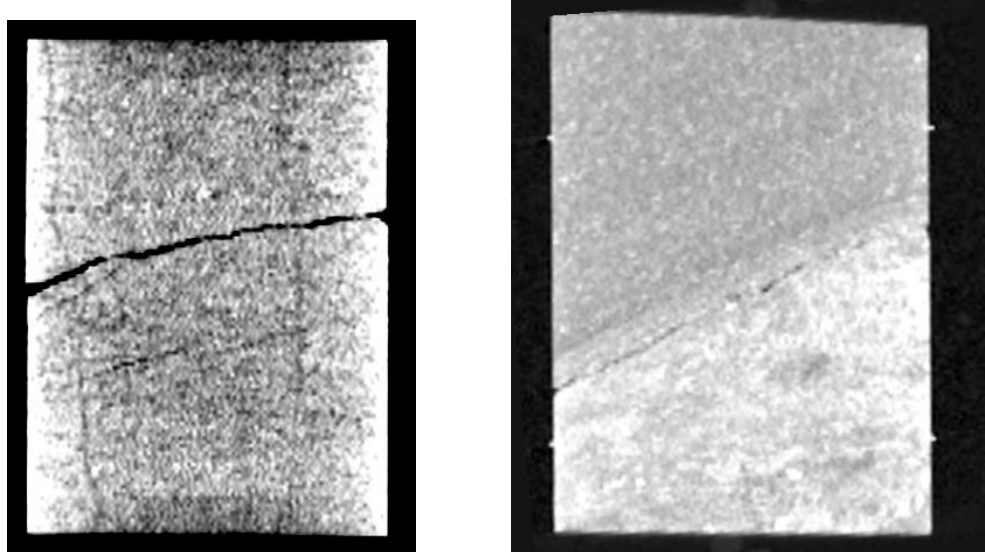


Figure 4-2(b.) Cross sections of Cores 211-2 (left) and 401-1 (right).



Figure 4-3. Sample on CT table ready for scanning.

In addition to the CT scanning method, a surface scan was performed using a surface profiling microscope (Keyence, Itasca, IL), and the surfaces were aligned and subtracted to estimate the aperture (Figure 4-4). The surface scans were high quality, but work is ongoing to align the faces to get the aperture maps to agree between the two measurement methods. At this time, this method is giving larger aperture values than the CT scanning method and more effort is needed to reconcile the two methods.

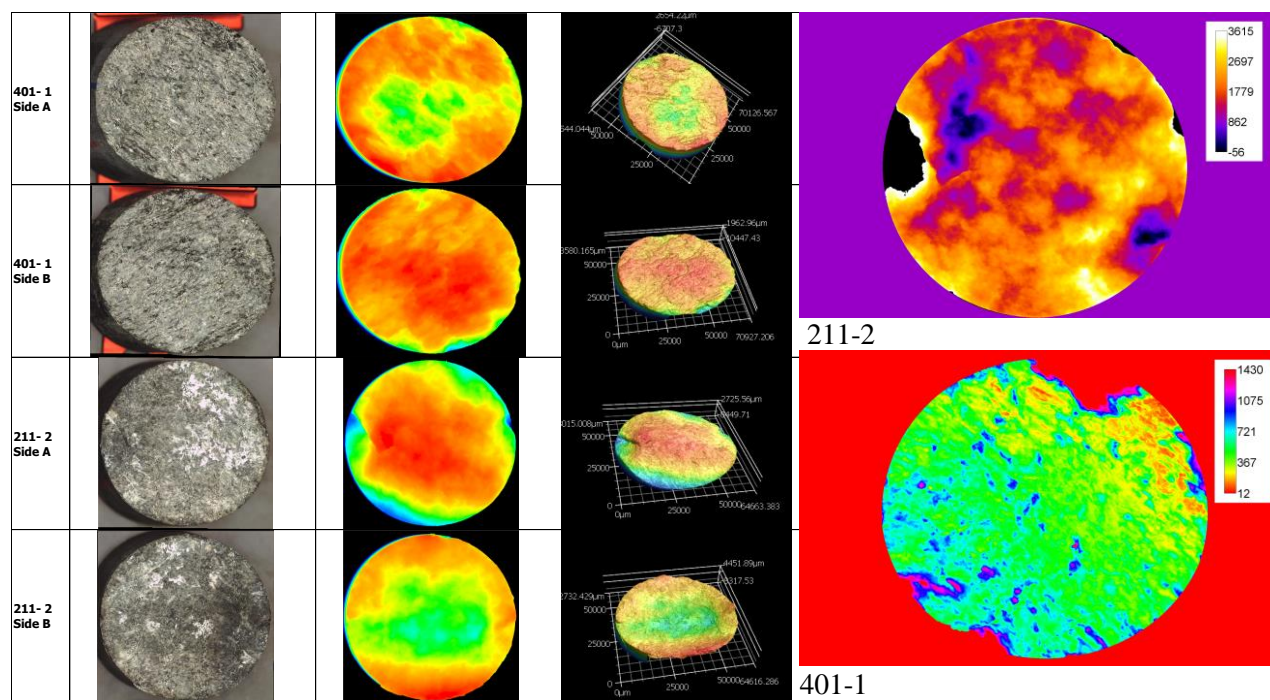


Figure 4-4. Surface profile measurements from the Keyence scanning for Cores 401-1 and 211-2. On the left is the data from the scanning scope (core photos, plan views of digital scans, perspective 3D views of scans), and on the right are estimates of the aperture after aligning and subtracting the surface maps.

4.2.3 Experimental Apparatus

The transmissivities were measured over a range of effective stresses from 200 to 1,100 psi. For the measurements, a custom apparatus was constructed allowing for delivery of water to any of four inlets distributed at 45-degree increments around the circumference of the core, and to extract water from an outlet opposite to the inlet (Figures 4-5 and 4-6). The inlets and outlets are half-tubes running along the

length of the core to insure the contact with the fracture. A custom silicone rubber sleeve (Figure 4-6) was manufactured to fit around the core and inlet and outlet tubes to inhibit flow around the core. This sleeve was cast with silicone molding compound over a mockup of the setup to provide the proper fit.

The top inlet and outlet support is a solid Delrin (a hard plastic) hockey-puck shaped disk with holes to hold the inlet and outlet tubes on one side, and national pipe thread (NPT) fittings on the other. One-quarter inch stainless steel tubes were connected to the NPT fittings, and these were run through feed-through ports on the pressure vessel cap (Figure 4-6). Outside the pressure vessel, each tube was connected to a 20 psi pressure relief valve, and then to a five-way ball valve. Inside the pressure vessel, the tubes were connected to half round tubing that ran along the outside of the core. The ends of the half round tubing were plugged with the same silicone molding compound used for the sleeve.

A second solid hockey puck-shaped Delrin disk was placed at the bottom of the core and sleeve, and a thin Latex sleeve followed by a Viton sleeve was placed over the entire assembly to prevent leaks into the assembly from the confining fluid. The assembly shown in Figures 4-5 and 4-6 was placed in a pressure vessel (High Pressure Equipment Company TOC-31-20) with an inside diameter of 4 inches, an inside length of 20 inches and a rating of 5,000 psi. A high-pressure precision syringe pump (Isco D-series) connected to a pressure port on the bottom of the pressure vessel was used to provide controlled confining pressure.

The sleeve system surrounding the core was designed to fit tightly around the core and half round stainless tubing, to prevent circumferential flow and to guide the fluid into the fracture. Modifications were made to the silicone sleeve in FY18, mainly removing the silicone end that interfaced between the bottom Delrin puck and the rock. This was done to insure that the confining pressure was directly applied to the core, and did not cause bowing out of the sleeve. In addition, previously a strip of copper was placed around the core under the silicone sleeve to help support the silicone sleeve and to keep the silicone from deforming into the fracture when confining pressure was applied. However, this year the copper strip was removed as the lower confining pressures used (1,100 psi max v. 4,500 psi max in previous years) did not require this extra stiffness. Also, at the lower confining pressures, the advantage of better sealing on the core surface with the silicone sleeve outweighed the benefits of the copper strip. Water penetration or adsorption into the matrix is not a factor in this experiment because the rocks are tight crystalline rock and flow occurs for such a short period of time.

At the top of the cores, at the interface between the upper Delrin disk with the feed-through flow tubing and the rock surface, a non-deformable gasket was placed to prevent flow through the top of the sample.

Flow through the fracture was driven using another precision high-pressure syringe pump (Isco D-series), although flow pressures were kept below 20 psi. Initially a model 1000D pump was used for the flow, but measurement of the transmissivity for the 401-1 required lower flow rates so this was exchanged for the model 500D pump. Flow was regulated through two 5-way ball valves (1 inlet tube and 4 outlets), and the pressure difference between the inlet and outlet was measured using a Rosemount 3051 differential pressure transducer and the signal recorded with a Keithley 2701 digital multimeter using Excelinx software.

To test the apparatus, a Delrin core of the same size as the rock cores was manufactured, which was solid except for one horizontal hole 1/16" in diameter through the core center. This dummy core was placed in the system and tested with the same range of confining pressure used for the natural cores. For the channel aligned with the through-hole, very low to no differential pressure was observed indicating that flow was not restricted. For the other three paths, no flow was observed and the differential pressure steadily climbed until nearing the pressure limit of the flow system (20 psi), indicating that no flow was occurring.

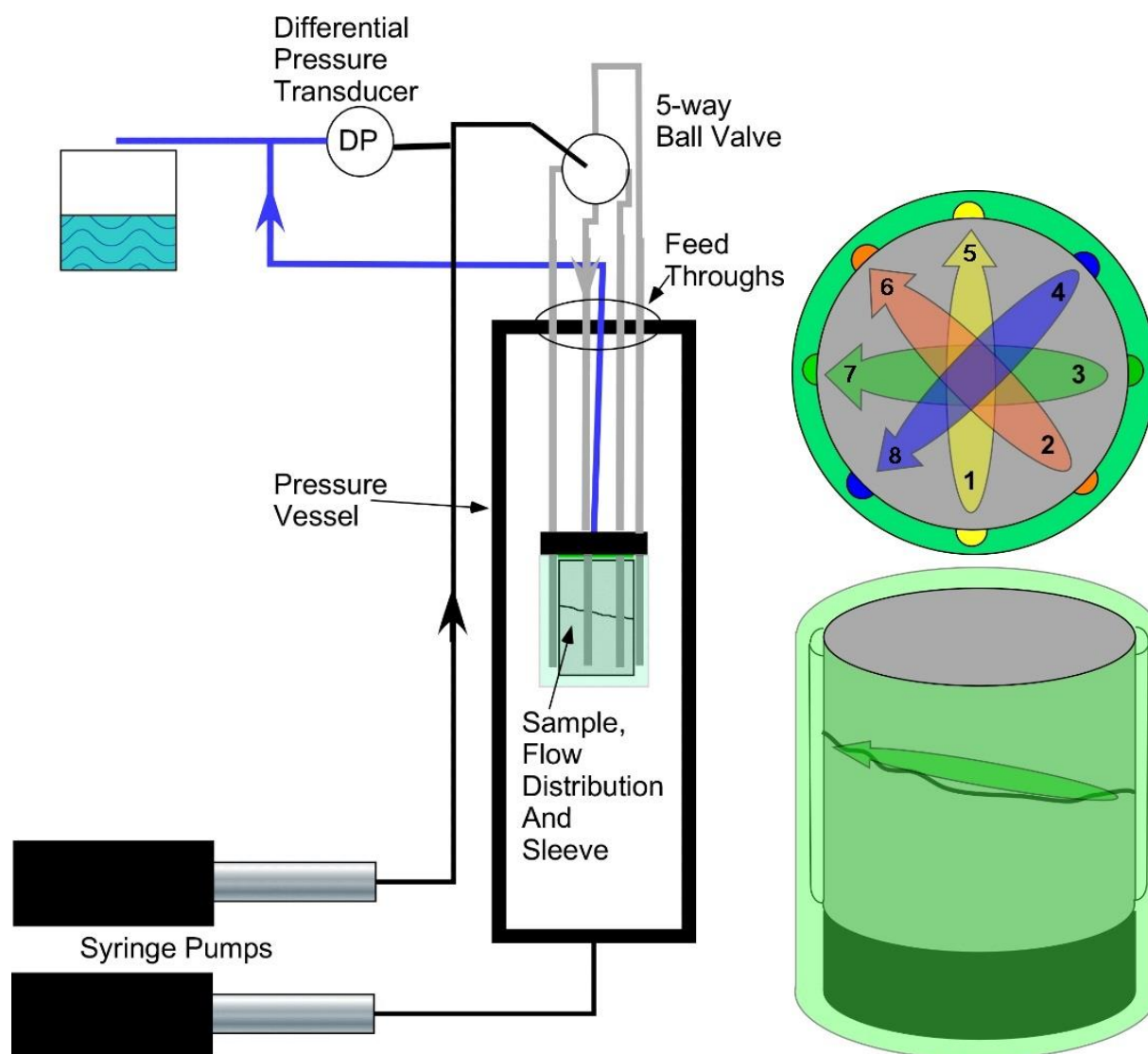


Figure 4-5. System schematic: The lower syringe pump controls confining pressure, and the upper syringe pump flows water through the core. Two 5-way ball valves (one shown) control flow to the inlet tubes (1-4) and outlet tubes (5-8).

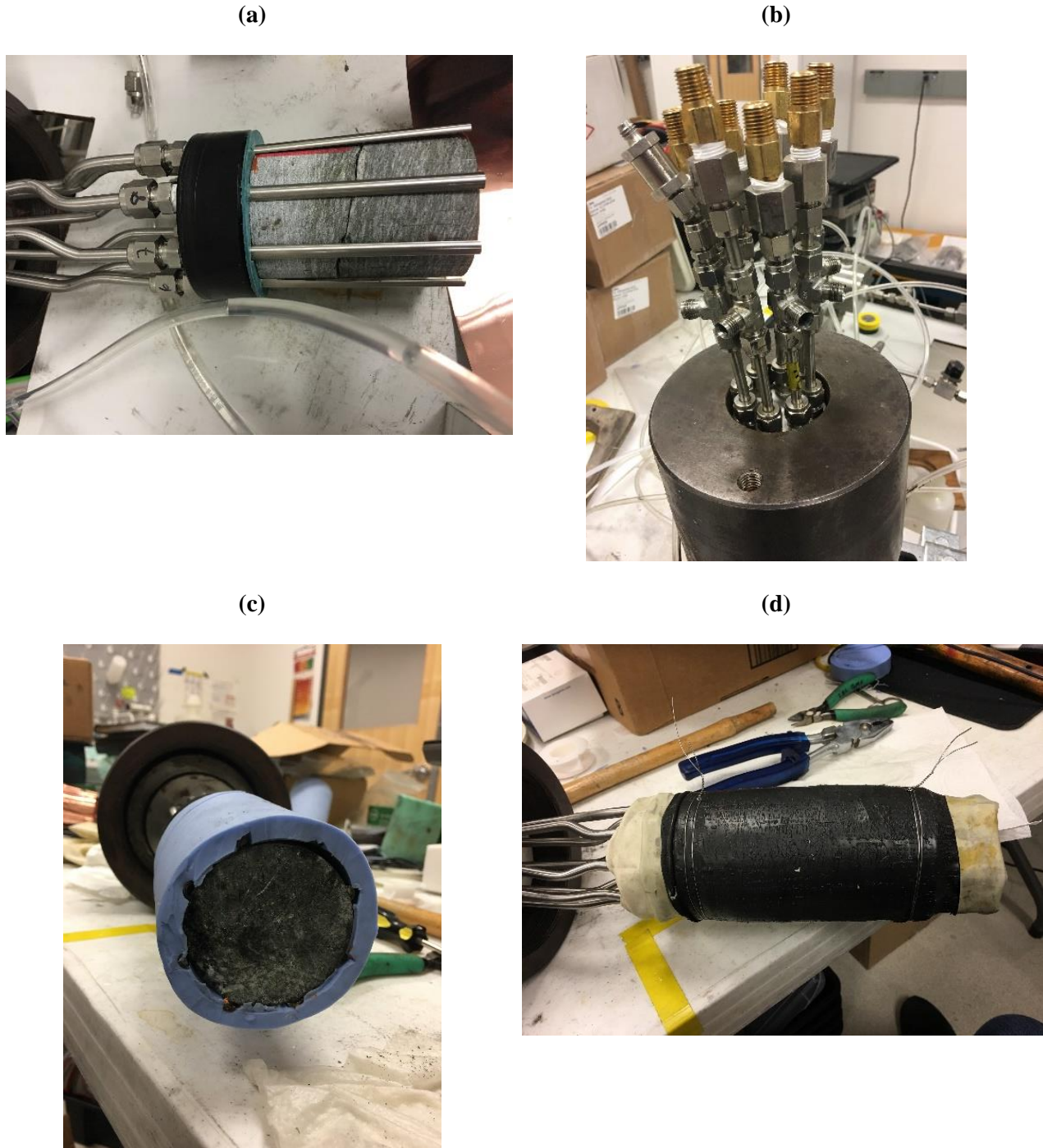


Figure 4-6. Apparatus assembly: (a) Both pieces of the fractured core are placed in between the water inlets and outlets, (b) feed-through ports on the pressure vessel cap, (c) end of core showing the Silicone rubber sleeve, and (d) view with outer sleeve in place.

4.2.4 Experimental Procedure

After preparing the core as described above, the core sample was placed in the pressure vessel. The vessel was filled with water and 100 psi confining pressure was applied to the core. Air bubbles in the tubing cause noise in the data and artificially increase the measured differential pressure, so any air bubbles in the flow tubing must be removed. This is an important step that cannot be omitted, even though it can be time-consuming.

Because previous experimental results showed that when confining pressure was increased for the first time, transmissivity decreased sharply and did not recover when the confining pressure was subsequently decreased, a procedure was developed to settle the fracture before beginning transmissivity measurements. After initial bubble removal, confining pressure was increased stepwise to 1100 psi, then reduced to 600 psi, and cycled two more times. After settling, differential pressure measurements were made across each of the four pathways (1-5, 2-6, 3-7, and 4-8, as shown in Figure 4-5) for at least three different flow rates. The flow rates ranged from 0.01 to 10 mL/min depending on the transmissivity of the core. When the flow measurements were completed, another confining pressure cycle was done and the measurements were repeated to assure a repeatable data set was produced. After data were collected for the flow directions (1-5, 2-6, 3-7, and 4-8), the flow directions were reversed and the measurements were repeated for directions 5-1, 6-2, 7-3, and 8-4.

4.2.5 Transmissivity Calculations

Differential pressure and flow rate measurements were completed on cross-cutting fractures through two core samples - Cores 211-2 and 401-1.

In the case of a planar rectangular fracture with fluid inlet and outlet occurring uniformly through opposite edges, shown in Figure 4-7 (top), fracture transmissivity T (m^2/s) can be calculated from the following relationship

$$T = \frac{Q\rho gl}{h\Delta P} \quad (4.1)$$

where Q = volumetric flow rate, ρ = fluid density, g = gravity, l = fracture length, h = fracture width, and ΔP = differential pressure across the fracture.

In the case of the core geometry used in our experiments, shown in Figure 4-7 (bottom), water is applied over a finite length on opposite sides of a natural fracture, having an approximately circular area. For this core geometry we modified Equation (1), based on an analogy with the solution to a similar electrical resistance problem across a disk with finite sized electrodes (McDonald, 2000).

For the rectangular case (Figure 4-7 top), the resistance R_s across the volume is

$$R_s = \frac{1}{\sigma th} \quad (4.2)$$

and, therefore, the conductance C_s is the reciprocal

$$C_s = \frac{\sigma th}{l} \quad (4.3)$$

where σ = conductivity, t = thickness, h = height, and l = length.

For the circular case (Figure 4-7 bottom), the resistance R_c is given by

$$R_c = \frac{2}{\pi\sigma t} \ln \frac{2D}{d} \quad (4.4)$$

and the conductance is

$$C_c = \frac{\pi \sigma t}{2 \ln \frac{2D}{d}} \quad (4.5)$$

where d is the inlet/outlet length, and D is the fracture diameter. Letting $l = h$ and dividing Equation (5) by Equation (3) yields

$$\frac{C_c}{C_s} = \frac{\pi}{2 \ln \frac{2D}{d}} \quad (4.6)$$

which will be used as a factor to account for the geometric difference between the circular and rectangular geometry for all cores and paths. Therefore, Equation (4.1) is modified to

$$T = \frac{C_c Q \rho g}{C_s \Delta P} \quad (4.7)$$

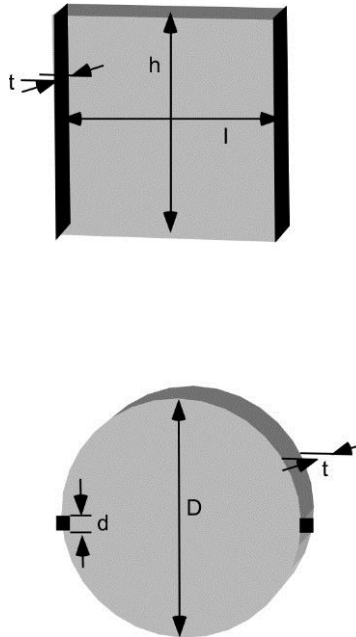


Figure 4-7. Schematic diagram of fractured core geometry used for calculations.

4.3 Laboratory results

For FY18 the effort was spent on understanding anisotropy of the fractures. Preliminary analysis of anisotropy using data collected in FY17 is presented first, followed by results from FY18 work.

4.3.1 Anisotropy Analysis of FY17 Experiments

Core 211-2. When all data is plotted for Core 211-2 (Figure 4-8), it is hard to see anisotropy, but individual cycles of pressure increase or decrease (Figures 4-9) consistently show anisotropy, with Paths 4-8 and 3-7 showing higher transmissivity than Paths 1-5 and 2-6. For the various cycles, anisotropy ranges from 1.7 to 2.7, with an average value of 2.2.

Core 401-1. A subset of the data collected at core 401-1, covering one cycle of confining pressure increase and decrease, is shown in Figure 4-10. Anisotropy is apparent, with Path 1-5 and Path 2-6 consistently showing greater transmissivity than Path 3-7. In this experiment, there was no flow through Path 4-8. For this core, the transmissivity values obtained in the laboratory are in the same range as the transmissivity estimated from flowing fluid electrical conductivity (FFEC) logging in the field (Doughty et al., 2017). The transmissivity variation with confining pressure (decreasing as confining pressure increases - top frame, then remaining constant as confining pressure decreases – bottom frame) is typical of the FY17 experiments conducted without the fracture-settling procedure. The anisotropy is similar for all confining pressures, with the ratio of transmissivity of the high-T paths (1-5 and 2-5) to the transmissivity of the low-T path (3-7) ranging from 2.0 to 2.9. If we include the zero permeability of Path 4-8, then the anisotropy would double, becoming 4.0 to 5.8.

The results of the core analyses can be summarized in Figure 4-11, which shows schematically the high flow and low flow directions for Cores 401-1 and 211-2.

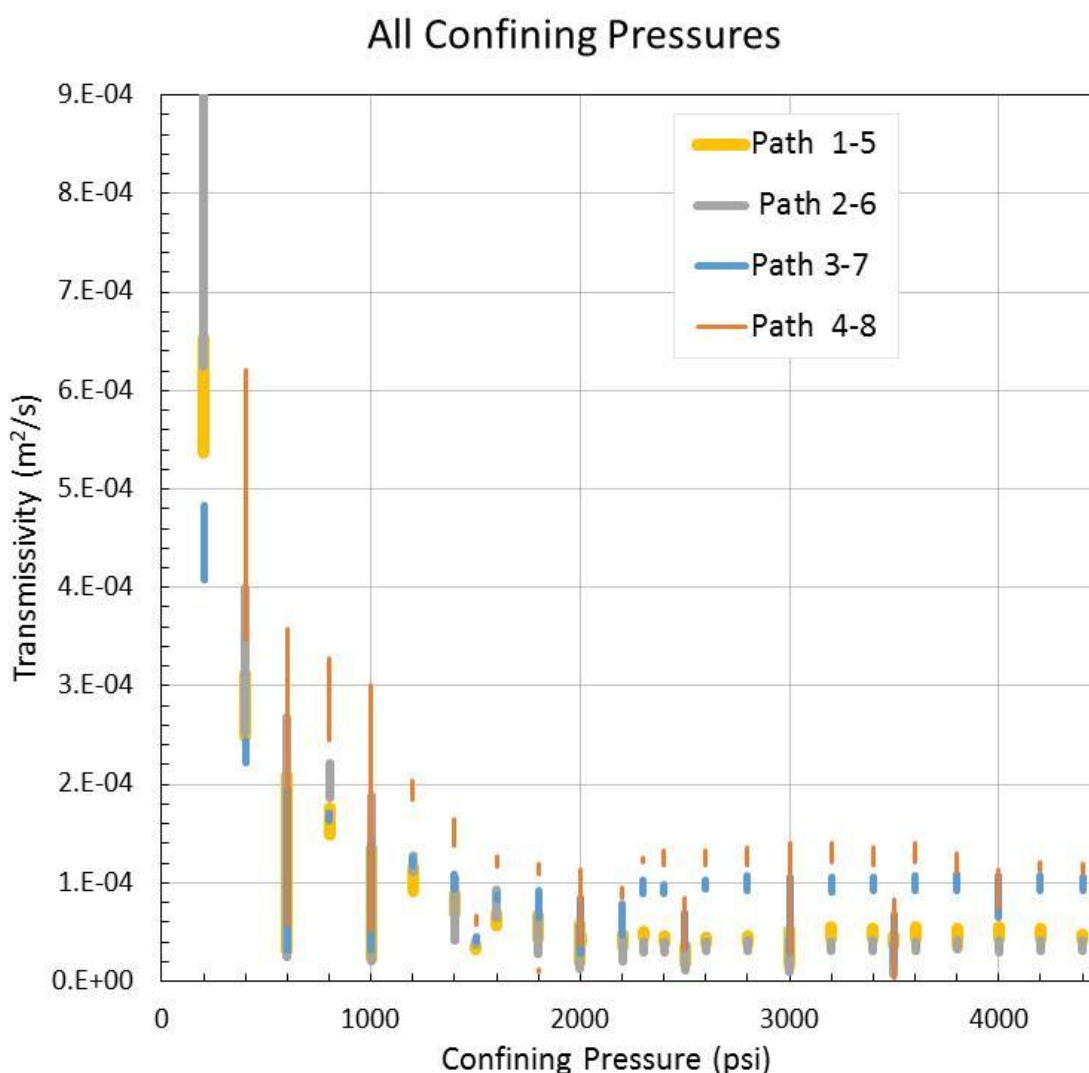


Figure 4-8. Transmissivities of various flow paths for Core 211-2 – all experiments conducted in FY17. Transmissivity for each path is shown with a different line thickness, to enable overlapping values to be seen.

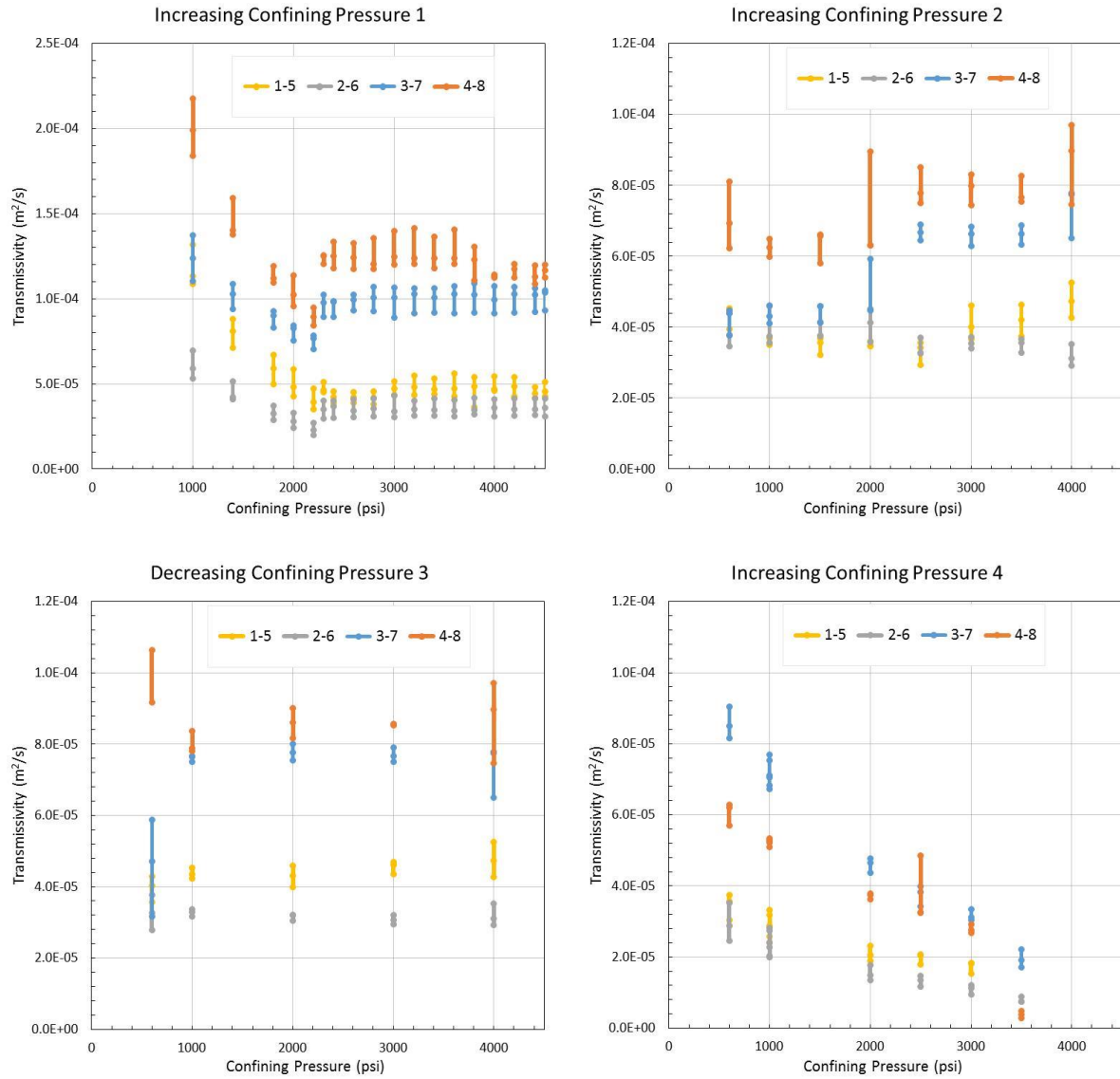


Figure 4-9. Transmissivities of various flow paths for Core 211-2 – individual cycles of FY17 data.

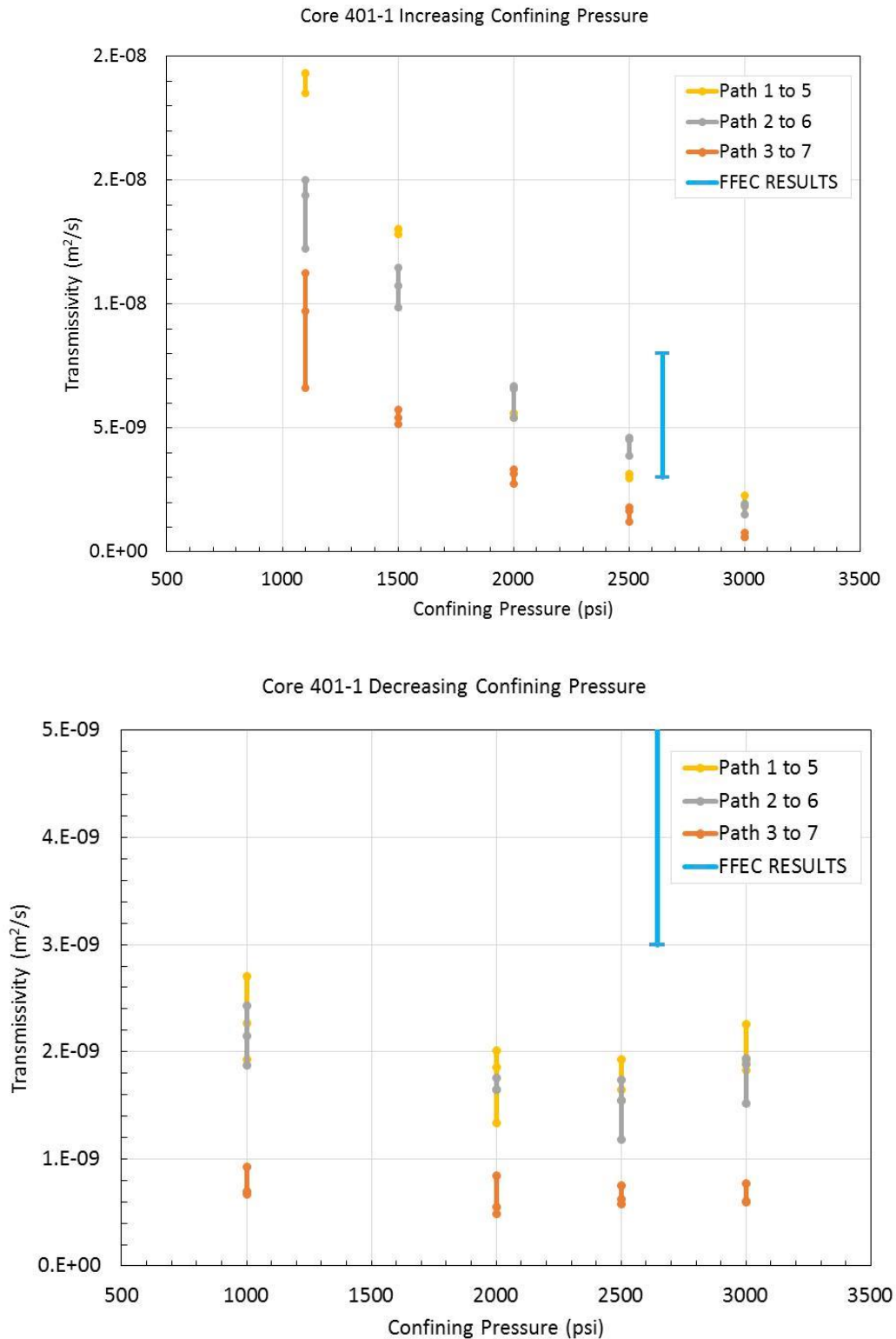


Figure 4-10. Transmissivities of various flow paths for Core 401-1 experiments conducted in FY17, and the transmissivity inferred from FFEC logging in the field. The transmissivity of Path 4 to 8 is zero.

around the edge. As can be seen in Table 4-2, the resultant transmissivities of Path 1 to 5 and Path 3 to 7 did not change significantly, while transmissivity for Path 4 to 8 decreased and that for Path 2 to 6 increased, possibly due to some sealing of the fracture near port 8, and propping open of the fracture near port 6. The large change in transmissivities apparent by comparing Tables 4-1 and 4-2 demonstrates that very different flow behavior can exist depending on the path through the fracture. The reverse direction flow was not measured in this system.

Table 4-2. Transmissivity of Core 211-2 altered by applying cementing compound to gaps at core edge near port 8. All values in m²/s.

Path	Forward	Std. Dev.
1 to 5	3.0×10^{-5}	7.7×10^{-6}
2 to 6	2.7×10^{-4}	9.0×10^{-5}
3 to 7	6.6×10^{-5}	1.1×10^{-5}
4 to 8	6.7×10^{-7}	1.9×10^{-7}

Core 401-1. Core 401-1 was selected for further study because the transmissivities obtained in FY17 were comparable to those obtained in the field by FFEC logging. However, Core 401-1 has proven to be more difficult to get consistent results from, and further measurements are ongoing. Transmissivity values on this core have been previously measured as on the order of 10^{-9} to 10^{-8} m²/s (Figure 4-10). With this small aperture, lower flow rates and longer equilibrium times are required to assure consistent measurements. In addition, complete water saturation of the fracture is required. To date, measurements in the forward direction have been completed and are shown in Table 4-3.

Table 4-3. Transmissivity of Core 401-1. All values in m²/s.

Path	Forward	Std. Dev.
1 to 5	1.9×10^{-9}	2.1×10^{-10}
2 to 6	4.3×10^{-9}	1.7×10^{-9}
3 to 7	3.7×10^{-9}	9.6×10^{-10}
4 to 8	4.6×10^{-9}	9.0×10^{-10}

Artificial Core. An artificial core with one fracture face smooth and the other artificially roughened with sand paper has been prepared. Initial investigations suggested that the fracture transmissivity is too low to be able to complete laboratory experiments within a reasonable time frame. Therefore, work is underway to increase the relief on the roughened face to increase transmissivity.

4.4 Conclusions

In this work, a novel technique was developed to investigate the effect of the geometry of the fracture on anisotropic flow through fractures in rock cores. The measurements show that fracture transmissivity appears anisotropic—roughly a factor of two difference in different directions, but numerous uncertainties make this finding tentative and provide motivation for future work.

4.4.1 Future Work

More work is ongoing to provide T values for forward and reverse directions on the cores for all flow paths, and also on artificial cores. Two avenues will be followed to try to support our tentative findings of observing anisotropy: use of artificial cores and numerical modeling.

For the artificial cores, we will purposefully attempt to produce fractures with anisotropic transmissivity distributions, by means of directional sanding, etching, gouging, etc. Additionally, the engineered nature of the artificial cores should minimize problems like broken edges that allow circumferential flow.

A numerical modeling component of the fracture is just getting underway. The aperture distributions shown in Figure 4-2(a) can be digitally represented by two-dimensional arrays of aperture values, each representing a 0.2 mm by 0.2 mm pixel. A 2D numerical model with grid size equal to pixel size will be constructed, with each cell having a transmissivity calculated from the aperture using the cubic law. Inlet and outlet ports will be located at their actual locations and will act as constant-rate mass sources and sinks. Differential pressure across the flow paths will be used to calibrate the model to the laboratory experiments. Previous studies comparing models and laboratory experiments conducted in transparent fracture replicas (Geller et al., 1995) indicated that subtracting a constant thickness from all aperture measurements was required to obtain a good match for the flow field. Here, direct visualization of flow paths is not possible because of the opaque core, sleeve, etc., but all the differential pressure values from the four pairs of ports should provide adequate constraints on the model.

If numerical modeling of cores 211-2 and 401-1 is promising, additional numerical models for cores 84Z and 188-4 and artificial cores may be developed.

There will be two key outputs of the numerical models:

- (1) The model adjustments required to match the laboratory differential pressures will provide insight into the fracture response to confining pressure.
- (2) The flow paths through the fracture will verify whether the laboratory experiments actually show anisotropic fracture flow, or whether artifacts such as circumferential flow are occurring, and what its magnitude is.

This page intentionally left blank.

5. FRACTURES AND FLUID FLOW IN CRYSTALLINE ROCKS – EXAMPLE FROM THE COSC-1 BOREHOLE, SWEDEN

5.1. Introduction

Low permeability crystalline rocks have long been considered as one of the important potential geologic environments for long term disposal of nuclear waste (e.g., Witherspoon et al., 1981; Bredehoeft and Maini, 1981). However, one key concern relating to this geologic disposal option is the presence of hydraulically conductive fractures that could result in transport of radionuclides (Cherry et al., 2014). Extensive field studies conducted at a number of underground research laboratories in crystalline rocks, such as the Stripa Mine in Sweden and the Grimsel Test Site in Switzerland, have revealed that often a small subset of measured fractures (Figure 5-1) is responsible for the bulk of the observed fluid flow (e.g., Witherspoon and Gale, 1982; Olsson and Gale, 1995; Carbonell et al., 2010). In the case of Stripa, three major fracture zones identified within the characterization study area accounted for 75% of the hydraulic transmissivity as measured by single-hole hydraulic tests (Olsson and Gale, 1995); the orientation of these features is correlated with both small scale fractures as well as regional lineaments.

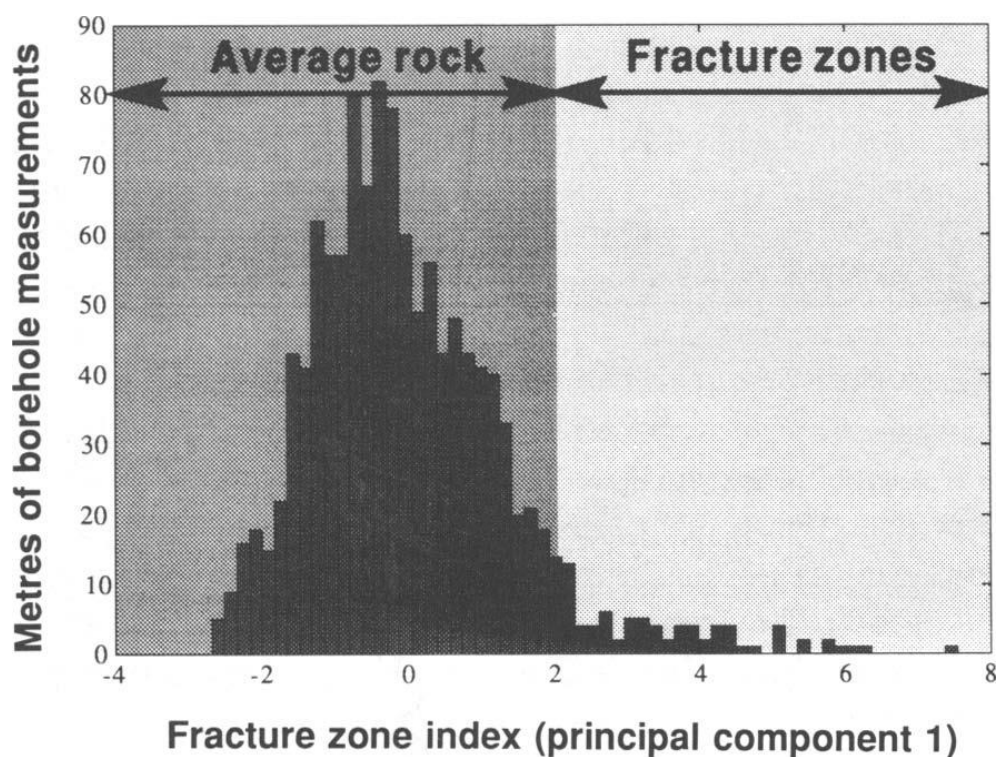
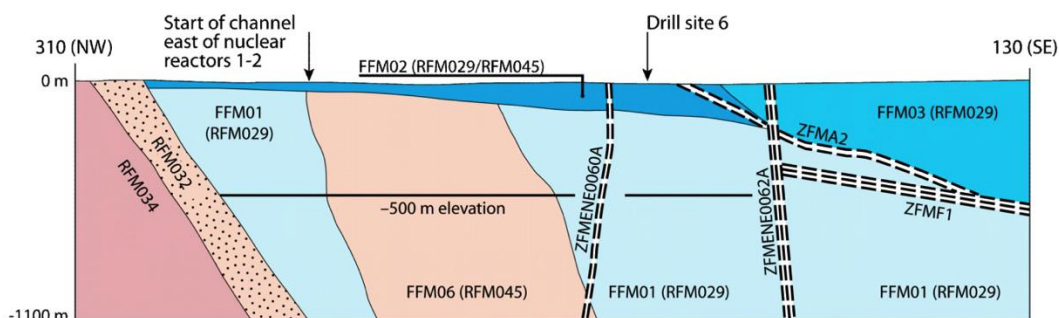


Figure 5-1. Frequency histogram of 'Fracture Zone Index (FZI)' values for 1 m long borehole intervals at Stripa. Intervals with an FZI value greater than 2 were considered part of a fracture zone. FZI was determined through a linear combination of data from borehole measurements of electric resistivity, sonic velocity, hydraulic conductivity, fracture frequency and occurrence of single-hole radar reflectors (Olsson and Gale, 1995).

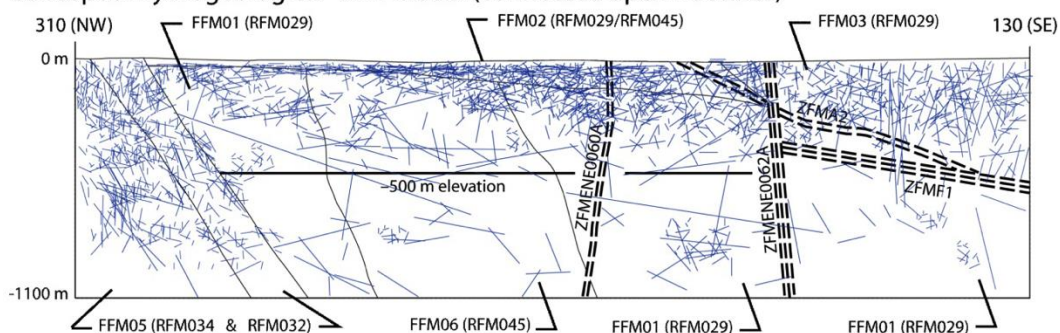
Several countries are currently in the process of developing geologic repositories for spent nuclear fuel in crystalline rock: two of the most advanced projects utilizing this approach are the Forsmark site in Sweden and the ONKALO facility in Olkiluoto, Finland (Lundqvist and Hammarström, 2016; Lahti, 2016). At Fosmark, extensive field tests were conducted to develop a comprehensive conceptual model (Figure 5-2) that identified hydraulically conductive fracture systems (Lundqvist and Hammarström,

2016), which could then be used to develop hydrogeological flow models to constrain safety cases (Hartley and Joyce, 2013; Follin et al., 2014).

Conceptual fracture domain model



Conceptual hydrogeological DFN model (connected open fractures)



Conceptual distribution of modelled end-members:

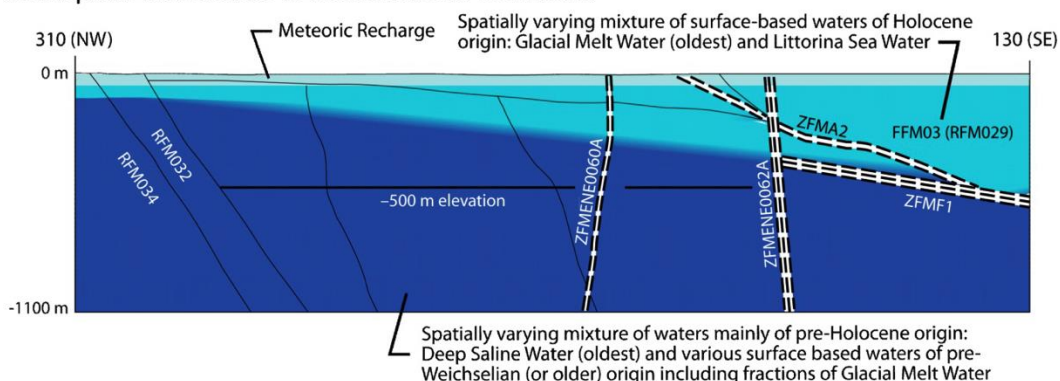


Figure 5-2. Conceptual geological-hydrogeological models, showing fracture domains, connected open fractures, and fracture end-members at Forsmark (Lundqvist and Hammarström, 2016).

Previous studies of a range of crystalline repository options (DOE, 1986) form one of the generic repository options currently under consideration (Hansen et al., 2011; Recharad et al., 2011). One key factor for this type of geologic repository is that discontinuities such as faults, joints, and fractures serve as the primary controls for groundwater flow in low permeability crystalline rocks; thus the frequency, size, orientation, and transmissivity of fractures are key attributes that need to be determined during site characterization (Patera, 1986; Recharad et al., 2011). These fracture attributes then can be used to develop

discrete fracture network and equivalent continuum models for simulating flow and transport (Hadgu et al., 2017).

Thus, fracture characterization remains a critical component for evaluating the safety case for potential crystalline repositories. This report provides some insights into fracture characterization and fracture-controlled fluid flow obtained from studies conducted at a crystalline analog site in Sweden, the COSC-1 borehole.

5.2 Fracture Characteristics of the COSC-1 Borehole

5.2.1 Introduction to the COSC-1 Project

The COSC-1 borehole was drilled as part of the Collisional Orogeny in the Scandinavian Caledonides (COSC) scientific deep drilling project in central Sweden (Lorenz et al., 2015). The well was drilled to a depth of 2.5 km through the Seve Nappe, which contains high grade metamorphic rocks indicative of deep (100 km) crustal levels (Figure 5-3). The main lithologies encountered in the borehole consist of felsic gneisses, amphibolite gneisses, calc-silicate gneisses, amphibolite, migmatites, and garnet mica schists, with discrete zones of mylonite and microkarst. The primary objectives of this project were to gain insights into the tectonic evolution of the area, calibrate high quality surface geophysics through deep drilling, characterize present and past deep fluid circulation patterns, determine current heat flow to constrain climate modeling, and characterize the deep biosphere (e.g., Lorenz et al., 2015; Hedin et al., 2016; Wenning et al., 2016, 2017).

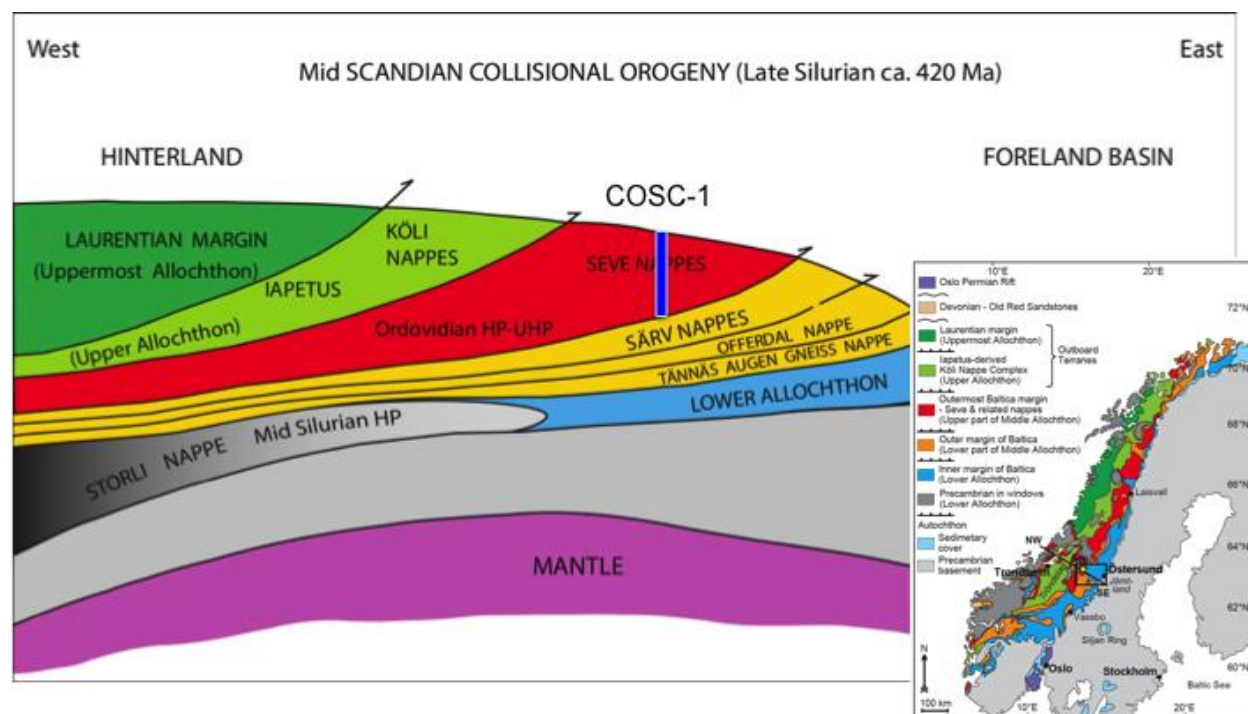


Figure 5-3. Geology and location of the COSC-1 deep borehole (Gee et al., 2013; Lorenz et al., 2015).

Our research team at LBNL has been collaborating with the COSC project to use information from this deep borehole research study as an analog for the deep borehole environment and to develop insights into

fluid flow in crystalline basement rocks. Our team has previously used Flowing Fluid Electrical Conductivity (FFEC) logging as a means of identifying hydrologically transmissive fractures in the deep borehole (e.g., Tsang et al., 2016; Doughty et al., 2017). This component of our study seeks to evaluate the correlation of these identified flow zones with potential correlative fractures observed in image logs and core samples.

5.2.2 Fracture Systematics of the COSC-1 Borehole

Wenning et al. (2017) conducted an extensive characterization of fractures, foliation, and in situ stress of the COSC-1 borehole through the examination of borehole acoustic televiewer image logs. They were able to characterize the *in situ* stress through the evaluation of borehole breakout and drilling induced tensile fractures in the borehole, calculating an orientation for S_{Hmax} of $127^\circ \pm 12^\circ$ based on analysis of 50 breakouts. This orientation is consistent with the regional NW-SE trend observed from boreholes, overcoring, and focal mechanisms (Wenning et al., 2017). Two main structural features were observed in the image logs – foliation and steeply dipping natural fractures (Figure 5-4). A total of 249 natural fractures were identified – they had variable orientations at depths less than 800 m, but had a consistent NW-SE strike with steep dips ($> 70^\circ$) to the NE below this depth. Foliations tended to have much shallower dips and were generally parallel to lithologic contacts – their variability has been attributed to the tight recumbent folding in the Seve Nappe (Wenning et al., 2017). Fractures that were along foliations were not distinguished from foliations – thus there are likely two distinct fracture types: the steeply dipping fractures that were identified as natural fractures, and shallower dipping foliation-parallel fractures. The features recorded in the image logs do not distinguish between open and mineral-filled fractures. The orientation of the steeply dipping fractures below 800 m were interpreted by Wenning et al. (2017) to be consistent with extensional or hybrid brittle shear failure under the current stress regime.

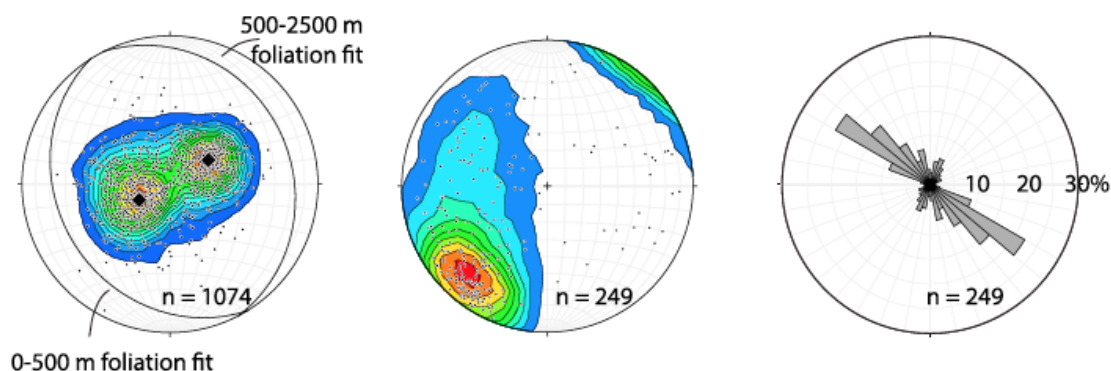


Figure 5-4. Left - Lower hemisphere Schmidt equal area projection of the poles to the foliation planes (black circles) depicting the primary shallow (0–500 m) and deep (500–2500 m) foliation trends. Center - Lower hemisphere Schmidt equal area projection of the poles (black circles) to the natural fracture planes. Right - Rose diagram of the orientation of the natural fractures. (Wenning et al., 2017).

5.2.3 Fractures Associated With Permeable Features Identified from FFEC Logging

Flowing Fluid Electric Conductivity (FFEC) logging is a technique that uses contrasts in wellbore and formation fluid salinities to identify permeable inflow zones in a wellbore (e.g., Tsang and Doughty, 2003). This logging method was applied first to the COSC-1 well during a break in drilling in 2014, and again in 2015 after the well had been completed (Tsang et al., 2016; Doughty et al., 2017). Analysis of the

results of these logging runs indicated the presence of fluid entry points in the boreholes at depths of 228, 338-339, 507-508, 553-554, 696, 1214, 1243-1245, 2300, and 2380 m. Selected core samples that appeared to contain fractures that roughly corresponded to these depth intervals were obtained by Chin-Fu Tsang and sent to LBNL for further study. A subset of these core samples was used to determine fracture transmissivities under controlled confining stress conditions (Dobson et al., 2017; Chapter 4, this study). One of the objectives of these measurements was to compare the field scale fracture transmissivities obtained from the FFEC studies with the core scale fracture measurements. However, one key concern was whether the core sample fractures actually corresponded to the permeable features that were detected in the boreholes. Thus, the core samples and the FFEC entry points reported by Doughty et al. (2017) were compared to fractures and foliations that were identified in the acoustic televiewer image logs by Wenning et al. (2017); these results are summarized in Table 5-1.

One aspect of this correlation work is that the depths reported for the core samples, FFEC logging, and image log data may be slightly off due to a number of technical reasons at the field site. Benoît Dessirier, a member of the COSC team at Uppsala University, used gamma log data from the downhole surveys as well as rock density and magnetic susceptibility data from both the rock core data as well as the downhole surveys to cross-correlate depths between these measurements and bring them into agreement. The offsets appear to be constant down to 1600 m depth (Figure 5-5; Dessirier et al., 2018). This comparison indicates that most of the core samples that were examined are not correlative with the actual FFEC inflow zones, and that neighboring samples might be more appropriate for analysis – these samples are indicated in the right hand column of Table 5-1. In one specific instance (the FFEC peak at 506 m), the studied core (144-2) appears to be at the correct depth interval.

Table 5-1. FFEC peak locations, corresponding core samples, and fractures and foliations in the COSC-1 borehole.

FFEC peak depth (m) (2017 paper)	Corrected FFEC peak depth ¹ (m)	Core sample studied	Core sample depth ² reported (m)	Corrected sample depth ³ (m)	Closest image log fractures (m) *	Closest image log foliations (m) *	More likely core sample
1243	1242	401-1	1242.06	1239.5	1238.62	1241.43 1242.51	401-4
1214	1212	393-3	1219.85	1217	1211.83 1212.68	1211.45	391-2 391-4 392-2
696	694.4	211-2 209-3	702.38 698.0	695.5	696.72	693.98	209-1 209-2
638.5 ⁺		188-4	638.39		618.68	639.16	
553	552.5				543.41	553.49	159-4
508	505.9	144-2 144-1	507.33 506.13	506 505	513.69	504.56	144-2
338	337.2	84-3	340.31	338.5	334.17	335.11 340.95	84-1
288	287				275.37	285.53	

¹Corrected peak depths taken from estimated mid-point depth of FFEC curve peaks corrected by B. Dessirier – these peaks are often are more than 1 m in height.

²Sample depths (for midpoint of core sample) determined from COSC-1 core archive sheet, using MBSF as reference point.

³Approximate sample depth based on gamma log depth correction made by B. Dessirier.

* Fracture and foliation data obtained from supplemental data tables, Wenning et al. (2017)

† Minor FFEC peak – not analyzed.

Samples shown in **bold** have fracture mineralization.

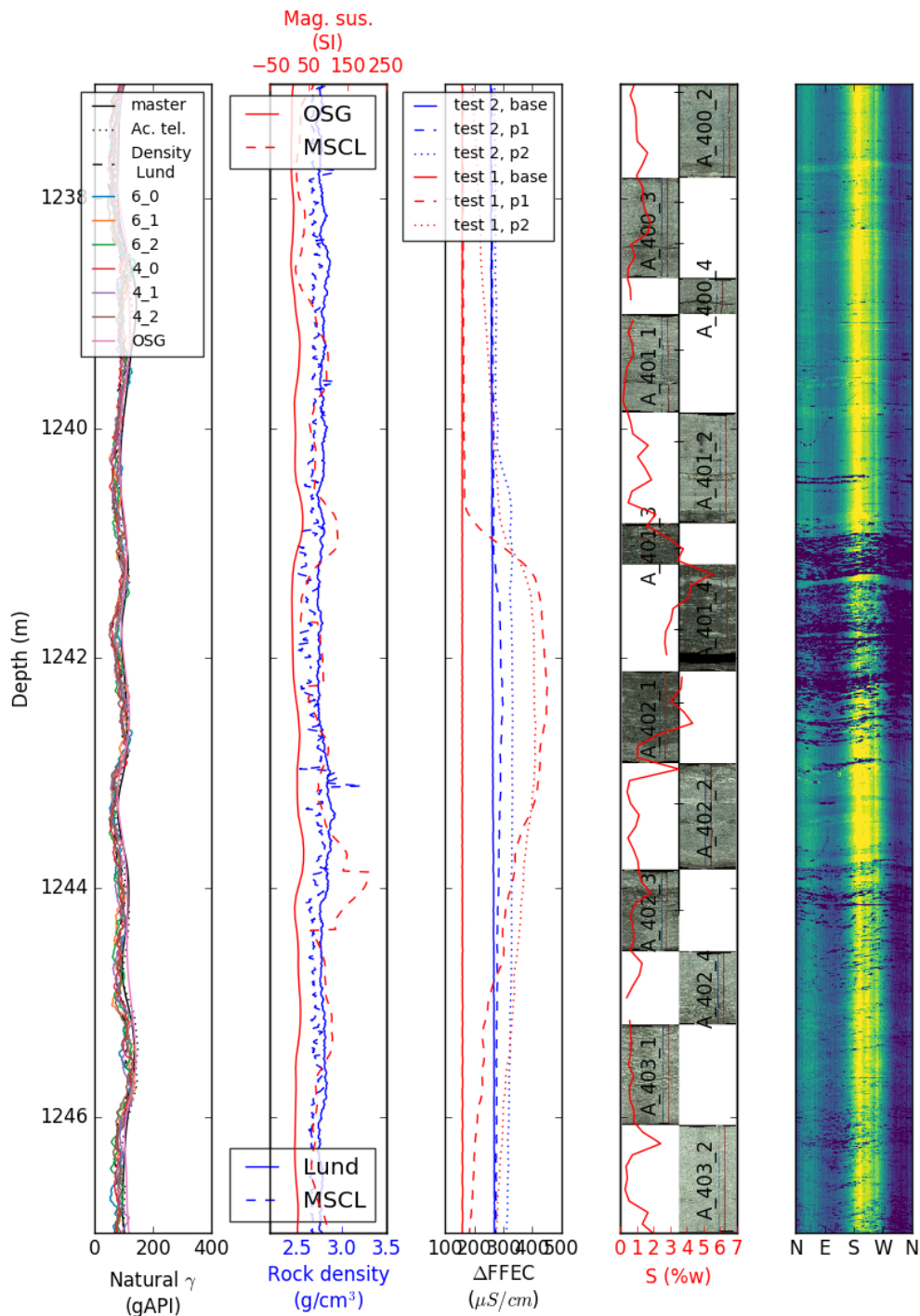

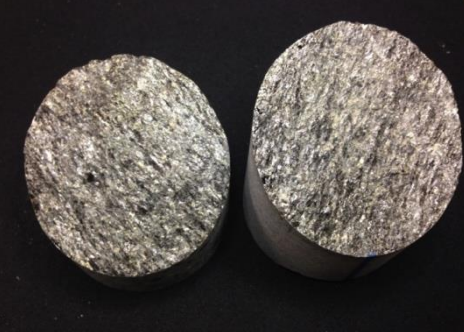

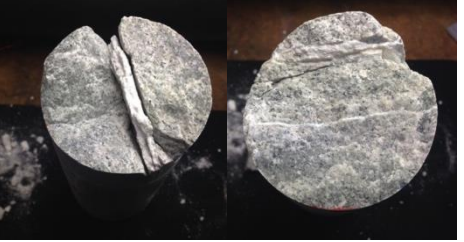






Figure 5-5. Correlation at 1237-1247 m in COSC-1 borehole between natural gamma and rock density/magnetic susceptibility logs used for depth matching (left two columns), the peaks obtained using the FFEC method identifying approximate location of flowing fractures (central column), and the unrolled core image, the sulfur content (wt. %), and the amplitude of the televierer image (right two columns). Correlation conducted by B. Dessirier, Uppsala University.

The core samples listed in the table above were all examined to provide more details on the nature of the fracture (Tables 5-2 and 5-3). All but one of the samples have shallow dipping fractures (or core breaks), parallel to the foliation. Many of the core samples do not have a close-fitting match between the core pieces, casting doubt that they truly represent actual fractures, but instead may be core breaks along foliation that were then damaged in the core barrel, resulting in the poor mating of the samples. Three of the samples (393-3, 188-4 and 144-2) have mineralization on the fracture surface, suggesting that these samples indeed do represent mineralized fractures.

Table 5-2. Photos of COSC-1 core samples.

Core sample	Photo of core pieces	Photo of fracture surface
401-1		
393-3		
211-2		
209-3		



Core samples are 60 mm in diameter. White material seen on core faces 211-2 and 209-3 is sealing material introduced to core during fracture flow experiments and not natural mineralization. White material seen on core faces 188-4 and 144-4 is mineralization (see Table 5-3).

Table 5-3. Observations of fractures in COSC-1 core samples.

Core sample	Rock type	Dip of fracture (geometric)	Dip of fracture (goniometer)	Parallel to foliation?	Fitting of core pieces	Fracture mineralization
401-1	Gneiss / microkarst	25		Yes	Good	No
393-3	Microkarst	>80		No	Good	Yes
211-2	Amphibolite	12	12	Yes	Moderate	No
209-3	Gneiss / amphibolite	6	10	Yes	Poor	No
188-4	Gneiss	13	14	Yes	Moderate	Yes
144-2	Gneiss	11	15	Yes	Poor	Yes
144-1	Gneiss	4	6	Yes	Moderate	No
84-3	Gneiss	21	18	Yes	Moderate	No

Fracture dips were estimated using two approaches. The height to the fracture top and bottom of the cores were used together with the core diameter to calculate the dip angle. A goniometer was also used to estimate the steepest dip angle of the core.

5.2.4 Analysis of Fracture Mineralization of Selected Core Samples Using X-Ray Diffraction (XRD)

Samples of secondary mineralization were collected by scraping the fracture surface with a steel razor blade. The collected fragments were then reduced into powder using an agate mortar and pestle. A small amount of powder was deposited onto a glass slide placed in an aluminum sample stage. Samples were spun during the data collection to improve counting statistics. The instrument used was a Rigaku SmartLab[®], and data were collected from 5° to 72° of 2θ, using Kα radiation (instrument operating at 40kV and 44 mA). After manual identification of the mineral phases, a Rietveld analysis of the collected X-ray powder diffraction (XRPD) profile (e.g. Young, 1993) was performed on both samples to obtain weight fractions and to further validate the correctness of the phase identification procedure.

The mineral coating on the fracture face of sample 144-2 consisted of a white platy coating that was observed on a small portion of the fracture. The Rietveld analysis of this sample (Figure 5-6) shows thaumasite (Ca₃Si(OH)₆(CO₃)(SO₄)·12H₂O) as the most abundant mineral phase (85% by weight), a mineral from the group of micas, fitted using a muscovite structure, as the second most abundant phase (12%), and the third phase was identified as aerinite (Ca₄(Al,Fe,Mg)₁₀Si₁₂O₃₅(OH)₁₂CO₃·12H₂O) (3%).

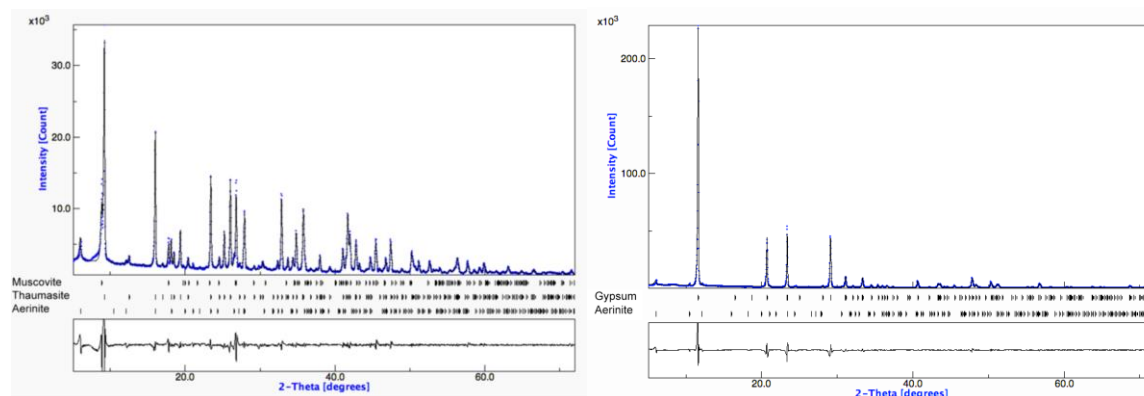


Figure 5-6. X-ray powder diffraction profile for fracture mineralization for samples 144-2 (left) and 188-4 (right), where the blue dots are the measured data and the black line is the Rietveld model. The peak positions for each phase are marked at the bottom.

The fracture coating sampled from 188-4 is composed almost exclusively by gypsum (Figure 5-6). It is observed coating one of the two fracture faces, present as white and glassy mineralization. Small (<1%) but clear traces of aerinite are still present. The presence of gypsum ($\text{CaSO}_4 \cdot 2\text{H}_2\text{O}$) in this sample is of particular interest. The COSC group at Uppsala (Dessirier et al., 2018) noted a correlation between increased S contents of core samples and the presence of fluid flow zones (Figure 5-5, fourth column). If these fractures have gypsum mineralization, this would help explain this correlation. The waters that were sampled from the COSC-1 borehole are primarily $\text{Ca-SO}_4\text{-HCO}_3$ waters (Figure 5-7) (Dobson et al., 2016), so that gypsum could be expected as a potential mineral precipitating from such fluids. Thaumassite (the main mineral phase of the mineralized fracture in sample 144-2) also contains SO_4 , so it could also be an indicator of flowing (and sealed) fractures.

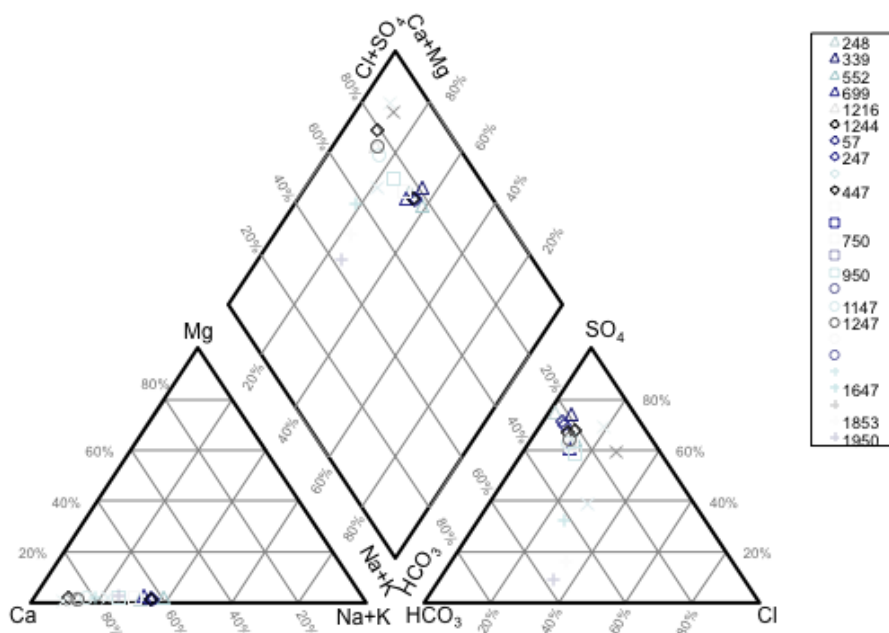


Figure 5-7. Piper diagram of borehole waters from COSC-1 well (Dobson et al., 2016).

5.3 Correlation of FFEC Flow Zones with Fracture Features and Future Work

While many of the core samples that were examined do not appear to spatially correlate with the FFEC inflow zones (Table 5-1) due to the recalibration of the core and logging depths, these zones do not appear to correspond to steeply dipping fracture features that were identified in the acoustic televiewer image logs either (Wenning et al., 2017). This observation was somewhat surprising, given that the steeply dipping fractures appear to be features that crosscut the foliation and would seem to be better candidates for hosting fluid flow within the low permeability crystalline rock. Using the core to FFEC log correlations developed by Benoît Dessirier, in most cases, foliation-parallel fractures are observed adjacent to the FFEC log peaks. Because most of the FFEC peaks are quite extensive (over 1 m), in many cases, there are multiple fracture/foliation features that may correspond to the inflow zones. The presence of increased sulfur contents in the core samples that are associated with some of the fractures in the vicinity of the flow zones may suggest the presence of a sulfate-bearing fracture mineral phase, such as gypsum or thaumasite, on the fracture surface. A number of additional core samples with fractures have been identified as possible candidates for hosting these flow zones. Two of the main fluid flow regions that were identified by the FFEC logging (1212 and 1242 m) also appear to be associated with a microkarstic region – localized dissolution may also enhance fluid flow in this region. It would be helpful to revisit additional core samples using the revised depth correlation (Table 5-1) to see if any additional fracture features are observed, and whether these also have sulfur-bearing secondary mineralization. It would also be helpful to see if the steeper dipping fractures identified in the televiewer logs have been sealed by mineralization.

This page intentionally left blank.

6. SUMMARY OF FY2018 PROGRESS AND FUTURE WORK

According to the Used Fuel Disposition Disposal R&D roadmap, based on an analysis of key features, events, and processes, which are important to the safety case for radioactive waste disposal, the main research priorities relevant to the evaluation of the possibility of disposal in crystalline rock include the evaluation of host rock properties, flow and transport pathways and processes in crystalline media, and the excavation disturbed zone.

The LBNL R&D activities during FY18 related to crystalline disposal addressed the following key issues: preliminary numerical simulations of the impact of gas bubble generation and migration on fracture growth and radionuclide migration, laboratory experiments and numerical simulations of how the excavation disturbed zone could impact local fluid flow properties in crystalline rocks, and the use of a crystalline basement analog site in Sweden to evaluate core-scale fracture transmissivity and to compare identified flow zones with different fracture sets observed from acoustic televiewer logs and core studies.

In particular, a new modeling activity was initiated during FY18 to simulate gas bubble migration. Gas bubbles, which are known to be produced by metal corrosion, radiolysis of trapped water, or by microorganisms, could impact the migration of radionuclides and could also cause fracturing of the crystalline rock mass if sufficient overpressures are generated. The preliminary modeling work was conducted to evaluate the migration of gas bubbles within different synthetic pore structures, and directions of research are identified to evaluate the potential impact of gas migration on radionuclide migration.

During FY18, a series of laboratory experiments were conducted on granite slabs with a special geometry to replicate the stresses and rock deformation responses that are expected to occur in larger circular excavations of the excavation damage zone (EDZ) in a mined crystalline repository. Specifically, microcracks generated by applying stress to the shaped rock samples were observed both visually and through a pronounced decrease in seismic velocity. The stressed samples were also used to assess the changes in rock permeability as an indicator how these microcracks could affect hydraulic properties of rock in the EDZ. Preliminary modeling studies of flow and transport coupled process and the effects of the rock deformation on hydrological and transport properties were initiated using a rigid body spring network modeling approach.

The final two sections of the report are based on the results of investigations of rock samples and data from a crystalline basement analogue site in central Sweden, the 2.5 km deep “Collisional Orogeny in the Scandinavian Caledonides” (COSC) scientific borehole. This study is aimed at gaining insights into the flow characteristics of crystalline basement rocks. The first part of this task included a series of laboratory experiments on fractured cores that were selected based on the correlation with the borehole inflow zones identified from flowing fluid electrical conductivity (FFEC) logs. These core flow measurements were conducted using a unique laboratory apparatus that can measure multi-directional transmissivity to assess fracture anisotropy under confining stress conditions. One challenge that was observed is that some of the core appears to have been damaged during recovery from the borehole, so that the core transmissivity measurements are significantly higher than the field scale values calculated from the FFEC logging runs. The second part of this task involved the evaluation of the nature of the fractures that appear to be linked to the borehole inflow zones, which were identified from the FFEC field measurements. Acoustic borehole televiewer images of the COSC-1 borehole indicated that there were two distinct sets of fractures: (a) steeply dipping fractures that were generated by current tectonic stresses, and (b) shallow fractures parallel to rock foliation. Based on new depth correlations of the core and well log datasets, it appears that the majority of the inflow zones are associated with the foliation-parallel fractures.

Based on the LBNL FY18 results, we have identified a number of areas that merit additional study in FY19. The initial results of the gas bubble migration study will be extended to perform simulations of bubble transport in fractures. The EDZ laboratory experiments are planned to be conducted on samples from the Grimsel URL, such as the FEBEX experiment. The COSC-1 analogue study will be completed in FY19; we may request some additional core samples to evaluate the spatial correlation with the actual FFEC inflow zones. The results of the COSC-1 analogue study will be included in a paper to be submitted to a peer-reviewed journal.

7 ACKNOWLEDGMENTS

The author of Section 2 would like to thank Dr. Chun Chang at Lawrence Berkeley National Laboratory for providing the experimental information for model verification, and thank Dr. Stephane Gaboreau at BRGM, France for providing the digital data of the two rock volumes.

We thank the members of the COSC scientific team for generously sharing their data and ideas on the COSC-1 project. The International Continental Scientific Drilling Program (ICDP) and the Swedish Research Council financed the drilling of the COSC-1 borehole (VR: Grant 2013–94). We also thank Hao Xu and Boris Faybishenko for their scientific review of this work, and Boris Faybishenko and Cynthia Tilton for their editorial reviews. Funding for this work was provided by the Spent Fuel and Waste Disposition Science and Technology Campaign, Office of Nuclear Energy, of the U.S. Department of Energy under Contract Number DE-AC02-05CH11231 with Lawrence Berkeley National Laboratory.

This page intentionally left blank.

8 REFERENCES

- Abu-Al-Saud, M. O., Riaz, A., Tchelepi, H. A. (2017) Multiscale level-set method for accurate modeling of immiscible two-phase flow with deposited thin films on solid surfaces. *Journal of Computational Physics* 2017, 333, 297-320.
- Adrian, M. S., Hisham, B. M., Andrew, J. K. (2016) Comparison of Two-Phase Pipe Flow in OpenFOAM with a Mechanistic Model. *IOP Conference Series: Materials Science and Engineering*, 121, (1), 012018.
- Armstrong, R. T., Evseev, N., Koroteev, D., Berg, S. (2015) Modeling the velocity field during Haines jumps in porous media. *Advances in Water Resources*, 77, 57-68.
- Asahina, D., Aoyagi, K., Kim, K., Birkholzer, J.T., and Bolander, J.E. (2017) Elastically-homogeneous lattice models of damage in geomaterials, *Computers and Geotechnics*, 81, 195– 206.
- Berg, S.; Ott, H.; Klapp, S. A.; Schwing, A.; Neiteler, R.; Brussee, N.; Makurat, A.; Leu, L.; Enzmann, F.; Schwarz, J. O.; Kersten, M.; Irvine, S.; Stampanoni, M. (2013) Real-time 3D imaging of Haines jumps in porous media flow. *Proceedings of the National Academy of Sciences of the United States of America*, 110, (10), 3755-3759.
- Birkholzer, J.; Houseworth, J.; Tsang, C. F. (2012) Geologic Disposal of High-Level Radioactive Waste: Status, Key Issues, and Trends. *Annual Review of Environment and Resources*, Vol 37 2012, 37, 79-106.
- Blunt, M. J.; Bijeljic, B.; Dong, H.; Gharbi, O.; Iglauer, S.; Mostaghimi, P.; Paluszny, A.; Pentland, C. (2013) Pore-scale imaging and modelling. *Advances in Water Resources*, 51, 197-216.
- Bolander, J.E. and Saito, S. (1998) Fracture analyses using spring networks with random geometry, *Eng. Fract. Mech.*, 61, 569–91.
- Bredehoeft, J.D., and Maini, T. (1981) Strategy for radioactive waste disposal in crystalline rocks. *Science* 423 (4505), 293–296.
- Bultreys, T.; Boone, M. A.; Boone, M. N.; De Schryver, T.; Masschaele, B.; Van Hoorebeke, L.; Cnudde, V. (2016) Fast laboratory-based micro-computed tomography for pore-scale research: Illustrative experiments and perspectives on the future. *Advances in Water Resources*, 95, 341-351.
- Carbonell, R., Pérez-Estaún, A., Martínez-Landa, L., Martí, D., and Carretero, G. (2010) Geophysical and geological characterization of fractures within granitic pluton. *Near Surface Geophysics* 8 (3), 181–193.
- Chang, C.; Ju, Y.; Xie, H. P.; Zhou, Q. L.; Gao, F. (2017) Non-Darcy interfacial dynamics of air-water two-phase flow in rough fractures under drainage conditions. *Scientific Reports*, 7.
- Cherry, J.A., Alley, W.M., and Parker, B.L. (2014) Geologic disposal of spent nuclear fuel – An earth science perspective. *The Bridge*, Spring 2014, 51–59.
- Christensen, H.; and Sunder, S. (2000) Current state of knowledge of water radiolysis effects on spent nuclear fuel corrosion. *Nuclear Technology*, 131, (1), 102-123.
- Cihan, A.; and Corapcioglu, M. Y.(2008) Effect of compressibility on the rise velocity of an air bubble in porous media. *Water Resources Research*, 44, (4).
- Claret, F., Marty, N., and Tournassat, C, (2018) Modeling the Long-term Stability of Multi-barrier Systems for Nuclear Waste Disposal in Geological Clay Formations. *Reactive Transport Modeling*.
- Deshpande, S. S.; Anumolu, L.; Trujillo, M. F. (2012) Evaluating the performance of the two-phase flow solver interFoam. *Computational Science and Discovery*, 5, (1).

- Dessirier B., Hedayati, M., Tsang, C.F., and Niemi, A. (2018) A study of correlating hydraulically transmissive zones at the COSC deep borehole with geological, geophysical and geochemical logging data from downhole surveys and core samples, in preparation.
- Dobson, P., Tsang, C.F., Doughty, C., Ahonen, L., Kietäväinen, R., Juhlin, C., Rosberg, J.E., Borglin, S., Kneafsey, T., Rutqvist, J., Zheng, L., Xu, H., Nakagawa, S., and Nihei, K. (2017) Deep borehole field test activities at LBNL 2017. US DOE Spent Fuel and Waste Science and Technology, SFWD-SFWST-2017-000046, LBNL Report 2001043, 118 p.
- Dobson, P., Tsang, C.F., Kneafsey, T., Borglin, S., Piceno, Y., Andersen, G., Nakagawa, S., Nihei, K., Rutqvist, J., Doughty, C., and Reagan, M. (2016) Deep Borehole Field Test Research Activities at LBNL. Prepared for U.S. Department of Energy Used Fuel Disposition Campaign, FCRD-UFD-2016-000438, LBNL Report LBNL-1006044.
- DOE (1986) Draft area recommendation report for the crystalline repository project. U.S. Department of Energy Office of Civilian Radioactive Waste Management, Crystalline Repository Project Office, DOE/CH-15(O), DE87 012335.
- Doughty, C. Tsang, C-F., Rosberg, J-E., Juhlin, C., Dobson, P.F. and Birkholzer, J.T. (2017) Flowing fluid electrical conductivity logging of a deep borehole during and following drilling: estimation of transmissivity, water salinity and hydraulic head of conductive zones, *Hydrogeol J* 25:501–517 DOI 10.1007/s10040-016-1497-5
- Doughty, C., Tsang, C.F., Rosberg, J.E., Juhlin, C., Dobson, P.F., and Birkholzer, J.T. (2017) Flowing fluid electrical conductivity logging of a deep borehole during and following drilling: estimation of transmissivity, water salinity and hydraulic head of conductive zones. *Hydrogeology Journal* 25, 501–517.
- Duan, K. and Kwok, C.Y. (2015) Evolution of stress-induced borehole breakout in inherently anisotropic rock: Insights from discrete element modeling, *J. Geophys. Res., Solid Earth*, 121, 2361-2381, DOI:10.1002/2015JB012676.
- Follin, S., Hartley, L., Rhén, I., Jackson, P., Joyce, S., Roberts, D., and Swift, B. (2014) A methodology to constrain the parameters of a hydrogeological discrete fracture network model for sparsely fractured crystalline rock, exemplified by data from the proposed high-level nuclear waste repository site at Forsmark, Sweden. *Hydrogeology Journal* 22, 313–331.
- Gaboreau, S., Robinet, J. C., Pret, D. (2016) Optimization of pore-network characterization of a compacted clay material by TEM and FIB/SEM imaging. *Microporous and Mesoporous Materials*, 224, 116-128.
- Gee, D.G., Janák, M., Majka, J., Robinson, P., and van Roermund, H. (2013) Subduction along and within the Baltoscandian margin during closing of the Iapetus Ocean and Baltica-Laurentia collision, *Lithosphere* 5, 169–178.
- Geller, J.T., Doughty, C., Long, J.C.S. and Glass, R.J. (1995) Disturbed zone effects: Two-phase flow in regionally water-saturated fractured rock: FY94 Annual Report, Rep. LBL-36848, Lawrence Berkeley Lab., Berkeley, CA.,
- Hadgu, T., Karra, S., Kalinina, E., Makedonska, N., Hyman, J.D., Klise, K., Viswanathan, H.S., and Wang, Y. (2017) A comparative study of discrete fracture network and equivalent continuum models for simulating flow and transport in the far field of a hypothetical nuclear waste repository in crystalline host rock. *Journal of Hydrology* 553, 59–70.
- Hansen, F.D., Hardin, E., and Orrell, A. (2011) Geologic disposal options in the USA. Proceedings, International High Level Radioactive Waste Management Conference 2011, Albuquerque, NM, 932–940.

- Hartley, L., and Joyce, S. (2013) Approaches and algorithms for groundwater flow modeling in support of site investigations and safety assessment of the Forsmark site, Sweden. *Journal of Hydrology* 500, 200–216.
- Hedin, P., Almqvist, B., Berthet, T., Juhlin, C., Buske, S., Simon, H., Giese, R., Krauß, F., Rosburg, J.-E., and Alm, P.-G. (2016) 3D reflection seismic imaging at the 2.5 km deep COSC-1 scientific borehole, central Scandinavian Caledonides. *Tectonophysics* 689, 40–55.
- Hoang, D. A.; van Steijn, V.; Portela, L. M.; Kreutzer, M. T.; Kleijn, C. R. (2012) Modeling of low-capillary number segmented flows in microchannels using OpenFOAM. *AIP Conference Proceedings*, 1479, (1), 86-89.
- Jasak, H., (2009) OpenFOAM: Open source CFD in research and industry. *International Journal of Naval Architecture and Ocean Engineering*, 1, (2), 89-94.
- Kawai, T. (1978) New Discrete Models and their Application to Seismic Response Analysis of Structures, *Nuclear Engineering and Design*, 48, 207–229.
- Kim, J.-S.; Kwon, S.-K.; Sanchez, M.; Cho, G.-C. (2011) Geological storage of high level nuclear waste. *KSCE Journal of Civil Engineering*, 15, (4), 721-737.
- Kirsch, E.G. (1898) Die Theorie der Elastizität und die Bedürfnisse der Festigkeitslehre. *Zeitschrift des Vereines deutscher Ingenieure*, 42, 797–807.
- Lahti, M. (2016) Chapter 7: Towards Implementation of the Spent Nuclear Fuel Repository in Finland. In: *International Approaches for Deep Geological Disposal of Nuclear Waste: Geological Challenges in Radioactive Waste Isolation – Fifth Worldwide Review*, B. Faybishenko, J. Birkholzer, D. Sassani, and P. Swift, Eds., Lawrence Berkeley National Laboratory and Sandia National Laboratories, LBNL Report 1006984, pp. 7-1–7-12.
- Lavrov, A. (2003) The Kaiser effect in rocks: principles and stress estimation techniques, *Int. J. Rock Mech. & Min. Sci.*, 40, 151-171.
- LISA ver.8.0.0. <http://www.lisa-fet.com/>
- Lorenz, H., Rosberg, J.E., Juhlin, C., Bjelm, L., Almqvist, B.S.G., Berthet, T., Conze, R., Gee, D.G., Klonowska, I., Pascal, C., Pedersen, K., Roberts, N.M.W., and Tsang, C.F. (2015) COSC-1 – drilling of a subduction-related allochthon in the Palaeozoic Caledonide orogen of Scandinavia, *Scientific Drilling* 19, 1–11.
- Lundqvist, B., and Hammarström, M. (2016) Chapter 20: Licensing of the KBS-3 concept for spent nuclear fuel in Sweden. In: *International Approaches for Deep Geological Disposal of Nuclear Waste: Geological Challenges in Radioactive Waste Isolation – Fifth Worldwide Review*, B. Faybishenko, J. Birkholzer, D. Sassani, and P. Swift, Eds., Lawrence Berkeley National Laboratory and Sandia National Laboratories, LBNL Report 1006984, pp. 20-1–20-25.
- Martin, C.D. (1997) Seventeen Canadian Geotechnical Colloquium: The effect of cohesion loss and stress path on brittle rock strength, *Canadian Geotechnical Journal*, 1997, 34(5): 698-725, <https://doi.org/10.1139/t97-030>
- Martin, C.D., Martino, J.B. and Dzik E.J. (1994) Comparison of borehole breakouts from laboratory and field tests, SPE 28050, SPE/ISRM Rock Mechanics in Petroleum Engineering Conference, Delft, The Netherlands, August 29-31, 183-190.
- McDonald, K.T. (2016) Resistance of a Disk, Joseph Henry Laboratories, Princeton University, Princeton NJ, www.physics.princeton.edu/~mcdonald/examples/resistivedisk.pdf, accessed June 30, 2016)
- Meakin, P.; and Tartakovsky, A. M. (2009) Modeling and simulation of pore-scale multiphase fluid flow and reactive transport in fractured and porous media. *Reviews of Geophysics*, 47, (3), n/a-n/a.

- Nakagawa S. and Ewy, R. (2008) Shaped-Core Uniaxial Compression Test for Studying Borehole Breakout in Rocks, In Proceedings of 42nd US Rock Mechanics Symposium, ARMA-08-158, 29 June-2 July, San Francisco, CA.
- Nieves-Remacha, M. J.; Yang, L.; Jensen, K. F., (2015) OpenFOAM Computational Fluid Dynamic Simulations of Two-Phase Flow and Mass Transfer in an Advanced-Flow Reactor. *Industrial & Engineering Chemistry Research*, 54, (26), 6649-6659.
- Okabe, A., Boots, B., Sugihara, K., and Chiu, S.N. (2000) *Spatial Tessellations: Concepts and Applications of Voronoi Diagrams*, 2nd ed., Wiley, NYC, 696 pages.
- Olsson, O., and Gale, J.E. (1995) Site assessment and characterization for high-level nuclear waste disposal: results from the Stripa Project, Sweden. *Quarterly Journal of Engineering Geology* 28, S17–S30.
- Patera, E.S. (1986) United States Crystalline Repository Project – Key research areas. *Materials Research Society Symposium Proceedings*, v. 50, 17–21.
- Pedersen, K. (1999) Subterranean microorganisms and radioactive waste disposal in Sweden. *Engineering Geology*, 52, (3-4), 163-176.
- Pedersen, K., (1996) Investigations of subterranean bacteria in deep crystalline bedrock and their importance for the disposal of nuclear waste. *Canadian Journal of Microbiology*, 42, (4), 382-391.
- Raeini, Q. A. J., Blunt, M.; Bijeljic, B. (2012) Modelling two-phase flow in porous media at the pore scale using the volume-of-fluid method; Vol. 231, p 5653–5668.
- Rechard, R.P., Goldstein, B., Brush, L.H., Blink, J.A., Sutton, M., and Perry, F.V., (2011) Basis for identification of disposal options for research and development for spent nuclear fuel and high-level waste. *Fuel Cycle Research & Development, U.S DOE Used Fuel Disposition Campaign, FCRD-USED-2011-000071*, 54 p.
- Roman, S., Abu-Al-Saud, M. O., Tokunaga, T., Wan, J. M., Kovscek, A. R., Tchelep, H. A. (2017) Measurements and simulation of liquid films during drainage displacements and snap-off in constricted capillary tubes. *Journal of Colloid and Interface Science*, 507, 279-289.
- Sloan, S.W. (1987) A fast algorithm for constructing Delaunay triangulations in the plan, *Advances in Engineering Software*, 9(1), 34–55.
- Taniguchi, T., Yamashita, Y., and Moriwaki, K. (2002) Generation of arbitrary 3-dimensional domain from nodes on its surface, 8th Conference on Numerical Grid Generation, Hawaii, USA.
- Tsang, C. F.; Neretnieks, I.; Tsang, Y. (2015) Hydrologic issues associated with nuclear waste repositories. *Water Resources Research*, 51, (9), 6923-6972.
- Tsang, C.F. and Doughty, C. (2003) Multirate flowing fluid electric conductivity logging method. *Water Resources Research* 39(12), 1354–1362, doi:10.1029/2003WR002308
- Tsang, C.F., Rosberg, J.E., Sharma, P., Berthet, T., Juhlin, C., and Niemi, A. (2016) Hydrologic testing during drilling: application of the flowing fluid electrical conductivity (FFEC) logging method to drilling of a deep borehole. *Hydrogeology Journal* 24, 1333–1341.
- Wan, J. M. and Wilson, J. L. (1994) Visualization of the Role of The Gas-Water Interface on the Fate and Transport of Colloids in Porous-Media. *Water Resources Research*, 30, (1), 11-23.
- Wenning, Q.C., Almqvist, B.S.G., Hedin, P., and Zappone, A. (2016) Seismic anisotropy in mid to lower orogenic crust: Insights from laboratory measurements of V_p and V_s in drill core from central Scandanaivan Caledonides. *Tectonophysics* 692, 14–28.
- Wenning, Q.C., Berthet, T., Ask, M., Zappone, A., Rosberg, J.-E., and Almqvist, B.S.G. (2017) Image log analysis of in situ stress orientation, breakout growth, and natural geologic structures to 2.5 km

- depth in central Scandinavian Caledonides: Results from the COSC-1 borehole. *Journal of Geophysical Research Solid Earth* 122, 3999–4019.
- Witherspoon, P.A., and Gale, J.E. (1982) Hydrogeological testing to characterize a fractured granite. *Bulletin of the International Association of Engineering Geology* 26, 515–526.
- Witherspoon, P.A., Cook, N.G.W., and Gale, J.E. (1981) Geologic storage of radioactive waste: Field studies in Sweden. *Science* 211 (4485), 894–500.
- Xu, T. F., Senger, R. and Finsterle, S. (2008) Corrosion-induced gas generation in a nuclear waste repository: Reactive geochemistry and multiphase flow effects. *Applied Geochemistry*, 23, (12), 3423-3433.
- Yip, M., Mohle, J., and Bolander, J. (2005) Automated modeling of three-dimensional structural components using irregular lattices, *Computer-Aided Civil and Infrastructure Engineering*, 20, 393–407.
- Young, R.A., (ed.) (1993) *The Rietveld Method*. Oxford University Press, Oxford, England, 298 p.